1-1-2007

Biodiesel droplet combustion.

S.C. Anthony Lam

University of Windsor

BIODIESEL DROPLET COMBUSTION

by

S.C. Anthony Lam

A Thesis
Submitted to the Faculty of Graduate Studies
through Mechanical, Automotive and Materials Engineering
in Partial Fulfillment of the Requirements for
the Degree of Master of Applied Science at the
University of Windsor

Windsor, Ontario, Canada

2007

© 2007 S.C. Anthony Lam

Canada

Abstract

A study was undertaken to provide fundamental information regarding biodiesel as a transportation fuel. This was accomplished through droplet combustion analysis and examining flame transmisivity characteristics.

Four experimental setups were designed and assembled to allow for the evaluation of three fuels and their blends. Synthetic diesel was also tested, but not blended with other fuels.

Fryer grease biodiesel, ultra low sulfur diesel, and ethanol, as well as their blends were selected to undergo the following experimental procedures:

- Temporal varying droplet dimension measurements (diameter and flame diameter)

- Temporal varying droplet liquid temperature measurements

- Spatial varying droplet flame temperature measurements along the flame axis

- Spatial varying soot transmisivity measurements along the flame axis

The droplet lifetimes and their burning rate constants matched published results. Temperature measurements were within the range of reviewed literature, and soot measurements provided intriguing new information.

Acknowledgements

Many people have made completing this work possible. I would like to thank Dr. A. Sobiesiak and Dr. J. Tjong for their daily guidance and unwavering support. Many thanks are also extended to Dr. G. Rankin and Dr. P. Henshaw for acting as committee members and for the many valuable discussions.

The staff and my colleagues at the University of Windsor and the personnel at Ford Motor Company are also gratefully acknowledged.

Table of Contents

List of Tables

List of Figures

x

Nomenclature

amu	Atomic mass unit
$B5$	5 % biodiesel with 95 % diesel
$B20$	20 % biodiesel with 80 % diesel
CCD	Charged coupled device
r	Coordinate variable
CA	Crank angle
B_Y	Dimensionless transfer number
k	Droplet burning rate constant
D	Droplet diameter
D^2	Droplet diameter squared
D_f	Droplet flame diameter
t_d	Droplet lifetime
m_d	Droplet mass
r_s	Droplet radius
V	Droplet volume
fps	Frames per second
L	Litre
$\dot{m}''$	Mass conservation
$\dot{m}_A''$	Mass conservation of liquid A
$\dot{m}_A''$	Mass conservation of liquid B
D	Mass diffusivity
$\dot{m}$	Mass evaporation rate
P_i	Random uncertainty
$P_{\bar{x}}$	Random uncertainty of the sample mean
RMS	Root mean square
RPM	Revolutions per minute
$\bar{x}$	Sample mean
s	Sample standard deviation
s^2	Sample variance
ρ	Specific density
$ULSD$	Ultra low sulfur diesel
Y_A	Vapor mass fraction
$Y_{A,s}$	Vapor mass fraction at the droplet surface
$Y_{A,\infty}$	Vapor mass fraction far from the droplet surface

Chapter 1

Introduction

The continual and unpredictable increase in petroleum prices and experiences with supply and demand has renewed the population's interest in finding alternative sources of energy. Biodiesel is an integral part of the solution in alleviating the world's dependence on fossil fuels due to the rapid and continuing depletion of non-renewable petroleum resources. Biodiesel is an alternative fuel produced from renewable resources with the potential to substantially reduce emissions associated with petroleum diesel usage. With properties exceeding conventional diesel fuel, biodiesel can be seen as a viable substitute. Impending regulatory changes will mandate low sulfur diesel fuel. Higher production costs will result as these changes will require additional treatment in order for diesel fuel to regain its former lubricity. Biodiesel has high lubricity and can be used in existing diesel engines with minor modifications depending on the blend of biodiesel used. Therefore, biodiesel offers an immediate and seamless way to fuel existing diesel vehicles. Biodiesel can also be used for fueling aircraft and has a potential for disaster remediation as stated by Wardle [56].

1

Chapter 2

Objective

In mobility engineering applications, a clear understanding of the atomization and subsequent combustion of liquid fuels is critical for the development of propulsion devices.

The overall objective of this research is to provide insight into the viability of biodiesel as a transportation fuel. This will be accomplished by examining the combustion characteristics of biodiesel droplets.

There are two areas of interest in spray combustion. First, is the combustion of a single droplet. The second addresses the issue of droplet interaction within the spray that features randomly spaced droplets of various sizes. This thesis will fully explore the combustion of single droplets of biodiesel. A literature investigation has concluded that very little work has been done to experimentally characterize how biodiesel fuels burn in terms of the:

- Droplet burning rate constant (from the D^2 relationship)

- Droplet liquid temperature

- Droplet flame temperature

- Droplet sooting characteristics

2

First, an apparatus for studying single droplet combustion was designed and assembled. A single droplet of biodiesel fuel was placed on quartz filaments. An optical system allows for the visualization of the burning droplet and for capturing of image sequences. From the individual frames of the sequences, the droplet diameter was measured. The droplet lifetimes and their burning rate constants were determined from temporal variations of the square of the diameter.

A second experimental setup was assembled to determine the droplet liquid temperature during combustion.

A third setup was used to determine the droplet flame temperature during combustion.

Finally, the fourth setup provided insight into the sooting characteristics of droplets.

Chapter 3

Literature Review

3.1 Droplet Combustion

Spray combustion has many practical and relevant aspects in modern society especially in propulsion and energy-generating devices that are used everyday. These include, but are not limited to the internal combustion engine (diesel, gasoline, and other variants), rockets, gas turbines, boilers, furnaces, and process heaters. It is important to note that in these devices, droplet combustion is vital in order to fully understand the complexity of the flame kinetics. Droplet combustion is also of importance from a national security point-of-view. The United States Navy, Office of Naval Research stated that, "a systematic droplet combustion study is required in order to characterize fuel combustion and to design methodologies to improve their combustion", and with respect to soot, "excessive soot formation resulted in problems associated with signature detection particularly for weapons applications". In addition, the National Aeronautics and Space Administration (NASA) and the European Space Agency (ESA) have also funded work in the area of droplet combustion.

Experimental studies of droplet combustion have utilized the following three methods:

1. Droplet suspension: a single droplet is suspended at the end of a thin quartz filament

2. Falling droplet: a freely falling single droplet or droplet stream

3. Porous sphere: a porous sphere with liquid fuel fed to its interior at such a rate that the surface is just wetted enough to support combustion

4

The strengths and weaknesses of the three methods will be briefly discussed.

Suspending a droplet can be setup and performed with relative ease. Ignition is accomplished by a single pulse discharge or a continuous pulse discharge. Since the droplet is stationary, accurate microphotography can be taken of the droplets burning sequence. Because of the thickness of the suspension filament, it is difficult to suspend a droplet smaller than 1 mm which is larger than typical droplet sizes (of 10 μm to 1000 μm) within a spray. Nevertheless, this should not be of serious concern if the droplet size dependence is known. Suspending a droplet is limited to nonvolatile fuels. This is due to the fact that vaporization would have occurred during the period while suspending the droplet, priming the test area, and igniting the droplet [51].

Falling droplets offer the advantages of smaller drop sizes and the capability of using volatile fuels. To generate a droplet stream with uniform size and controlled spacing involves squeezing out droplets from a nozzled tube pressed against a piezoelectric transducer. By applying electric pulses, the transducer is deformed causing a pressure wave that forces a droplet out of the nozzle [51].

The porous sphere method conforms well with the steady-state gas-phase assumption associated with the D^2 law and allows precise probing of the flame structure [51].

3.2   Biodiesel

Biodiesel is a complex mixture of various compounds known as mono-alkyl esters. Biodiesel is produced from fatty feedstocks such as canola oil, recycled cooking oils (fryer grease), rapeseed oil, soybean oil, corn oil, sunflower oil, and animal fat (tallow or lard). These feedstocks are non-toxic, bio-degradable, and are renewable. The fatty acid composition of biodiesel derived from various sources and produced from different areas around the world can be seen in Table 3.1.

5

Table 3.2 tabulates the chemical structure of the fatty acids found in biodiesel. From Table 3.1 and Table 3.2, it can be clearly seen that biodiesel is a highly multi-component fuel composed of many constituents. The chemical composition of fat and oil esters is dependent upon the length and degree of unsaturation of the fatty acid alkyl chains.

Table 3.1 - Typical analyses of soybean and canola-based biodiesel (wt%) [60]

Fatty Acid	Central Brazil Soybean Oil	NE Brazil Soybean Oil	US Midwest Soybean Oil	Typical Ranges for US Soybean Oil	Typical Canada #1 Canola Oil
Palmitic	10.7	9.3	10.14	10.6 - 11.2	3.9
Stearic	3.4	3.1	4.20	4.4 - 5.6	2.0
Oleic	21.3	33.8	24.31	25.4 - 28.9	61.5
Linoleic	56.4	48.3	51.47	48.3 - 52.0	19.1
Linolenic	8.2	5.5	8.31	5.1 - 6.1	9.9
Margaric	n/a	n/a	0.11	n/a	n/a
Arachidic	n/a	n/a	0.35	n/a	0.7
Gadoleic	n/a	n/a	0.19	n/a	1.4
Behenic	n/a	n/a	0.37	n/a	0.4
Lignoceric	n/a	n/a	0.12	n/a	0.2
Other	n/a	n/a	0.17	n/a	0.9

Table 3.2 - Chemical structure of fatty acids found in biodiesel [60]

Acid Chain	# of Carbons	Structure
Caprylic	8	$CH_3(CH_2)_6COOH$
Capric	10	$CH_3(CH_2)_8COOH$
Lauric	12	$CH_3(CH_2)_{10}COOH$
Myristic	14	$CH_3(CH_2)_{12}COOH$
Palmitic	16	$CH_3(CH_2)_{14}COOH$
Palmitoleic	16	$CH_3(CH_2)_5CH=CH(CH_2)_7COOH$
Stearic	18	$CH_3(CH_2)_{16}COOH$
Oleic	18	$CH_3(CH_2)_7CH=CH(CH_2)_7COOH$
Linoleic	18	$CH_3(CH_2)_4CH=CH(CH_2)CH=CH(CH_2)_7COOH$
Linolenic	18	$CH_3(CH_2)CH=CH(CH_2)CH=CH(CH_2)CH=CH(CH_2)_7COOH$
Arachidic	20	$CH_2(CH_2)_{18}COOH$
Eicosenoic	20	$CH_3(CH_2)_7CH=CH(CH_2)_9COOH$
Erucic	22	$CH_3(CH2)_7CH=CH(CH_2)_{11}COOH$

There are four methods to produce biodiesel: transesterification, blending, microemulsion, and pyrolysis (thermal cracking). Transesterification is the most commonly used method in producing biodiesel and will be briefly introduced. It is the reaction of a lipid with an

6

alcohol to form esters and glycerol. Typically, a basic catalyst such as sodium hydroxide is used to convert the glycerol based tri-esters which are composed of fats and oils to methanol based mono-esters yielding free glycerol as a byproduct. Glycerol is nearly insoluble in biodiesel and in the feedstock oil and therefore forms a separate liquid phase. The biodiesel may require distillation to remove traces of glycerides, and the glycerol may be purified by vacuum distillation. Ethanol or other alcohols may be used in the transesterification process. These are generally less cost effective to use, and are not as easily reacted with the fat or oil as is methanol [28].

Biodiesel can be produced from a variety of feedstocks. Canadian biodiesel is mainly derived from canola, while the United States uses soybean. In Europe, rapeseed is heavily used, and in Southeast Asia, palm oil is used. This reflects the agricultural practices of these regions.

Biodiesel has a higher cetane number (51 to 62) than petroleum diesel (48 to 50). This broad range of cetane numbers is a result of the differences in the fractional conversion of triglycerides to esters and by the presence of residual methanol and glycerol in the fuel [28]. The cetane number indicates how readily a fuel will auto-ignite. The higher the cetane number, the shorter the delay between the injection and the ignition which will result in improved cold start, less noise, and reduced white smoke.

Biodiesel is naturally high in lubricity. Agarwal et al. [2] mentioned that the use of biodiesel resulted in 30 % less wear of engine components when compared to using ultra low sulfur diesel. The problem associated with the lubricity of petroleum diesel is due to the desulfurization stage at the oil refinery plants. This desulfurization is a result of government regulations to reduce sulfur content. During this process, compounds containing polar heterocyclic nitrogen (which contribute to the lubricating property of the fuel) are also removed along with sulfur. This desulfurized fuel causes premature engine wear. Oil refineries add lubricity additives to restore lubricity. Biodiesel does not have this problem, and it can act as a lubricity additive for petroleum diesel.

7

Biodiesel is essentially free of sulfur. The sulfur is converted to sulfur oxide in the tailpipe and a fraction of the sulfur oxide is converted to sulfuric acid, which is classified as a particulate - a regulated pollutant. Sulfur oxides are also regarded as air pollutants. Generally, biodiesel produces less harmful emissions as it can be seen in Table 3.3.

Table 3.3 - Emissions from biodiesel usage

	%
Brake specific fuel consumption	+ 15
Nitrogen oxides	+ 10
Hydrocarbons	- (20 to 50)
Carbon monoxide	- (25 to 35)
Particulate matter	- (30 to 50)
Visible Smoke	- (60 to 80)
Polycyclic aromatic hydrocarbons	- (75 to 80)

There is a tendency for brake specific fuel consumption and nitrogen oxides to increase while hydrocarbons, carbon monoxide, particulate matter, visible smoke, and polycyclic aromatic hydrocarbons decrease. Brake specific fuel consumption is a measure of an engine's efficiency. It is the rate of fuel consumption divided by the rate of power production. The increase in nitrogen oxides is due to atmospheric nitrogen through reactions that occur in the cylinder at peak combustion temperatures.

The demand for biodiesel continues to grow throughout various major parts of the world such as the United States and Europe. Figure 3.1 delineates the demand for biodiesel in Canada. It is expected that this trend will continue in Canada and the rest of the world because of growing concerns over national security (dependence on foreign energy sources), economic, and greenhouse gas / climate change issues. From an economic standpoint, biofuels are meant to supplement or replace liquid petroleum fossil hydrocarbon fuels as future demand begins to surpass supply.

8
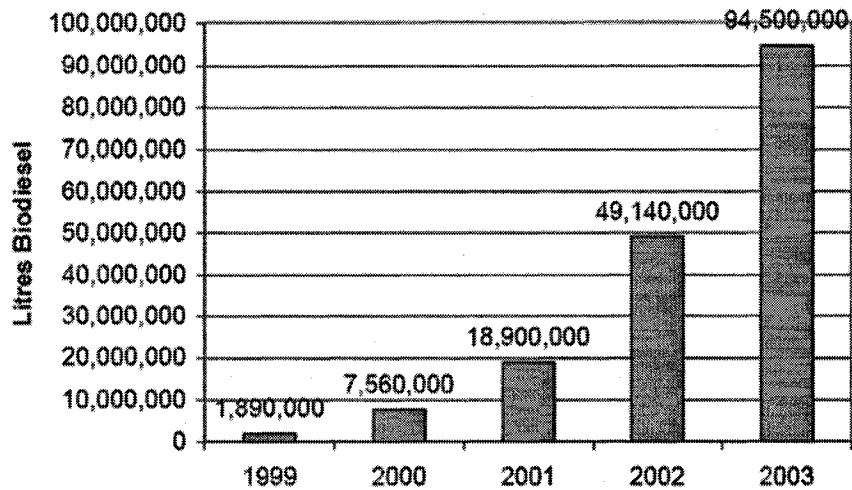
Figure 3.1 - Demand for biodiesel in Canada

The cost of biodiesel is currently higher than that of petroleum diesel. Table 3.4 shows the cost of biodiesel in various parts of the United States. As with any emerging fuel, cost will be high at first. With the assistance of government subsidies, costs will gradually stabilize and will become more economically attractive as the infrastructure develops and technology to produce the fuel matures.

Table 3.4 - The cost of biodiesel in various parts of the United States
[Alternative Fuels Index, May 2004]

City	US$/USG		
	B100 Price	Diesel Price	Biodiesel Premium
Providence	1.96	1.14	0.83
Oklahoma City	1.98	1.15	0.83
Dallas	2.00	1.18	0.82
Jackson	2.03	1.11	0.90
Boston	2.03	1.14	0.90
Louisville	2.05	1.13	0.92
Minneapolis	2.07	1.17	0.90
Madison	2.08	1.13	0.95
Portland	2.08	1.13	0.95
Birmingham	2.10	1.09	1.01
Houston	2.10	1.10	1.00
Kansas City	2.10	1.16	0.94
Little Rock	2.10	1.11	0.99

9

At present, fueling a diesel engine with biodiesel poses some technical challenges. This is mainly due to the high viscosity associated with biodiesel when compared to petroleum diesel fuel, which can be seen in Table 3.5. The viscosity is due to the triglycerides that are unfortunately associated with biofuels.

Table 3.5 - Biodiesel and diesel differences [3]

Type	Dynamic viscosity	Density	Kinematic viscosity	Surface tension
	mPa-s	kg/m^3	mm^2/s	mN/m
Peanut	3.69	861.1	4.29	28.70
Canola	3.61	853.6	4.23	28.79
Coconut	2.25	813.1	2.77	26.82
No. 2 Diesel	2.13	851.9	2.5	24.00

The high viscosity can cause the injection nozzles and piston ring grooves to coke, and makes operation difficult at low temperatures, in addition to decreasing the performance of the atomization of the injected fuel. Other problems are insufficient stability, low resistance to cold, and poor elastomer compatibility.

Biodiesel has a limited shelf life of six months. This is due to the oxidative degradation from anaerobic bacteria which is termed oxidative stability. Biofuels can demonstrate instability in several ways. They can be hydrolyzed by water, or oxidized, especially in the presence of both water and oxygen, and they can be attacked by both aerobic and anaerobic bacteria and molds (fungi). These microbes, which are activated by the small amounts of water that are typically present in fuels and their storage facilities, consume minute amounts of fuel and create biomass that can block fuel lines. Water present in the fuel can cause the formation of rust, and in the presence of acids and hydroperoxides formed by fuel oxidation, lead to corrosion. The main source of instability in biodiesel fuels is the unsaturation of the fatty acid chains which are susceptible to biological attack. Although other liquid fuels do not exhibit such a biological behavior, water is almost always present and may be unavoidable in real-world use.

10

Research is currently being undertaken by automotive and engine manufacturers, as well as academic institutions and research organizations in order to understand the effects of fueling an engine with biodiesel. Just to mention briefly: Scholl et al. [40] had problems with the fuel pump and injector system. Ma et al. [28] noticed severe injector coking led to decreases in power output and thermal efficiency. Wardle [56] had blocked fuel filters. Agarwal et al. [1] observed a decrease in thermal efficiency. During extensive field trials conducted by diesel fuel injection equipment manufacturers in collaboration with customers, the following injection equipment and engine problems were identified:

- Corrosion of components

- Low pressure fuel system blockage

- Increased dilution and polymerization of engine sump oil

- Pump seizures

- Increased injection pressure

- Elastomeric seal failures

- Fuel injector spray hole blockage

The likelihood of these problems occurring is greater for engines that are not used regularly such as seasonal vehicles (snow removal vehicles, etc.)

Chapter 4

Theory of Droplet Combustion

4.1 D^2 Law

In droplet combustion, the D^2 law is used to describe burning of fuel droplets. The coordinate system is defined in the following figure.

Flame position

r $Y_A = 1$ $Y_{B,\infty} = 1$

r_s

r
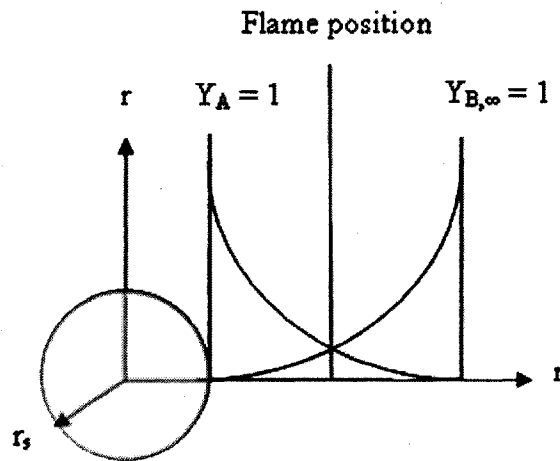
Figure 4.1 - Evaporation of a liquid droplet

The coordinate variable is r, and its origin is at the center of the droplet. The droplet radius is defined as r_s. The heat from the ambient environment supplies the necessary energy to vaporize the liquid. Then the vapor diffuses from the droplet surface into the ambient gas. The droplet radius will decrease with time until the droplet is completely evaporated ($r_s = 0$) due to mass loss. Solving the mass flow rate of the vapor from the surface at any instant in time will allow for the calculation of the droplet radius as a function of time.

12

In order to reduce the number of unknowns and hence equations, the following four assumptions are made:

The first assumption is that the evaporation process is quasi-steady where at any instant in time, the process can be described as if it were steady state. Therefore, the need for differential equations is eliminated.

The second assumption is that droplet temperature is uniform, and that the temperature is to be some fixed value below the liquid boiling point. The transient heating of the liquid does not affect the droplet lifetime. Determining the temperature at the droplet surface depends on the heat transfer rate to the droplet. Therefore, assuming a specified temperature eliminates the need to apply conservation of energy to the gas phase surrounding the liquid droplet and the droplet itself.

The third assumption is that the mass fraction of vapor at the droplet surface is determined by liquid-vapor equilibrium at the droplet temperature.

The final assumption is that all thermo-physical properties, specifically density ρ and mass diffusivity D are constant, thereby allowing a simplified closed-form solution even though properties may vary through the gas phase from the droplet surface to the surroundings.

The mass evaporation rate $\dot{m}$ and the droplet radius history $r_s(t)$ can be found by writing a droplet vapor species conservation equation and a droplet liquid mass conservation equation. Species conservation will determine the evaporation rate thereby yielding the droplet size as a function of time. Overall mass conservation can be expressed as

$$\dot{m}(r) = \text{constant} = 4\pi r^2 \dot{m}'' \qquad (4.1.1)$$

where $\dot{m}'' = \dot{m}_A'' + \dot{m}_B'' = \dot{m}_A''$ since $\dot{m}_B'' = 0$. Note, $\dot{m}_A''$ and $\dot{m}_B''$ represent the overall conservation of mass of gas A and gas B respectively. Mass flow rate is constant and mass flux is not. Species conservation for the droplet vapor becomes

13

$$\dot{m}_A{}'' = Y_A \dot{m}_A{}'' - \rho D_{AB} \frac{dY_A}{dr} \qquad (4.1.2)$$

Recall $\dot{m} = \dot{m}_A$. Solving $\dot{m}$ by substituting Equation (4.1.1) into Equation (4.1.2) yields

$$\dot{m} = -4\pi r^2 \frac{\rho D_{AB}}{1-Y_A} \frac{dY_A}{dr} \qquad (4.1.3)$$

Applying the boundary condition (at the droplet surface, the vapor mass fraction is $Y_{A,s}$), $Y_A(r = r_s) = Y_{A,s}$ yields

$$Y_A(r) = 1 - \frac{(1-Y_{A,s})\exp\left[-\dot{m}/(4\pi\rho D_{AB}r)\right]}{\exp\left[-\dot{m}/4\pi\rho D_{AB}r_s\right]} \qquad (4.1.4)$$

The evaporation rate is determined by letting $Y_A = Y_{A,\infty}$ for $r \rightarrow \infty$ and solving for $\dot{m}$

$$\dot{m} = 4\pi r_s \rho D_{AB} \ln\left[\frac{(1-Y_{A,\infty})}{(1-Y_{A,s})}\right] \qquad (4.1.5)$$

Taking the logarithm of Equation (4.1.5) is used to define the dimensionless transfer number B_Y. Doing so, will show how the vapor mass fractions at the droplet surface and far from the surface affect the evaporation rate.

$$1 + B_Y = \frac{1 - Y_{A,\infty}}{1 - Y_{A,s}} \qquad (4.1.6)$$

Using the transfer number, the evaporation rate is expressed as

$$\dot{m} = 4\pi r_s \rho D_{AB} \ln(1 + B_Y) \qquad (4.1.7)$$

From Equation (4.1.7), when the transfer number is 0, the evaporation rate is 0. Likewise, as the transfer number increases, the evaporation rate increases. From a physical sense standpoint, the mass fraction difference ($Y_{A,s} - Y_{A,\infty}$) can be interpreted as a driving potential for mass transfer.

14

The droplet mass conservation is used to obtain the droplet diameter profile by writing a mass balance that states that the rate at which the mass of the droplet decreases is equal to the rate at which the liquid is vaporized.

$$\frac{dm_d}{dt} = -\dot{m} \tag{4.1.8}$$

where the droplet mass m_d is determined by

$$m_d = \rho_l V = \frac{\rho_l \pi D^3}{6} \tag{4.1.9}$$

where V is the droplet volume and D (= 2 r_s) is the droplet diameter. Substituting Equation (4.1.9) and Equation (4.1.7) into Equation (4.1.8) yields

$$\frac{dD}{dt} = -\frac{4\rho D_{AB}}{\rho_l D} \ln(1 + B_Y) \tag{4.1.10}$$

Equation (4.1.10) is normally expressed as

$$\frac{dD^2}{dt} = -\frac{8\rho D_{AB}}{\rho_l} \ln(1 + B_Y) \tag{4.1.11}$$

Taking the time derivative of Equation (4.1.10) indicates that the droplet diameter is constant. Therefore, D^2 varies linearly with time with a slope of $-(8\rho D_{AB}/\rho_l)ln(1+B_Y)$. This slope is known as the burning constant k.

$$k = \frac{8\rho D_{AB}}{\rho_l} \ln(1 + B_Y) \tag{4.1.12}$$

To determine the time it takes a droplet of given initial size to evaporate completely (known as the droplet lifetime t_d), Equation (4.1.11) or Equation (4.1.10) can be used. Therefore,

$$\int_{D_0^2}^{0} dD^2 = -\int_{0}^{t_d} k dt \tag{4.1.13}$$

which yields

15

$$t_d = \frac{D_0^2}{k}$$ (4.1.14)

Changing the upper limits of Equation (4.1.13) provides a general relationship expressing the variation of diameter with time.

$$D^2(t) = D_0^2 - kt$$ (4.1.15)

Equation (4.1.15) is known as the D^2 law for droplet evaporation. This law can be used to describe the pyrolysis of fuel droplets

4.2   Soot Formation

Warnatz [57] designated soot as a specific class of particulate matter. It is technically defined as the black solid product of incomplete combustion or pyrolysis of fossil fuels and other organic materials.

Soot is formed in the narrow region on the fuel-rich side of a diffusion flame. Most of the soot is burned with the fuel at the diffusion flame. The fraction of soot that is not oxidized becomes exhaust emission.

In its pure form, soot is physiologically inert. Since soot is a good absorbent, it plays important roles as an industrial filler and pigment (such as carbon black). However, soot is also an air pollutant (namely diesel soot) containing toxic and carcinogenic aggregates such as polycyclic organic matter.

Soot is primarily composed of carbon (> 80%) and consists of agglomerated particles with diameters on the order of 10 nm to 30 nm comprising of crystalline and amorphous structures.

16

Soot particles encountered in diesel engine combustion have a size distribution over a range from a few nanometers to 70 nm. The shape of the individual particle is roughly spherical though they may form non-spherical agglomerates in the exhaust.

The generalized chemical formula of soot is C_8H. Soot is organized in straight or branched chains of spherical or near-spherical particles adhering to one another, each with a diameter of 10 nm to 30 nm and containing approximately 10^6 carbon atoms.

Flame temperatures within the range of 1000 °C to 2500 °C will emit soot.

The physical structure of a soot molecule can be found in the form of a platelet, crystallite, or particle.

Soot formation consists of multiple complex reaction mechanisms. Soot formation first begins with the pyrolysis or oxidative pyrolysis of a hydrocarbon fuel. Subsequently, polymerization of the particle-like structures arises followed by either surface growth or coagulation of the molecules. This particle inception takes place between 500 amu and 2000 amu. Afterwards, aggregation of the molecules occur leading to oxidation of the hydrocarbon fuel to form soot. Soot formed depends strongly on the initial fuel structure.

Understanding soot generation in hydrocarbon fuels is fundamental in establishing practical strategies for increasing combustion efficiency, and at the same time, limiting particulate matter emissions.

Diesel engines offer substantial fuel economy advantages for road transportation. However, more stringent standards are being introduced for diesel engines. In order to meet these impending regulations, a clear understanding of the combustion process and emission formation in a diesel engine is critical for engine researchers / designers. The developments of various techniques for analyzing the combustion and pollutant formation in diesel engines are the result of intense interest in reducing exhaust emissions. Soot

17

formation and oxidation in a diesel engine are complicated and difficult to examine. The study of soot involves the use of physical probing and optical techniques.

Physical probing is usually performed by a fast sampling valve capable of providing information on the chemical composition of soot as well as soot concentration measurements. In-cylinder sampling is another physical technique.

18

Chapter 5

Methodology and Procedures

Three fuels and their blends, as well as synthetic diesel were selected based on availability to undergo droplet combustion evaluations. The following chapter explains in detail the four tests the fuels and their blends underwent. Each measurement was conducted 10 times and based on those measurements, the sample mean was calculated and used. Table 4.1 illustrates the percentage blends of fuels that were tested. The synthetic diesel was derived from recycled tires and the fryer grease was originally canola oil.

Table 4.1 - Blends of fuel tested (%)

ULSD	Fryer Grease Biodiesel	Ethanol
	100	
80	20	
50	50	
95	5	
100		
	20	80
	50	50
	5	95
		100
50		50

Droplets of various volumes were initially tested to determine the best volume for fuel delivery and ease of ignition. A volume of 5 mm^3 was initially tried. The droplet was too large and fell off the filament and thermocouple. Next, 4 mm^3 and 3 mm^3 of fuel were attempted. For both of those volumes, the droplet rested on the filament, but not on the thermocouple. Upon ignition, the burning droplet fell off the filament. Subsequently,

19

2 mm^3 of fuel was tested and was found to rest quiescently on the filament and thermocouple. For consistency, 2 mm^3 of fuel was used for all experiments.

Pre-heating the fuel droplet was investigated to determine if transient heating would have any effects on the diameter and flame diameter. It was determined that elevating the droplet's temperature does not affect the droplet burning rate constant. Turns [51] also came to the same conclusion.

Both horizontal and vertical arrangements of the quartz filaments were initially tested. It was decided to use the vertical arrangement for diameter and flame diameter measurements due to background lighting effects associated with the horizontal filaments.

The time constant or response time is the time required by a sensor to reach 63.2 % of a step change in temperature under a specified set of conditions. Five time constants are required for the sensor to approach 100 % of the step change value. An exposed-junction thermocouple is the fastest responding and was chosen to be used for liquid and flame temperature measurements. Table 5.2 lists the response time (from the Omega Temperature Handbook [62]) of the thermocouples with various wire diameters. The junction diameter is 2.5 times the wire diameter.

Table 5.2 - Thermocouple response times

Type	Wire Diameter		Response Time
	mm	in	(s)
K	0.13	0.005	0.04
	0.25	0.010	0.22
	0.38	0.015	0.40
S	0.025	0.001	0.002
	0.075	0.003	0.021
	0.130	0.005	0.040

Thermocouple wire diameters of various sizes were initially tested to allow for the fastest response time. A diameter of *0.003 in* was initially tried. The droplet was too large and fell off the thermocouple. Next, a *0.005 in* diameter was attempted. The droplet rested on the thermocouple junction, but fell off when the pilot flame was brought into the

20

vicinity of the droplet. Finally, a *0.010 in* diameter was tested and was found that the droplet rested quiescently and ignited in the presence of the pilot flame.

5.1 Diameter Measurements

Droplets of each fuel were suspended at the spherical end of a 1 mm diameter quartz filament in a vertical position. A 5 μL Hamilton high precision micro-syringe fitted with a specialized Chaney adapter was used to deliver the fuel in order to maintain a constant volume of 2 mm^3. The Chaney adapter secures the plunger location to allow repeatable volume deliveries. Figure 5.1 shows the vertical and horizontal quartz filament orientations.

Vertical

Horizontal
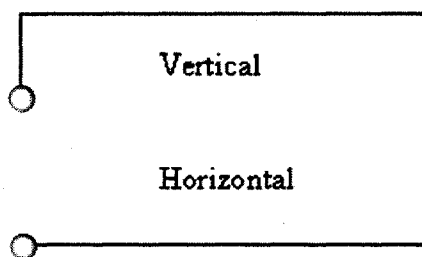
Figure 5.1 - Quartz filament orientations

Figure 5.2 illustrates the apparatus used in determining droplet diameter. A macro lens with a magnification ratio of 1:1 was coupled with a CCD camera at a resolution of 512 × 240 pixels capturing at 125 fps was used to acquire the images as the droplets were burning. The time history of the droplet diameter over its burning duration was used to calculate the burning rate constants.

Ignition of the droplet was made via an adjustable firing spark mechanism composed of fully adjustable needle-like tungsten electrodes.

21

Macro lens, 1:1 magnification ratio

1 mm diameter quartz filament
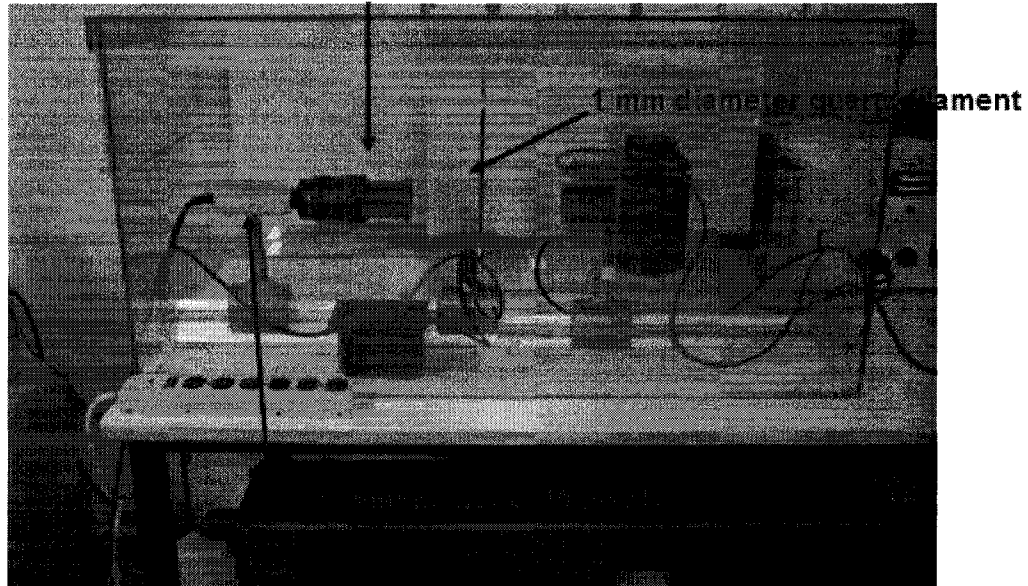
Figure 5.2 - Optical apparatus for droplet diameter testing

To determine the diameter of the droplets, sequential images of the droplets were recorded. Figure 5.3 illustrates a series of frames from a high-speed movie capturing the entire biodiesel burning sequence. Both the droplet and filament can be seen at time t = 0.0 s as the droplet rests on the filament. Droplet diameters were subsequently measured from a sequence of images, such as those shown in Figure 5.3. To determine the burning rate constant k, a line was fitted over the square of the diameter with respect to time.

| t = 0.0 s | t = 1.0 s | t = 1.6 s | t = 2.5 s |
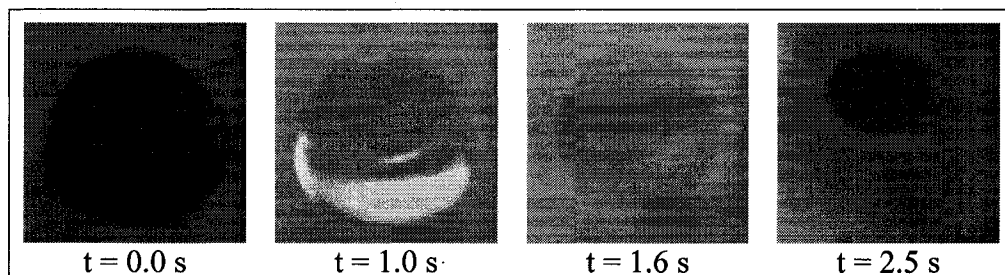
Figure 5.3 - Biodiesel droplet burning sequence

For each frame, a histogram representing the changes in grey-scale intensity during the burning sequence of a droplet was obtained as shown in Figure 5.4. A change in the grey-scale intensity of the image was defined as the edge of the droplet. On average, 100 frames were processed for each trial.

22

Initial   Burning
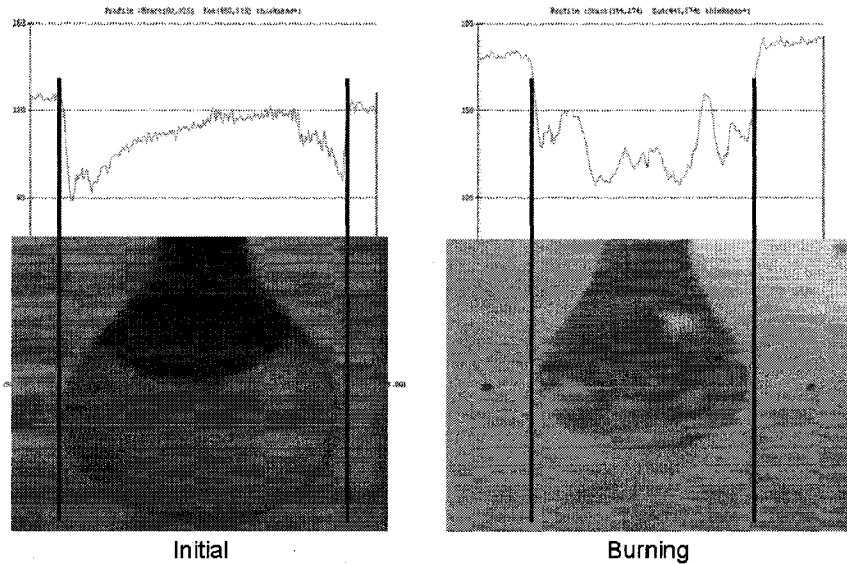
Figure 5.4 - Histogram representing the droplet burning sequence

5.2 Flame Diameter Measurements

Figure 5.5 defines the bounds where the diameter, D and flame diameter, D_f measurements were taken. The flame diameter measurements were obtained using the same procedure as droplet diameter measurements. The only difference was in the setup of the equipment. The camera position was adjusted in order to adequately capture the flame. The aperture of the camera lens was reduced to prevent over-saturation from the brightness of the flame.
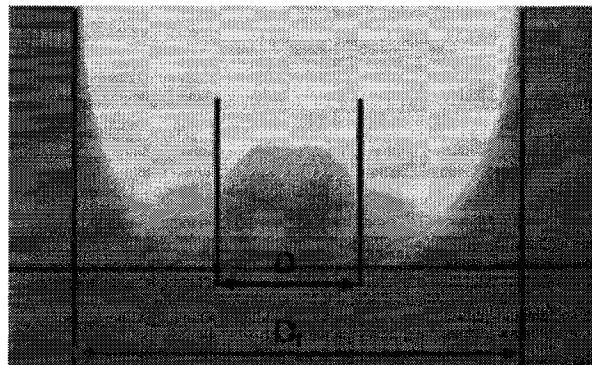
Figure 5.5 - Diameter and flame diameter dimensions

23

5.3   Liquid Temperature Measurements

Temperature histories of the liquid phase were obtained by placing a single droplet of fuel on an exposed-junction K-type thermocouple connected to the apparatus shown in Figure 5.6. Ignition was made by a pilot flame that was brought in when required for ignition and the droplet was placed on the thermocouple as shown in Figure 5.7. The temperature histories during the combustion phase were recorded and used to evaluate the boiling temperatures of the various fuels. A sampling rate of 1000 Hz was used to avoid aliasing of repetitive information and so that clean signals can be extracted from high noise environments.

The traversing mechanism in Figure 5.6 has two degrees of freedom allowing motion in the positive and negative *x*- and *y*-direction.
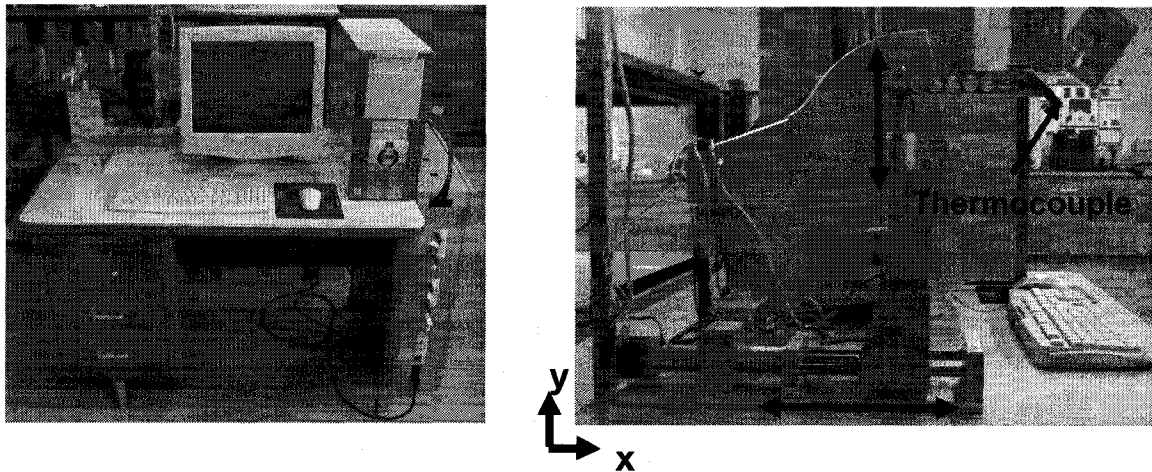
Figure 5.6 - Apparatus for temperature measurements

Figure 5.7 shows the droplet suspended on the thermocouple. The thermocouple was held stationary inside the droplet during the measurement of the droplet liquid temperature. The droplet was carefully placed by the micro-syringe. Due to gravitational effects, the droplet hung slightly downwards.

24
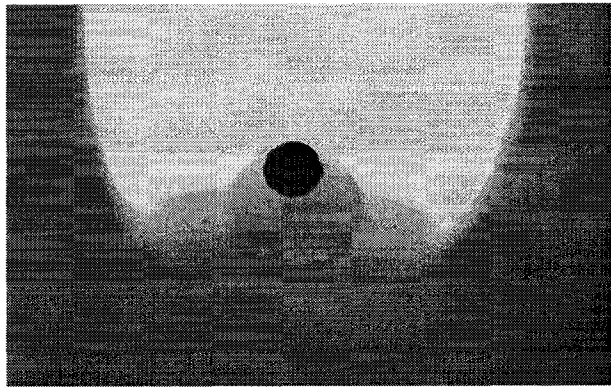
Figure 5.7 - K-type thermocouple positioning

A National Instruments LabVIEW program was written to acquire and preview the temperatures before post-processing in Microsoft Excel. Shielded thermocouple wires were used to prevent noise interference. Considering the sampling rate, a running average of the temperature history profiles with a 200 sample window resulted in smoother plots. This is clearly evident as it can be seen in Figure 5.8 and Figure 5.9. Figure 5.8 shows the temperature history profile before applying the running average and Figure 5.9 illustrates the result of the running average.
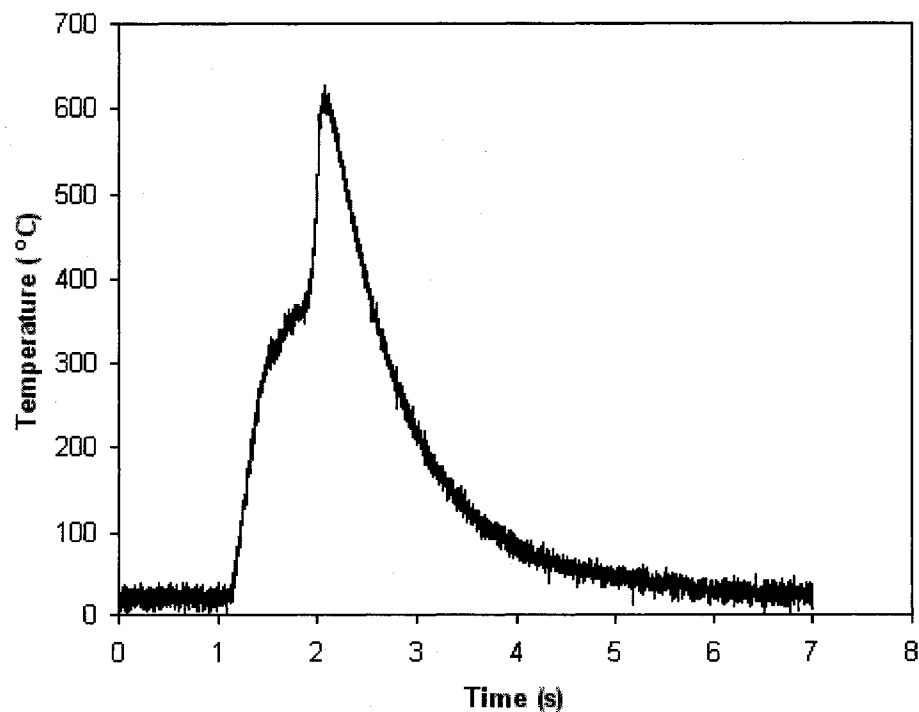
Figure 5.8 - Biodiesel temperature history without averaging

25
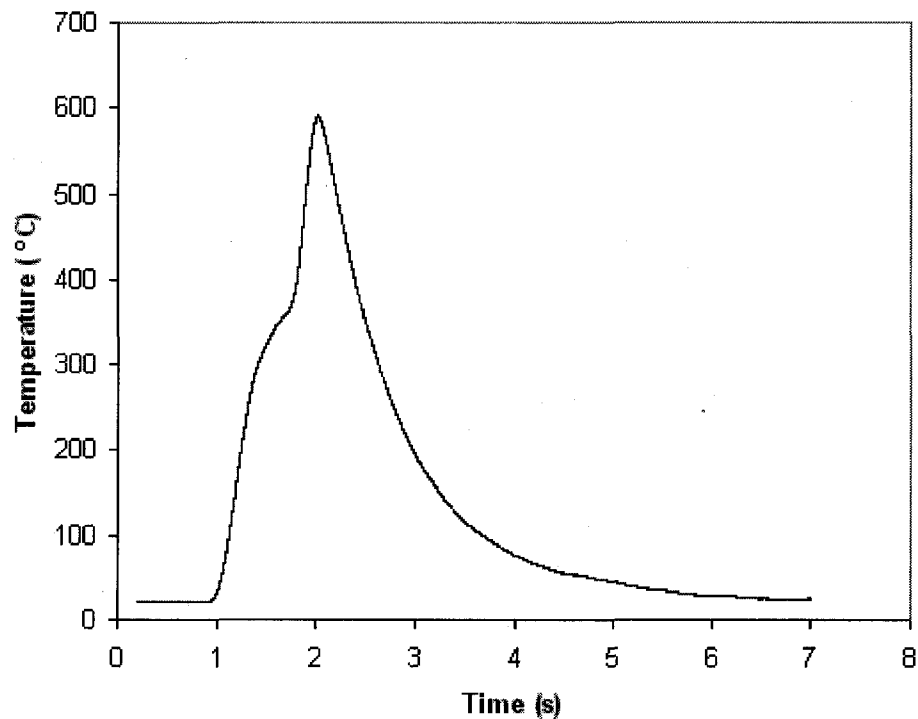
Figure 5.9 - Biodiesel temperature history with averaging

5.4 Flame Temperature Measurements

In order to accurately determine the flame temperature, an S-type thermocouple was chosen. Exposed-junction S-type thermocouples have the necessary range ($0°C$ to $1450°C$) that are typical of flames. For example, Strehlow [50] stated that a buoyant laminar hydrogen diffusion flame has a maximum flame temperature of $1227°C$.

Flame temperature measurements were taken every 2 mm along the flame's vertical axis above the droplet and at one location below the droplet with the apparatus shown in Figure 5.6. One should note that for each location, ten trials were conducted. Therefore, each point on the flame temperature profiles represents an average of the maximum temperature of 10 trials over the entire droplet burning lifetime. The maximum temperatures occurred at different times during the droplet burning lifetime. Ignition was made via a pilot flame.

26

Figure 5.10 shows the position of the thermocouple held stationary at the underside of the droplet. The thermocouple was incrementally moved upwards at the top to obtain spatially varying droplet flame temperatures.
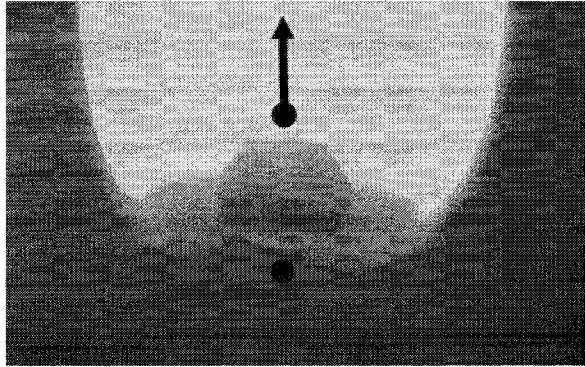
Figure 5.10 - S-type thermocouple positioning

The same data processing method was used as in the droplet liquid temperature measurements.

5.5 Flame Transmisivity Measurements

A Coherent Innova 70 water-cooled argon ion laser was used to determine the flame transmisivity under various experimental conditions such as varying temperatures, altering filament orientation, and changing droplet volume. Flame transmisivity measurements are representative of sooting characteristics and are a precursor to quantifying soot volume fraction measurements. Figure 5.11 illustrates the setup. The droplet was suspended at varying heights in order to determine soot emissivity over the entire flame length and ignition was made by a pilot flame that was brought in when required for ignition.

27
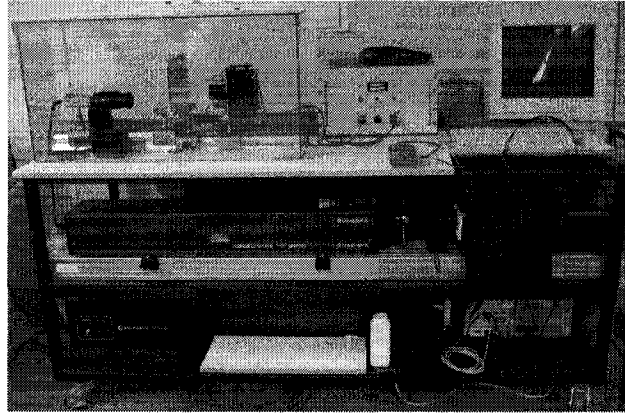
Figure 5.11 - Experimental setup for soot measurement
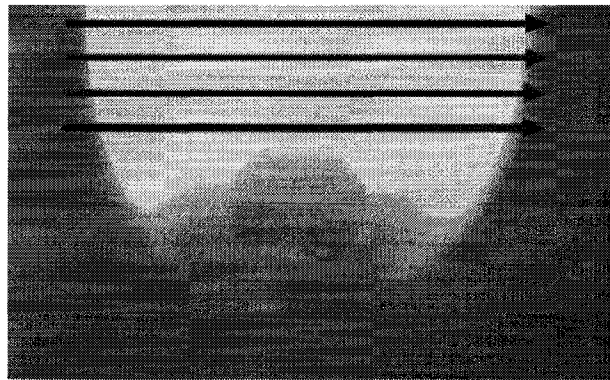
Figure 5.12 - Ar-ion laser beam crossing the flame at incremental heights
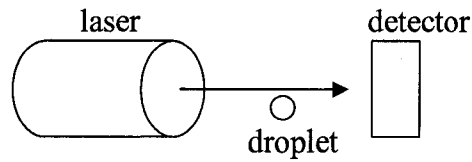
Figure 5.13 - Ar-ion laser setup

After the laser beam passed the flame, a laser power measurement was recorded and compared with the beam power with no droplet to determine laser power attenuation. The lowest value from the soot profiles (Figure 5.14 to Figure 5.20) were plotted since they represented the maximum soot absorption. The preceding figures are representative of the steps taken. An explanation is as follows to assist in interpreting the figures correctly:

28

In Figure 5.14, Figure 5.16, and Figure 5.18, a dip or a decline and an increase is evident. This dip occurs when the droplet ignites in the path of the laser beam. For example, in Figure 5.14, the laser beam had a stable signal attenuation. Once an interference (the burning droplet) is brought into the path of the laser, a dip arises. Heating the droplet causes a larger dip, meaning more soot blocked the signal being registered from the laser measurement detector. In other words, heating causes more soot which effectively blocks the laser beam. Once the droplet completes combustion, the laser signal rises back to its original set-point.

In Figure 5.15, Figure 5.17, and Figure 5.19, an elevation or an increase followed by a decrease is apparent. In this situation, no laser beam was used. The laser measurement dectector only recorded the luminosity of the droplet burning. The elevation occurs when the droplet ignites. At first, the detector reads zero, since there is no combustion. Once combustion is initiated, the detector registers the burning droplet, which is represented by the elevation. Once combustion ends, the detector returns to reading zero.

Figure 5.19 depicts the various stages that occurred when the soot profile of biodiesel was recorded. In the first stage, the pilot flame is brought in to allow the droplet to ignite. Then, the pilot flame is removed. Afterwards, the droplet ignites. Finally, the droplet completes combustion.

Figure 5.20 illustrates the testing and verification of the response time of the laser power measurement meter. This was done to ensure that the laser power measurement meter was logging the proper value. The response time was 1.6 s and the time it takes for the measurements to be taken was 2 s. The slight rise within the dip is an indication of the sudden fragmentation or micro-explosion of the biodiesel fuel droplet. This micro-explosion was due to the fact that biodiesel is a multi-component fuel where some fractions boil at lower temperatures causing break-up of the droplet.
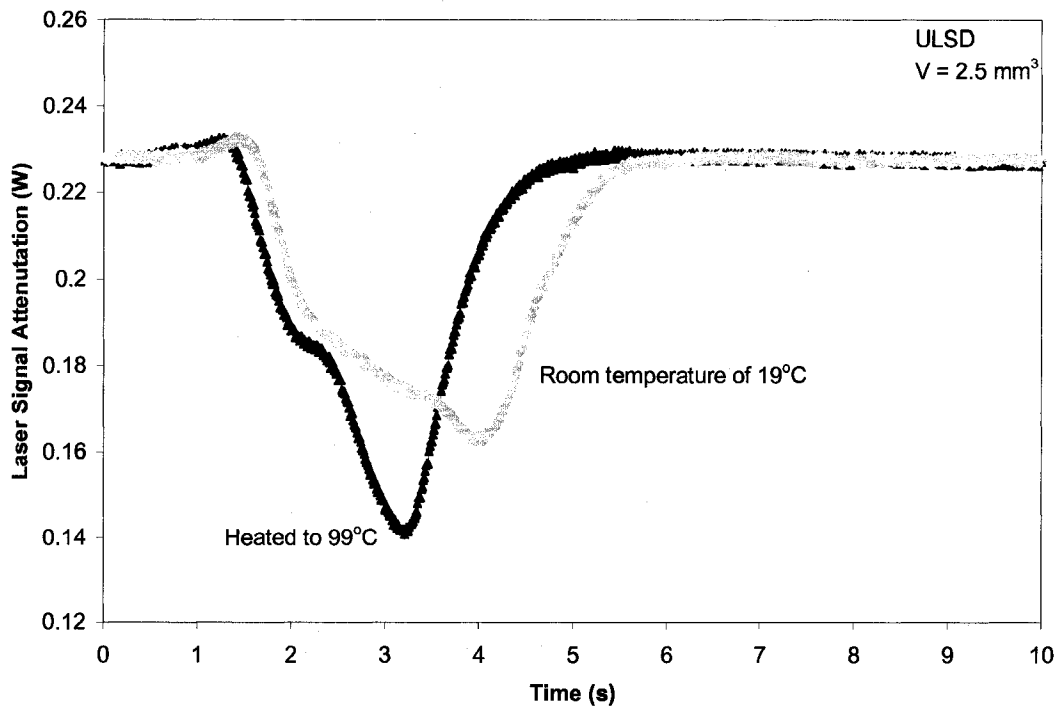
Figure 5.14 - Heated ULSD soot profile with laser
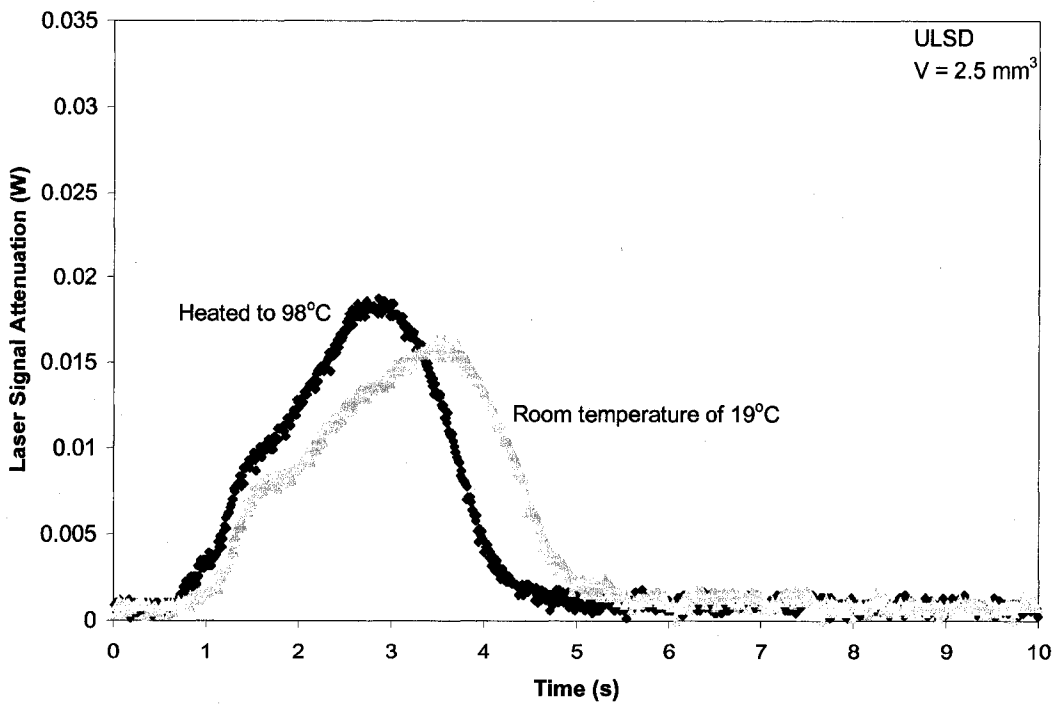
Figure 5.15 - Heated ULSD soot profile without laser (only droplet)

30
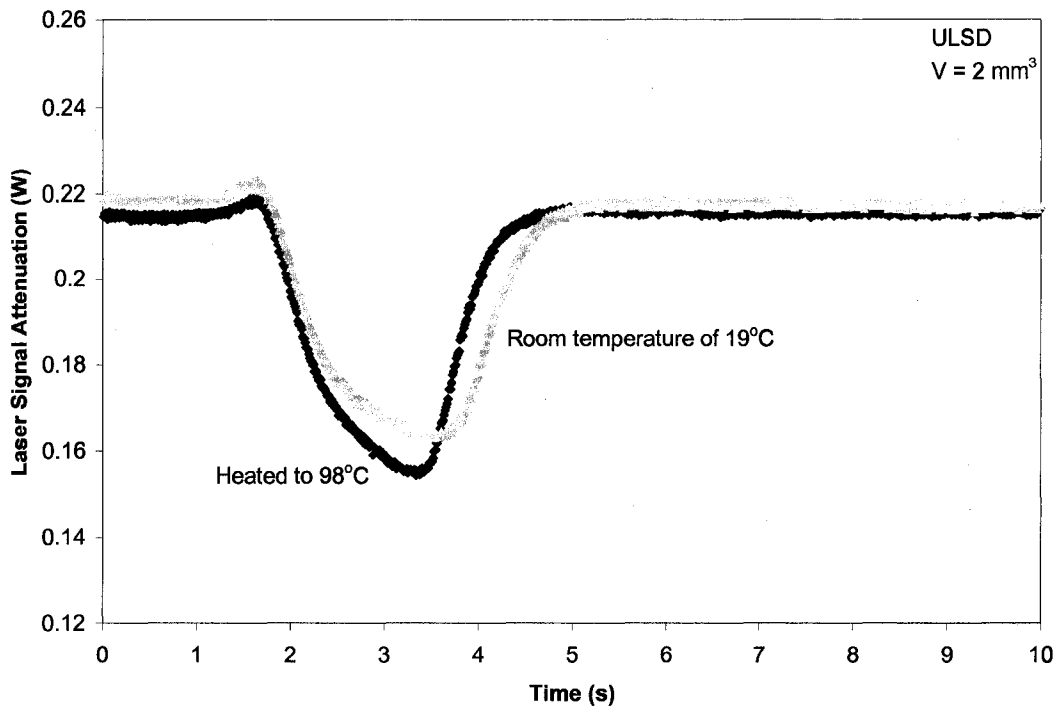
Figure 5.16 - Heated ULSD soot profile with laser
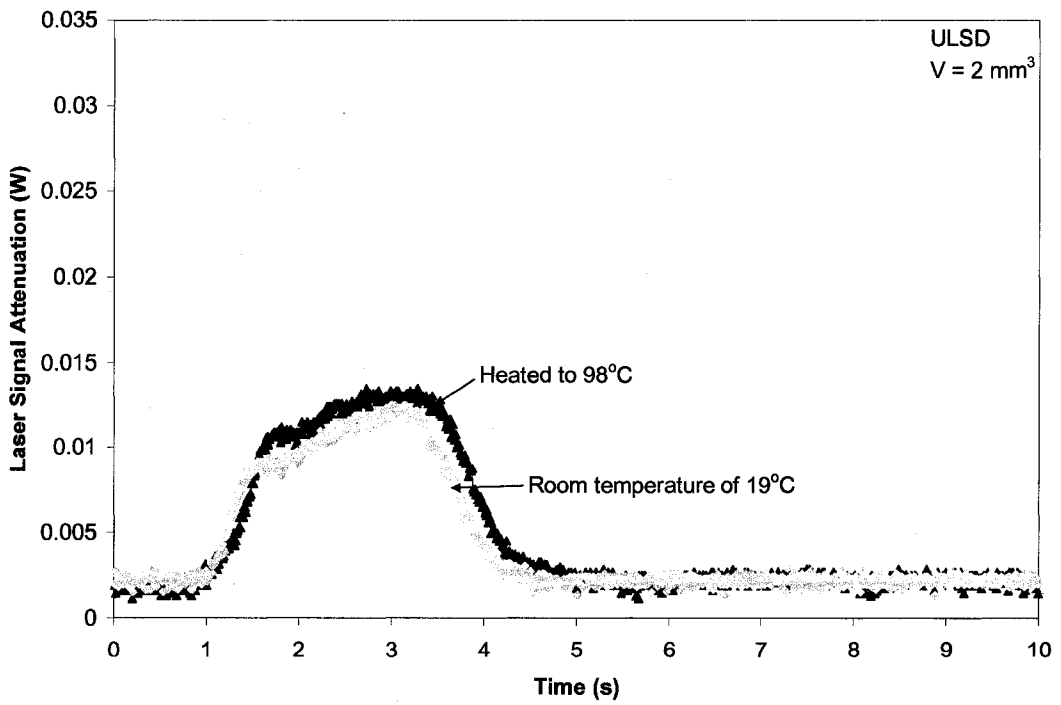
Figure 5.17 - Heated ULSD soot profile without laser (only droplet)

31
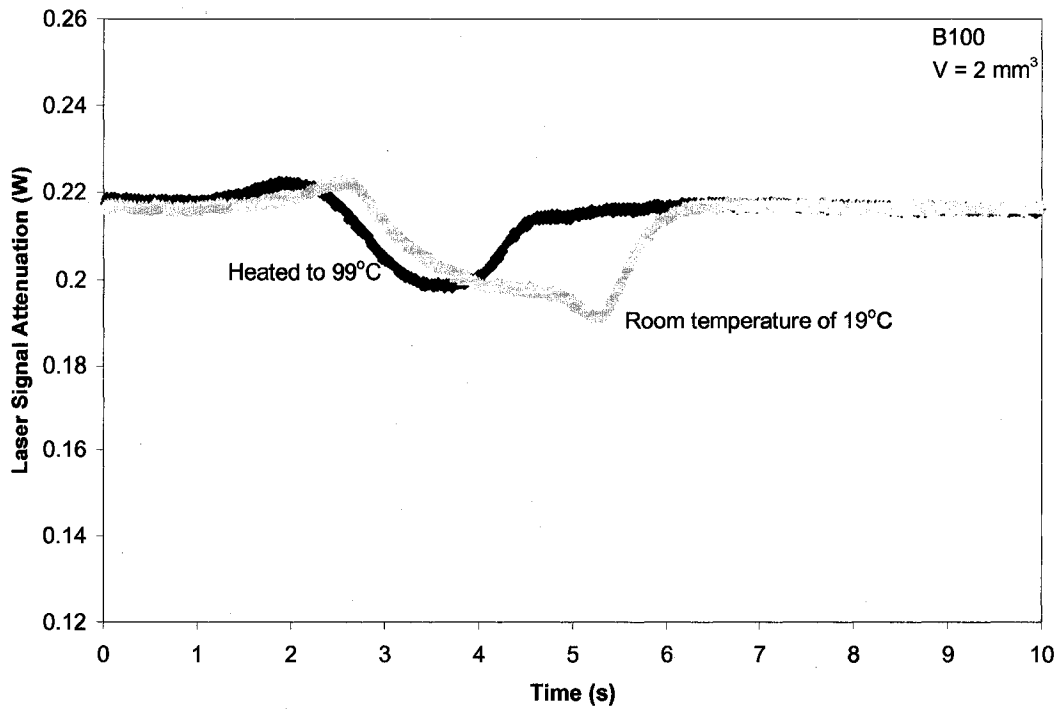
Figure 5.18 - Heated biodiesel soot profile with laser
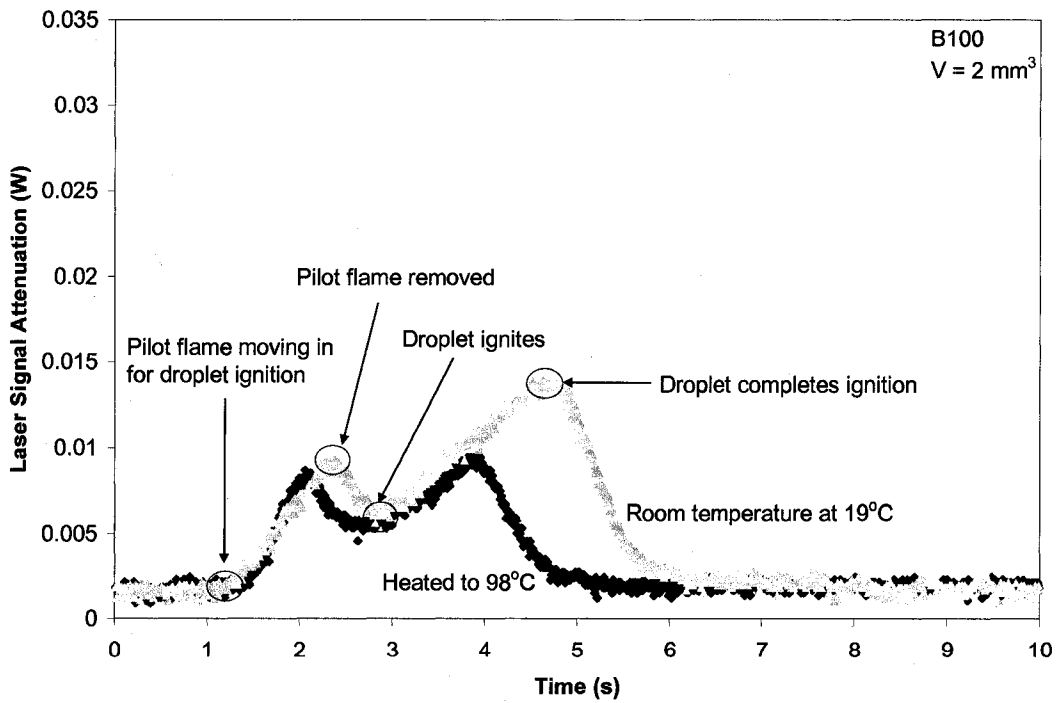
Figure 5.19 - Heated biodiesel soot profile without laser (only droplet)

32
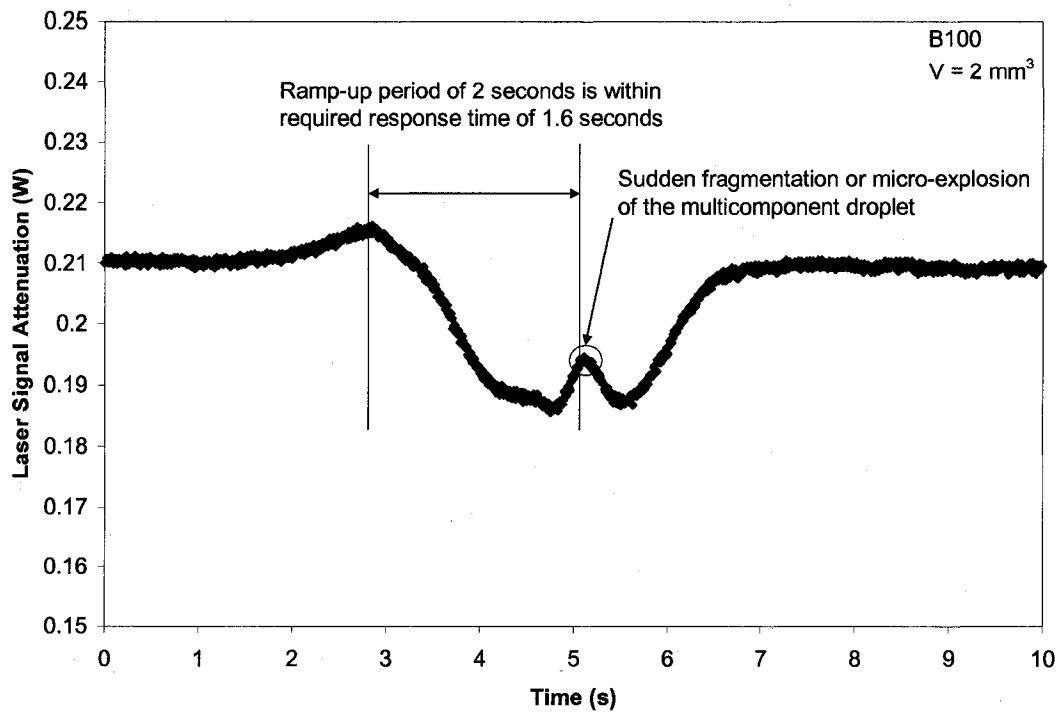
Figure 5.20 - Heated biodiesel soot profile with laser

33

Chapter 6

Results and Discussion

6.1 Liquid Temperature Measurements

Figure 6.1 exhibits the typical recorded temperature profile for all the fuels with a total observation time of *20 s*. Note that droplet lifetimes were approximately *1.6 s* from the peak temperature towards the droplet creation time *t = 0 s*. Figure 6.1 also shows the characteristic points of the temperature profiles. The figure represents the temperature profile of ethanol (it was arbitrarily chosen as an example). Point A signifies droplet ignition, while Point C denotes completion of the droplet vaporization process. Within Points B and C, the liquid phase continues to boil. It was suspected that the period between Points C and D, signifies combustion of the remainder of the vaporized fuel.

34
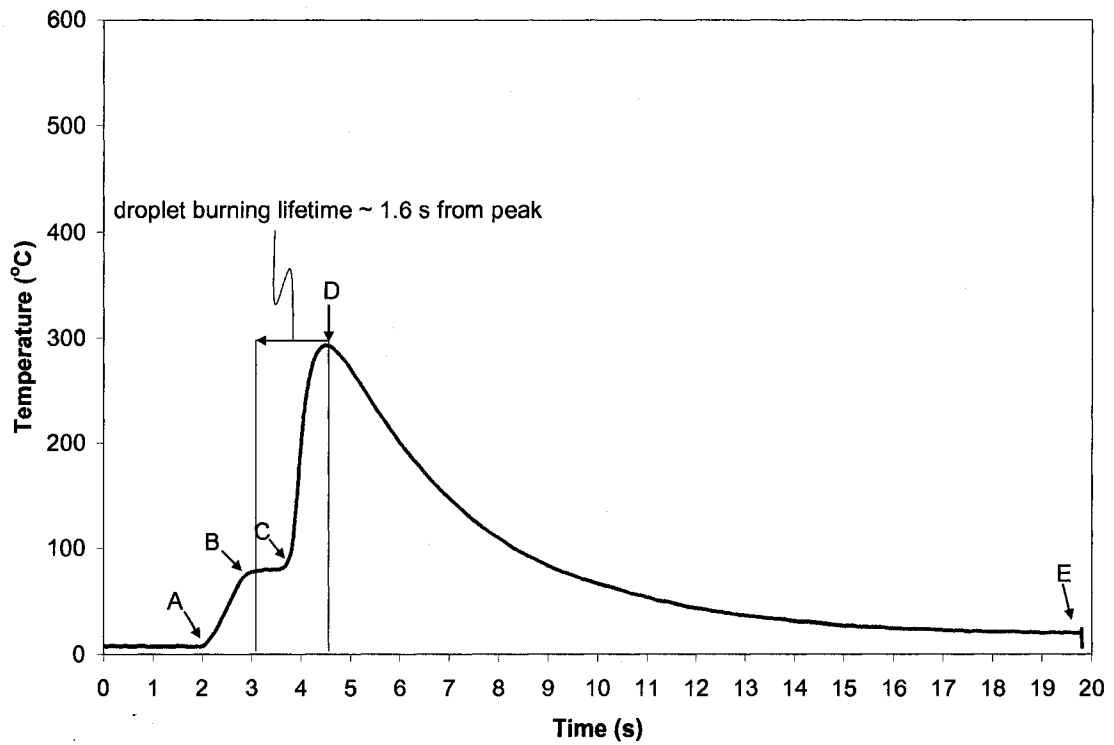
Figure 6.1 - Temperature profile highlighting characteristic points

Peak temperatures are tabulated in Table 6.1. Biodiesel had the highest peak temperature, followed by ultra low sulfur diesel, synthetic diesel, and lastly ethanol. Peak temperatures increased as higher levels of biodiesel were blended into ultra low sulfur diesel and ethanol as illustrated in Figure 6.3 to Figure 6.6.

Table 6.1 - Average peak temperatures (°C)

B100	ULSD	E100	Synthetic Diesel	50/50 ULSD/Ethanol
584	481	293	449	432

B5	B20	B50
465	476	537

B5 + Ethanol	B20 + Ethanol	B50 + Ethanol
291	443	502

All temperature profiles exhibited four characteristic points as described in Table 6.2.

35

Table 6.2 - Definition of the temperature characteristic points

Point	Observation
A → B	Warm-up (heating of the droplet to its boiling temperature) and combustion.
B → C	Combustion of the droplet with the liquid phase boiling.
C → D	Burn-off of vaporized fuel.
D → E	Thermocouple cool-down.

The boiling temperatures of biodiesel, ultra low sulfur diesel, and ethanol were within published values similar to those of Tyson [52], Maly [31], and Hodgman [18] respectively. Table 6.3 shows the measured boiling temperatures along with their associated referenced values.

Table 6.3 - Boiling temperatures of the fuels

Fuel	Boiling Temperature ($^{\circ}C$)	
	Measured	Referenced
Biodiesel	300 to 385	182 to 338
ULSD	250 to 315	186 to 337
Synthetic Diesel	180 to 300	-
Ethanol	90	78.3

Figure 6.2 graphically summarizes the measured and referenced boiling temperature ranges. The boiling temperatures for biodiesel, ultra low sulfur diesel, and ethanol tend to situate on the upper bounds of the referenced boiling temperature ranges. This was a result of conduction along the thermocouple wires from the flame. The reference range for synthetic diesel was not given. Instead, a target range similar to that of ultra low sulfur diesel was used since the synthetic diesel was designed to meet or exceed the performance of petroleum diesel.

36
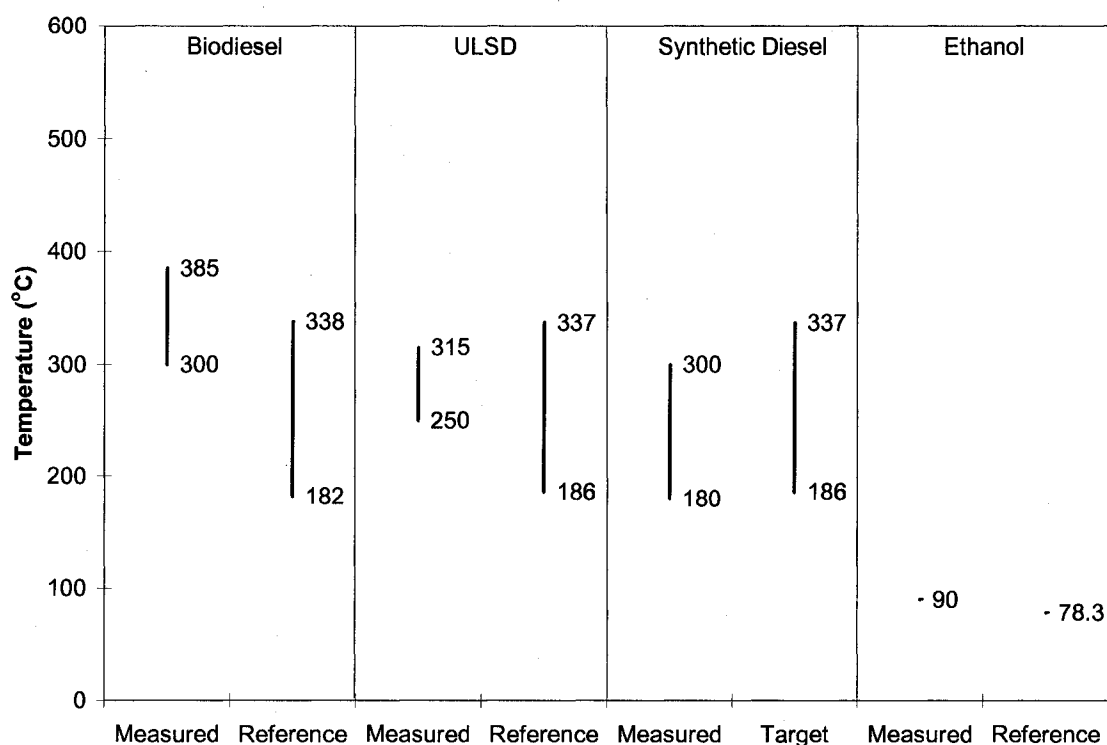
Figure 6.2 - Observed droplet boiling temperature ranges

Figure 6.3 shows the temporal variations of the droplet liquid temperature for all the fuels. Biodiesel had the highest liquid temperature while ethanol had the lowest. Figure 6.4 to Figure 6.6 displays the temperature profiles grouped by no blends, biodiesel / diesel combinations, and biodiesel / ethanol combinations.

Figure 6.4 depicts the liquid temperatures starting from lowest to highest of the no blend group. Ethanol had the lowest liquid temperature, followed by 50/50 ULSD / ethanol, synthetic diesel, ultra low sulfur diesel, and biodiesel. It should be noted that a 50 % blend of ultra low sulfur diesel and ethanol was included in this group for comparative purposes. These observations are noted on the figure where the arrow indicates increasing temperature.

In Figure 6.5, generally the liquid temperature increases as biodiesel concentration is increased. The temperature for B50 is located between the temperature of ultra low

37

sulfur diesel and biodiesel which makes sense since B50 consists of half diesel and half biodiesel.

Figure 6.6 clearly shows that liquid temperatures increase as biodiesel is blended more into ethanol. Recall, these observations are noted on the figure where the arrow indicates increasing temperature.
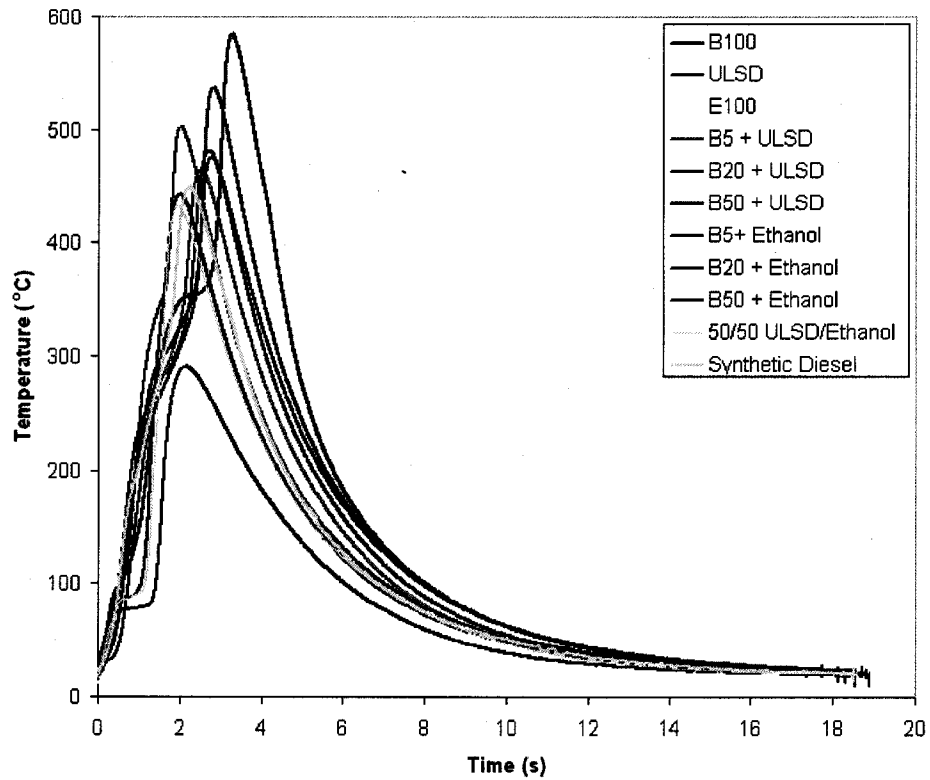
Figure 6.3 - Temporal variations of droplet liquid temperature - all fuels

38
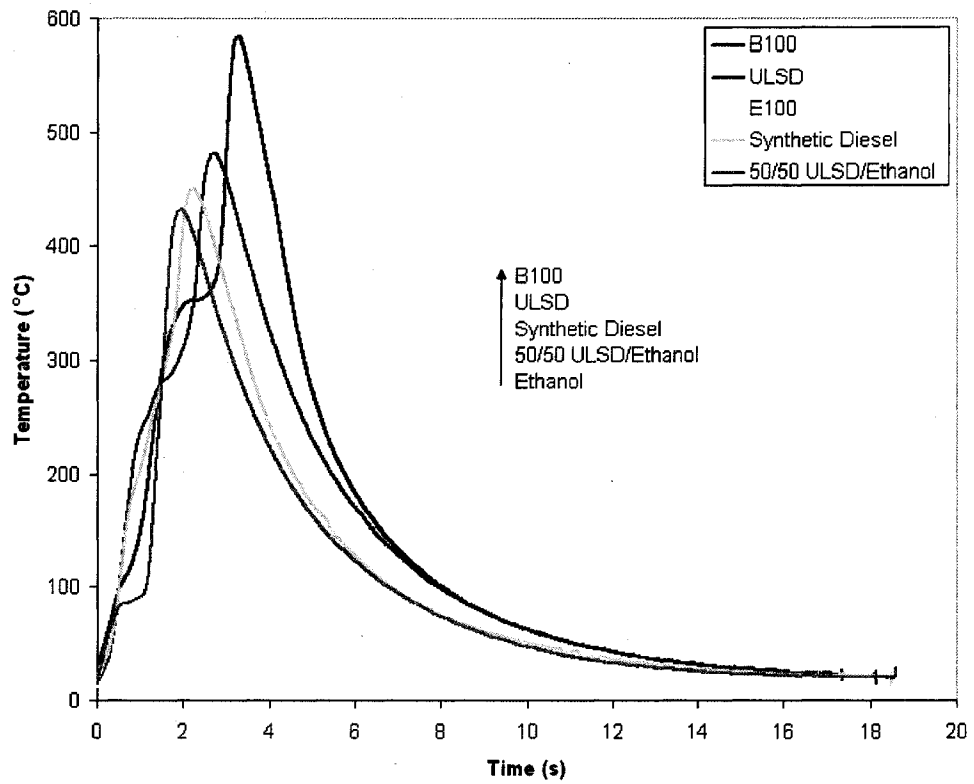
Figure 6.4 - Temporal variations of droplet liquid temperature - no blends
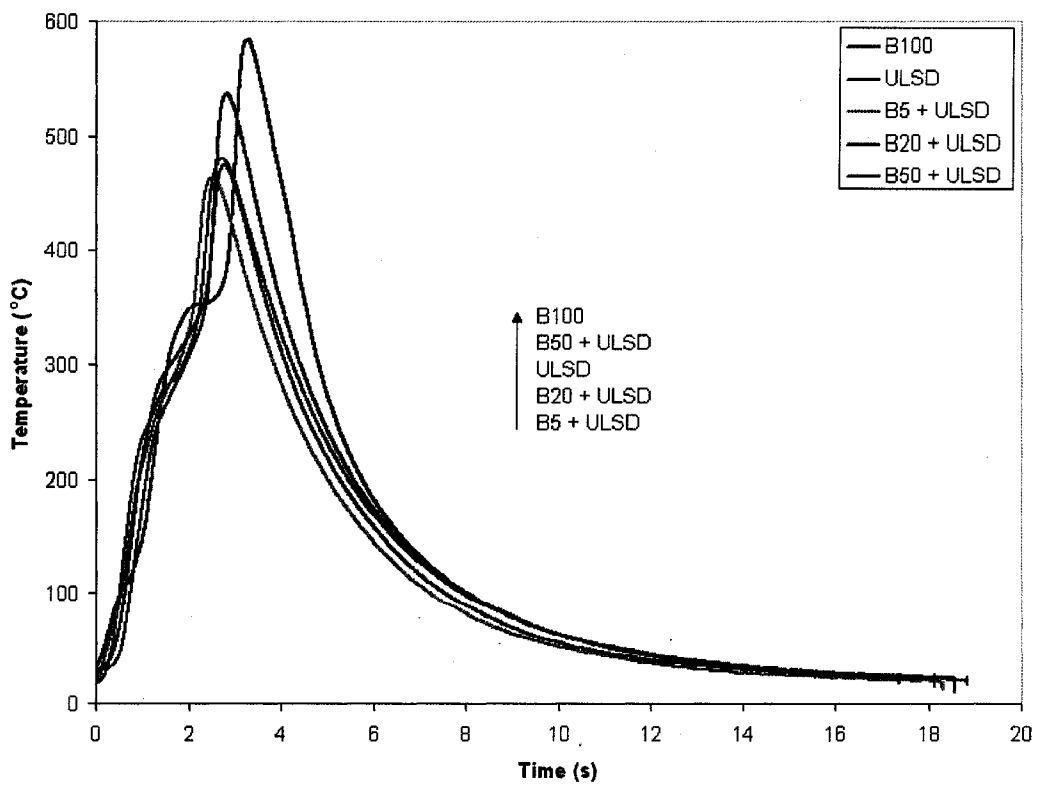
Figure 6.5 - Temporal variations of droplet liquid temperature - biodiesel/diesel combinations

39
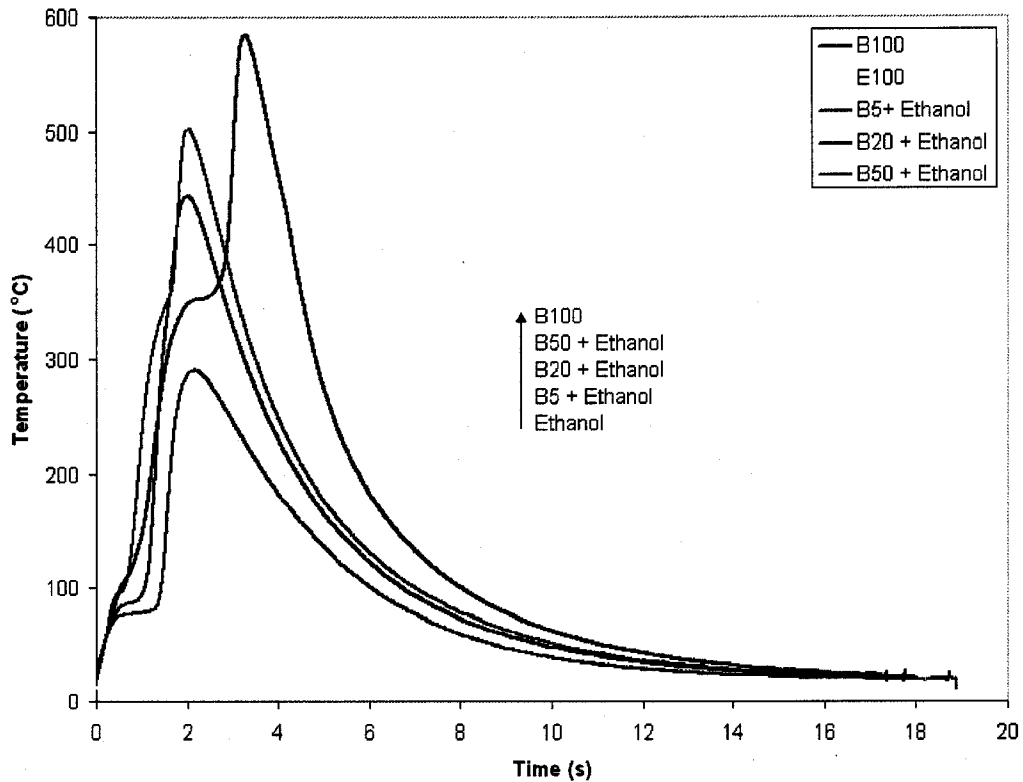
Figure 6.6 - Temporal variations of droplet liquid temperature - biodiesel/ethanol combinations

6.2 Diameter Measurements

It was conjectured that biodiesel will adhere to the D^2 relationship similar to other fuels such as ultra low sulfur diesel and ethanol.

Figure 6.7 and Figure 6.8 represents the liquid temperature profiles (with the three transient stages defined) of biodiesel and ethanol respectively. The first transient stage is the initial transient or the fuel warm-up. The burning rate constant for the first stage is a function of time and will be termed $k_1(t)$. The second transient stage is the boiling-off period or the fuel distillation curve. For multi-component fuels the burning rate constant will also be a function of time, $k_2(t)$. However, for single component fuels k_2 will be independent of time. The last stage is a function of time and is known as the final transient or the burn-off of the vapour bubble, $k_3(t)$.

40

Figure 6.9 to Figure 6.12 illustrates the burning rate constants with the transient stages (multi-staged burning rate constants) of biodiesel, ultra low sulfur diesel, ethanol and B50 respectively. The multi-staged burning rate constants were calculated for all fuels and their blends and are located in Table 6.4.

In Table 6.4, some values were missing due to insufficient amount of data except for ethanol since it is a single-component fuel with only k_2. It can be seen that the burning rate constants are quite different when comparing k that was taken over the entire droplet lifetime (Table 6.5) versus k that was taken in multiple stages (Table 6.4). For some of the fuels, the initial transient stage had values that were higher than expected. The boiling-off period had values that tend to situate on the upper range of the reviewed literature. Not all of the fuels had a final transient stage.

The burning rate constants were calculated based on the diameter measurements mentioned in this section. Specifically, a linear regression was applied to Figure 6.14 to Figure 6.17 for the entire droplet lifetime. The results of applying the linear regression yielded the burning rate constants listed in Table 6.5. In doing so, it was determined that the values presented in Table 6.5 did not accurately represent the "true" burning rate constant since Figure 6.14 to Figure 6.17 (temporal variations of the square of the diameter) or Figure 6.18 to Figure 6.21 (*normalized* temporal variations of the square of the diameter) had various transient stages. There are three transient stages which can be easily seen by observing the liquid temperature profiles in Section 6.1 and in the following two figures.

41
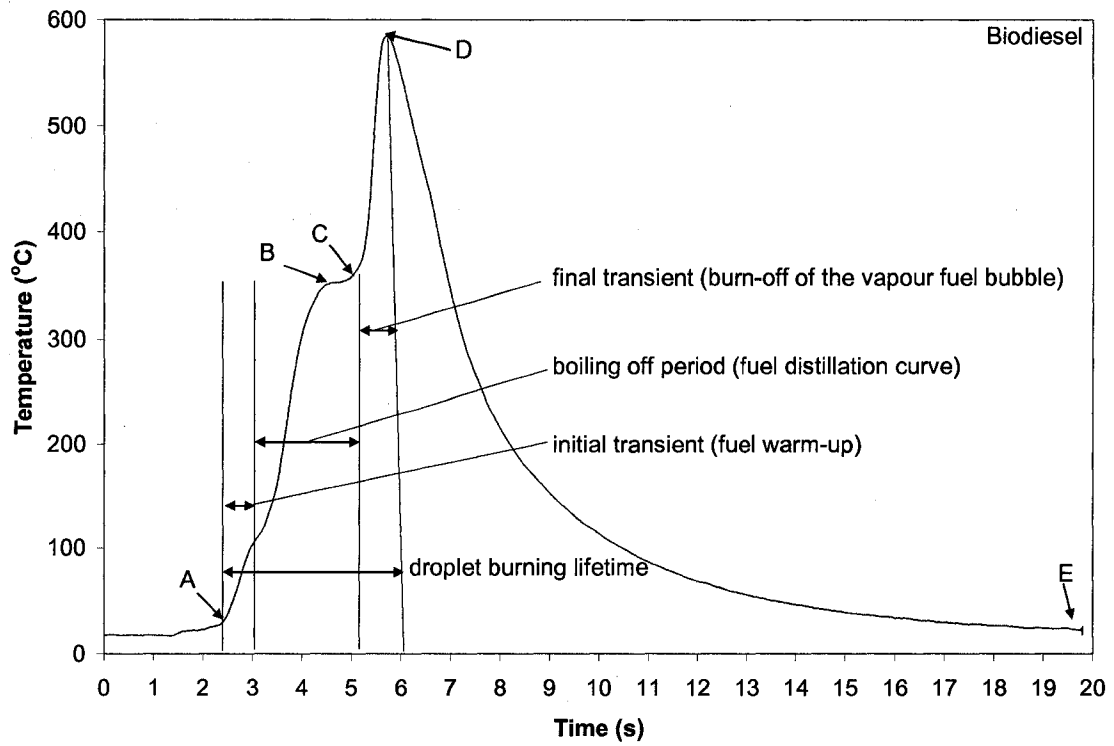
Figure 6.7 - Biodiesel liquid temperature profiles with transient stages
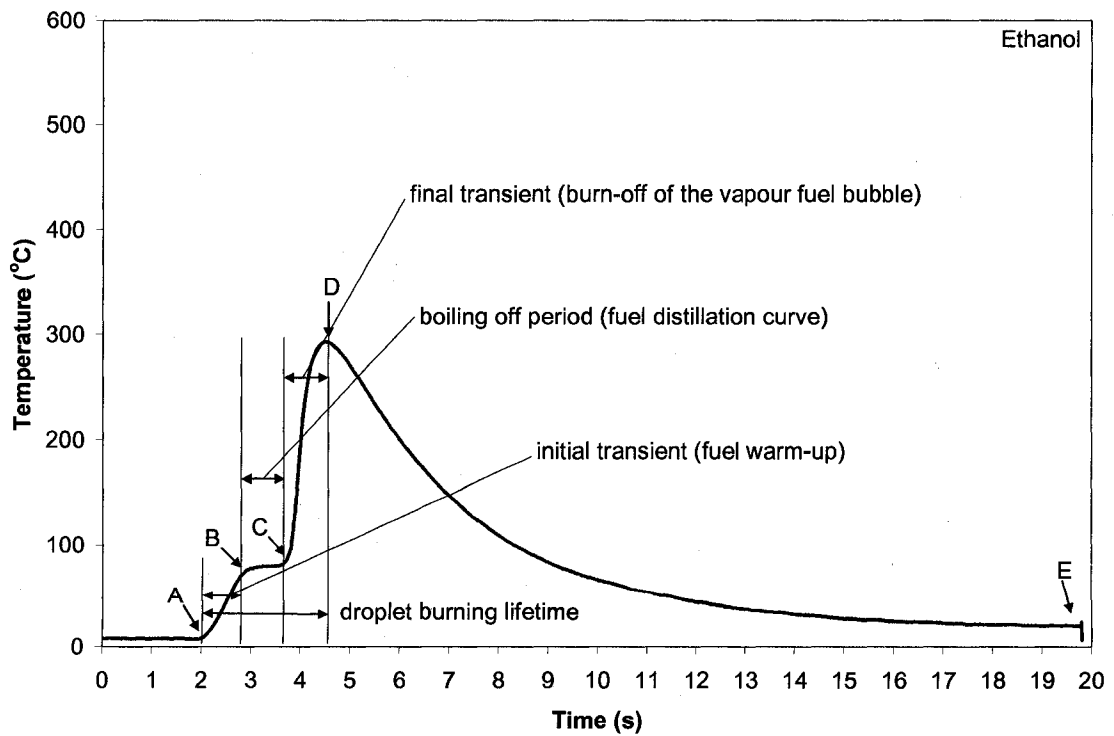
Figure 6.8 - Ethanol liquid temperature profiles with transient stages

42
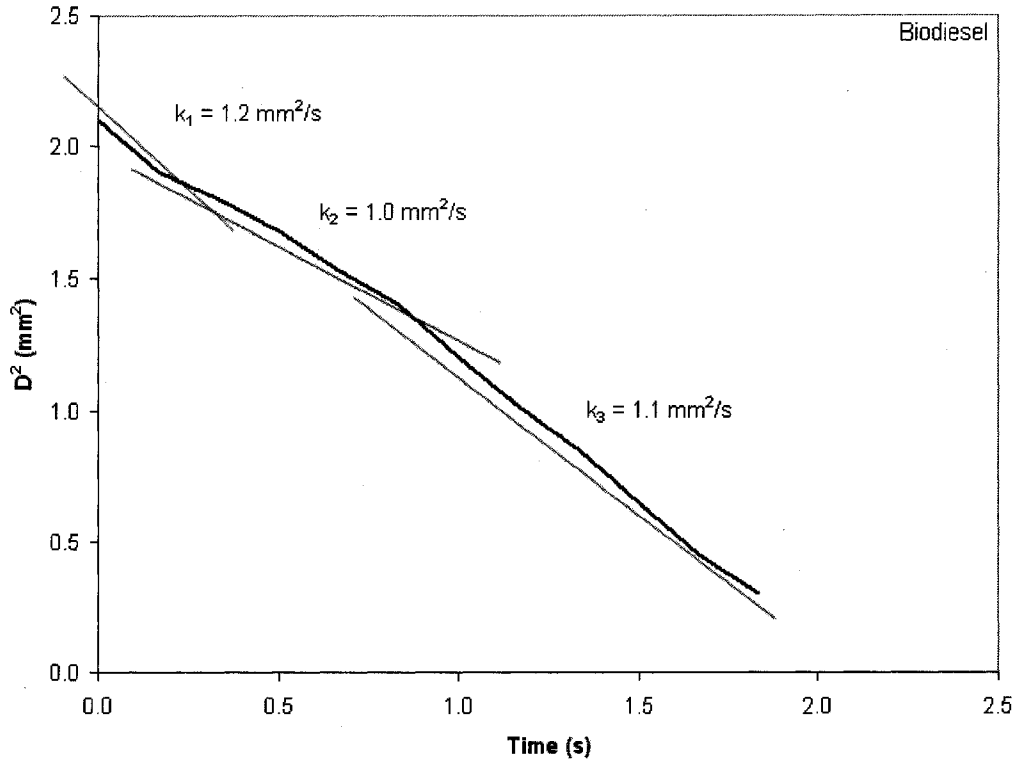
Figure 6.9 - Multi-staged burning rate constant of biodiesel

Biodiesel

$k_1 = 1.2$ mm²/s

$k_2 = 1.0$ mm²/s

$k_3 = 1.1$ mm²/s
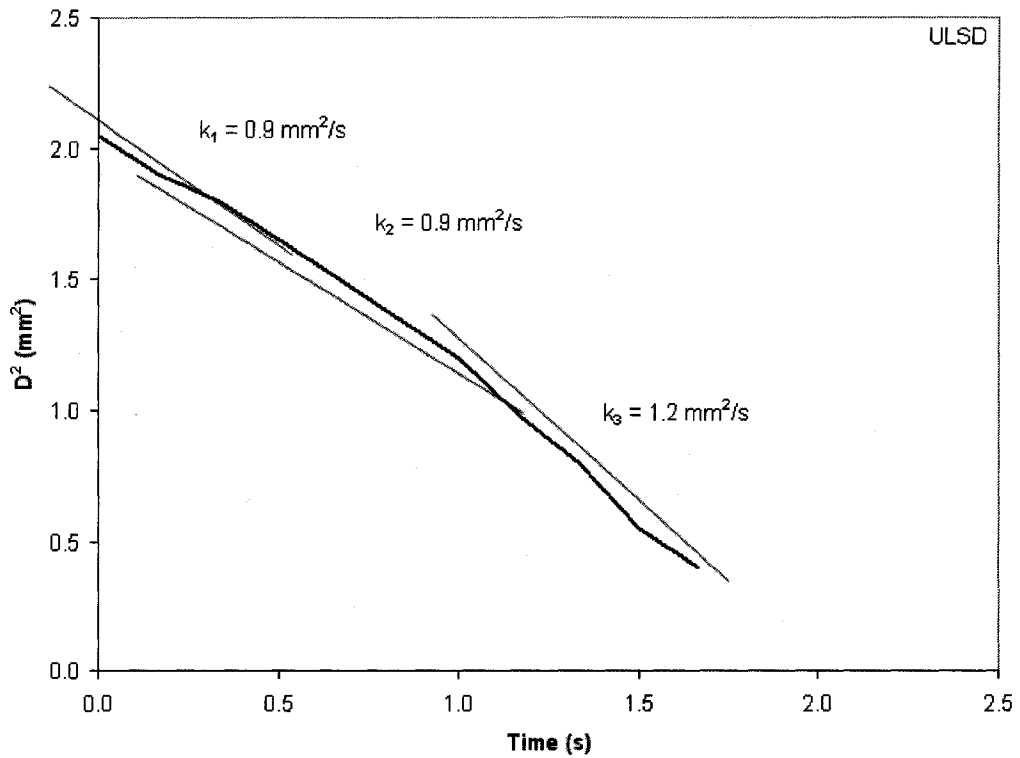
Figure 6.10 - Multi-staged burning rate constant of ULSD

ULSD

$k_1 = 0.9$ mm²/s

$k_2 = 0.9$ mm²/s

$k_3 = 1.2$ mm²/s

43
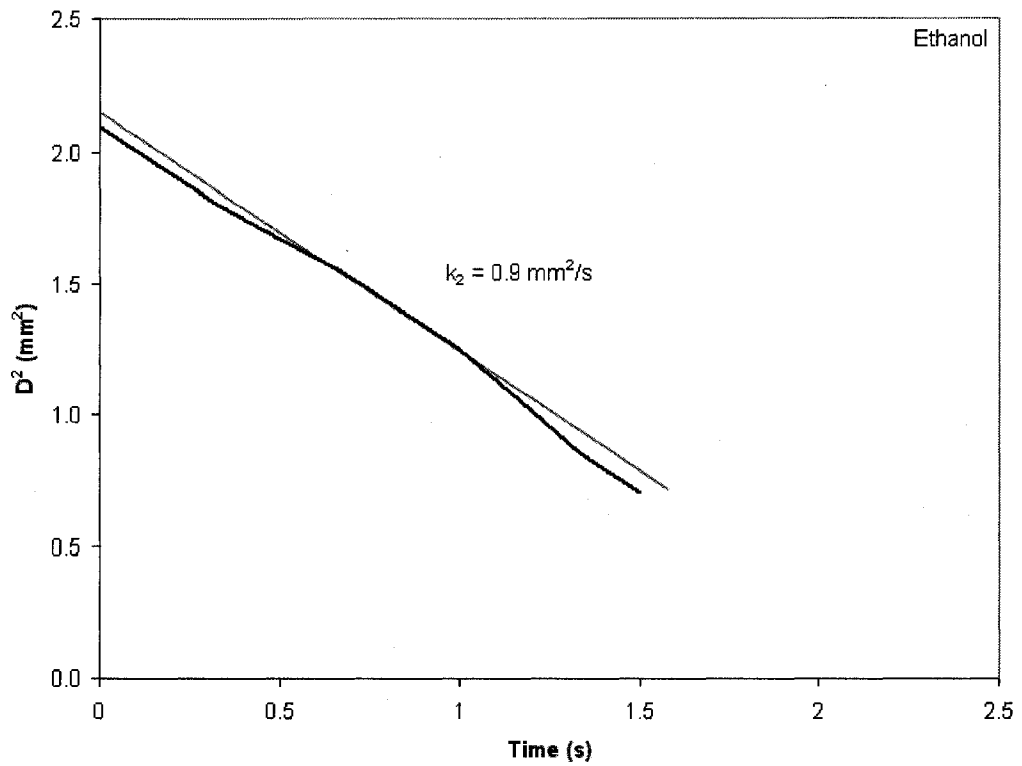
Figure 6.11 - Multi-staged burning rate constant of ethanol
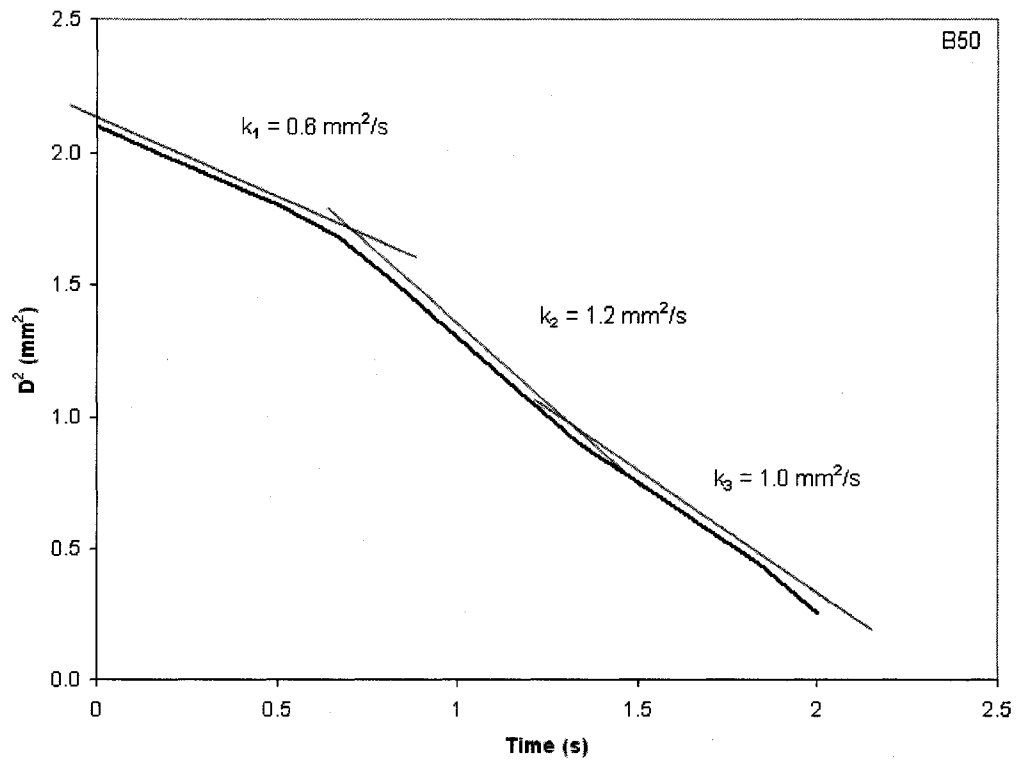
Figure 6.12 - Multi-staged burning rate constant of B50

44

Table 6.4 - Multi-staged burning rate constants (mm^2/s)

	B100	ULSD	E100	Synthetic Diesel	50/50 ULSD/Ethanol
k_1	1.2	0.9		0.8	0.6
k_2	1.0	1.2	0.9	1.2	0.9
k_3	1.1				1.2

	B5	B20	B50
k_1	0.4	0.5	0.6
k_2	1.0	1.2	1.2
k_3	1.2		1.0

	B5 + Ethanol	B20 + Ethanol	B50 + Ethanol
k_1	1.7	1.1	0.9
k_2	1.2	1.0	1.1
k_3	1.1		1.0

This following calculates the burning rate constants for the entire droplet lifetime. Figure 6.13 shows that all the fuels tested had a burning constant within the range of *0.92 mm^2/s* to *1.16 mm^2/s*. Chomiak [8] reported the burning rate constants for the majority of practical fuels fall within a narrow range of *0.70 mm^2/s* to *1.10 mm^2/s*. Makino [30] stated the burning rate constant for conventional hydrocarbon fuels is about *1.00 mm^2/s*. They observed changes of droplet diameter squared over time were linear which was confirmed from the results in Figure 6.14 and Figure 6.18. Fuels with higher molecular weight will tend to deviate from this pattern. This is due to enhanced radiant heat transfer caused by more intense soot formation for other fuels. A crucial factor affecting the burning rate is the convective gas flow around the burning droplet.

Results from previous trials using the first-generation ignition system (with free hanging electrodes) are located in the Appendices. Results reported in the main body of this thesis utilize the current ignition system (with fine-tipped fully adjustable tungsten electrodes). Photographs illustrating the differences between the two ignition systems are also located in the Appendices. The latter ignition system was chosen to prevent heat transfer and because it did not interfere with the droplets' shape.

45
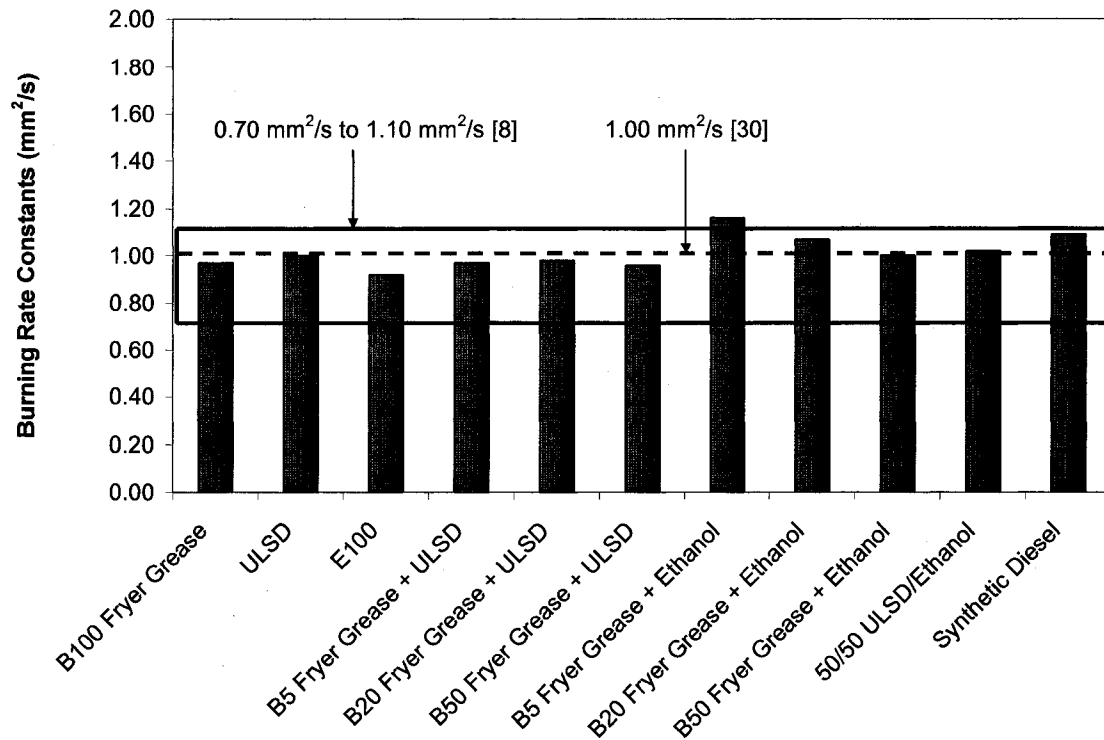
Figure 6.13 - Burning rate constants

Table 6.5 summarizes the burning rate constants taken for the entire droplet lifetime for all the fuels tested in this work.

Table 6.5 - Burning rate constants (mm^2/s)

	B100	ULSD	E100	Synthetic Diesel	50/50 ULSD/Ethanol
k	0.97	1.00	0.92	1.09	1.02

	B5	B20	B50
k	0.97	0.98	0.96

	B5 + Ethanol	B20 + Ethanol	B50 + Ethanol
k	1.16	1.07	1.00

For all the non-normalized figures (Figure 6.14 to Figure 6.17), the initial square of the diameters were different for $t = 0\ s$. This was due to the fact that the time of processing was different for each trial. Specifically, the time when the droplet is placed on the filament and the time when ignition occurs were different.

46

Figure 6.14 shows the results for all the fuels and their blends. In the following figures, the fuels were grouped into three categories (no blends, biodiesel and diesel, biodiesel and ethanol) to allow for easier viewing and interpretation of the results.
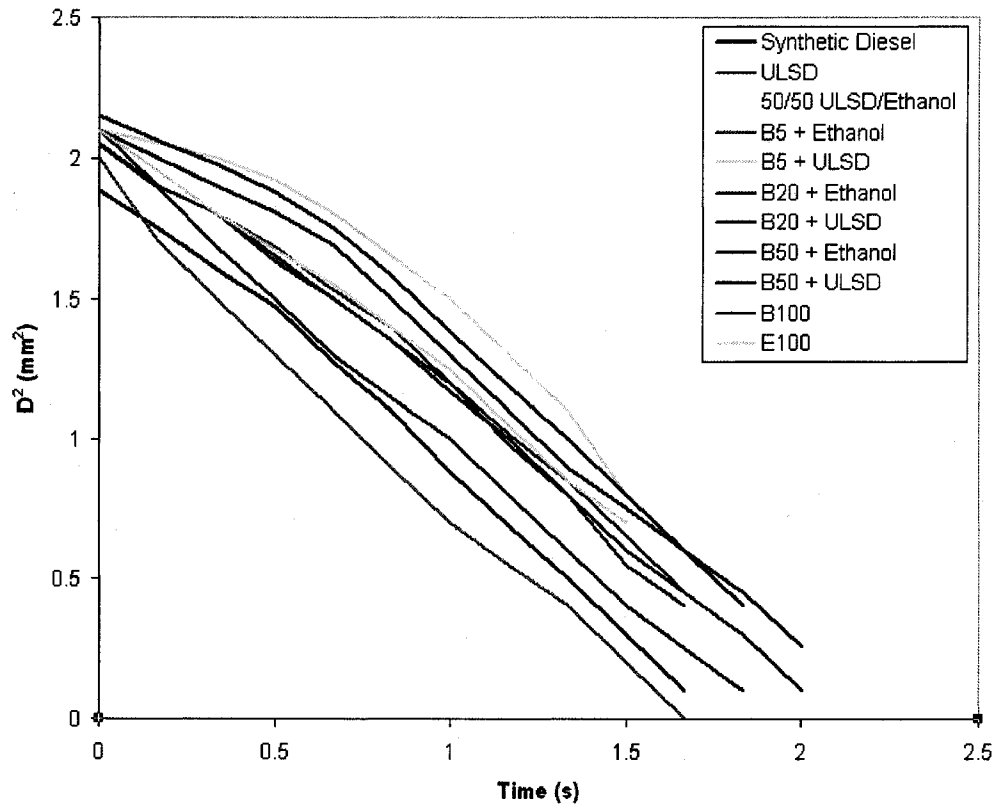
Figure 6.14 - Temporal variations of the square of the diameter - all fuels

Figure 6.15 depicts the temporal variations of the square of the diameter for the fuels with no blending. Ethanol is an alcohol and had the fastest burning rate constant of 0.92 mm^2/s, followed by biodiesel, ultra low sulfur diesel, a 50 % mixture of ultra low sulfur diesel and ethanol, and lastly synthetic diesel. Synthetic diesel had a burning rate constant of 1.09 mm^2/s similar to ultra low sulfur diesel with a rate of 1.00 mm^2/s. The differences between biodiesel and ultra low sulfur diesel are due to the fact that biodiesel is an organic multi-component fuel derived from fryer grease and ultra low sulfur diesel is a petroleum-based fuel. It should be noted that a 50 % blend of ultra low sulfur diesel and ethanol was included in this group for comparative purposes.

47
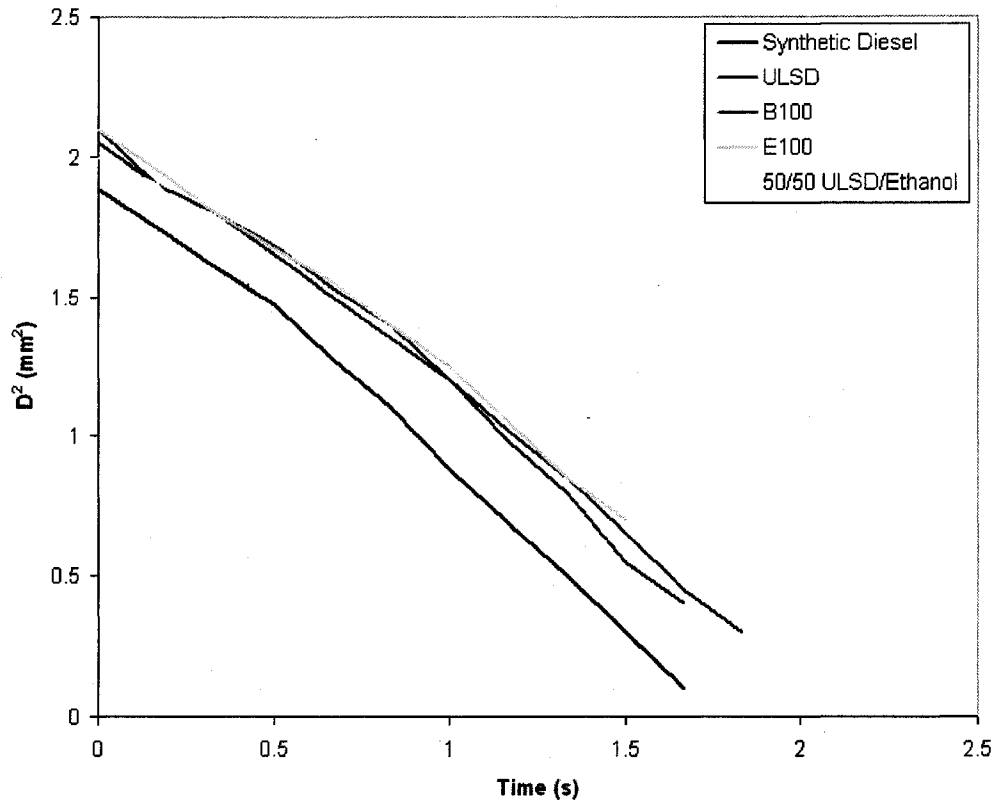
Figure 6.15 - Temporal variations of the square of the diameter - no blends

Figure 6.16 illustrates the temporal variations of the square of the diameter for the fuels with biodiesel and ultra low sulfur diesel blends. Biodiesel was added at 5 % (B5), 20 % (B20), and 50 % (B50) by volume to ultra low sulfur diesel. The droplet burning rate constant increased with the addition of biodiesel. Biodiesel had a burning rate constant of *0.97 mm²/s*, similar to ultra low sulfur diesel of *1.00 mm²/s*. It is also interesting to note that kinematic viscosities of biodiesel and ultra low sulfur diesel were fairly similar. Biodiesel and ultra low sulfur diesel had a kinematic viscosity of *3.76 mm²/s* and *3.00 mm²/s* respectively. Viscosity tends to be an important parameter with biodiesel fuels since high viscosity can lead to problems that were mentioned in the Literature Review chapter.

48
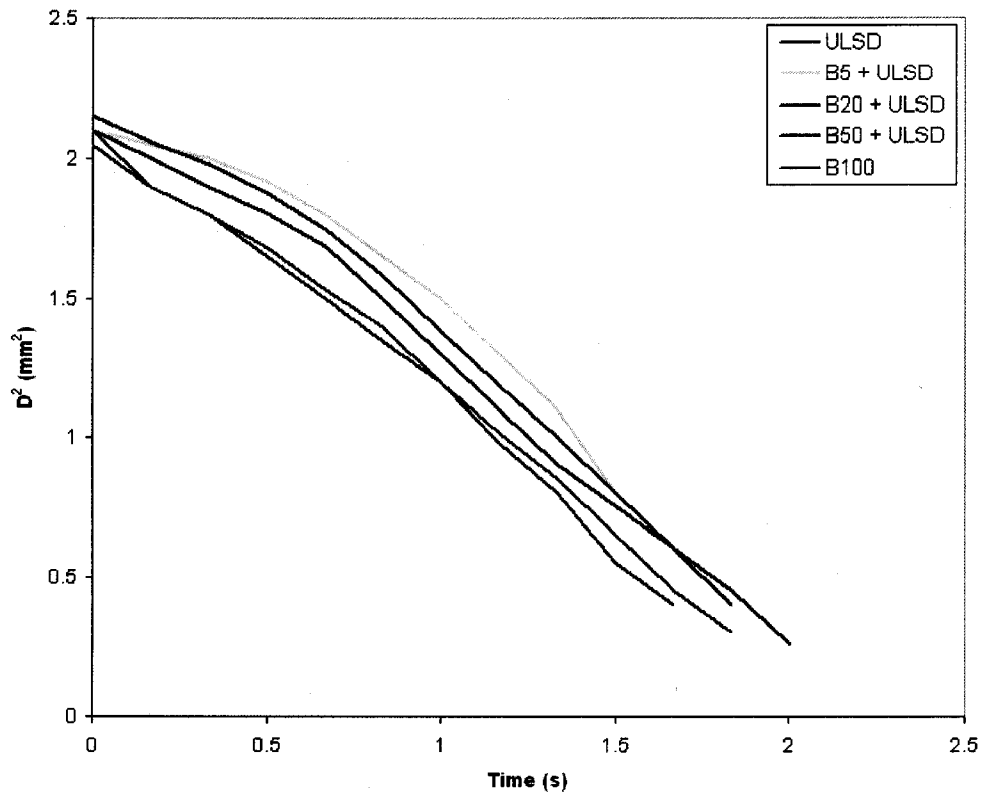
Figure 6.16 - Temporal variations of the square of the diameter - biodiesel/diesel combinations

Figure 6.17 represents the temporal variations of the square of the diameter for ethanol and biodiesel blends. Ethanol had the lowest burning rate constant followed by biodiesel. As the concentration of biodiesel decreases (while the concentration of ethanol increases), the burning rate constant also increases. It can be seen that ethanol increases the droplet burning lifetime. This is due to ethanol's lower viscosity compared to biodiesel. Ethanol has a kinematic viscosity of *1.08 mm²/s* while biodiesel has a kinematic viscosity of *3.76 mm²/s*.
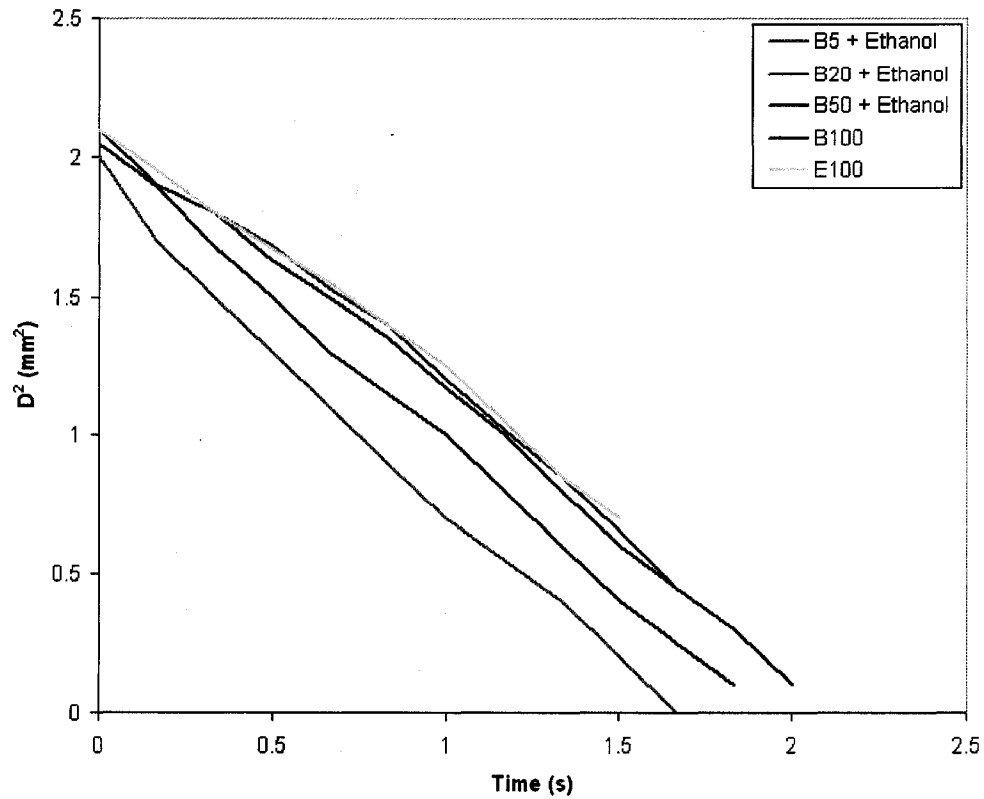
49

Figure 6.17 - Temporal variations of the square of the diameter - biodiesel/ethanol combinations

Figure 6.18 to Figure 6.21 are the normalized versions of the temporal variations of the square of the diameter. All the figures were normalized by the square of the diameter at the first measurement location which was the first image sequence frame under consideration. Shaddix [43] took the same approach. It can be noted that at $D^2/D_o^2 = 0$, the droplet completes combustion. The combustion duration ranged from *1.5 s to 2.0 s*. This was due to the fact that the time of processing was different. Specifically, the time when the droplet is placed on the filament and the time when ignition occurs were different. At $t = 0 s$, $D^2/D_o^2 = 1$ which indicates that the volume was held constant by the Chaney adapter. In the following figures, the fuels were grouped into three categories (no blends, biodiesel and diesel, biodiesel and ethanol) to allow for easier viewing and interpretation of the results.

50
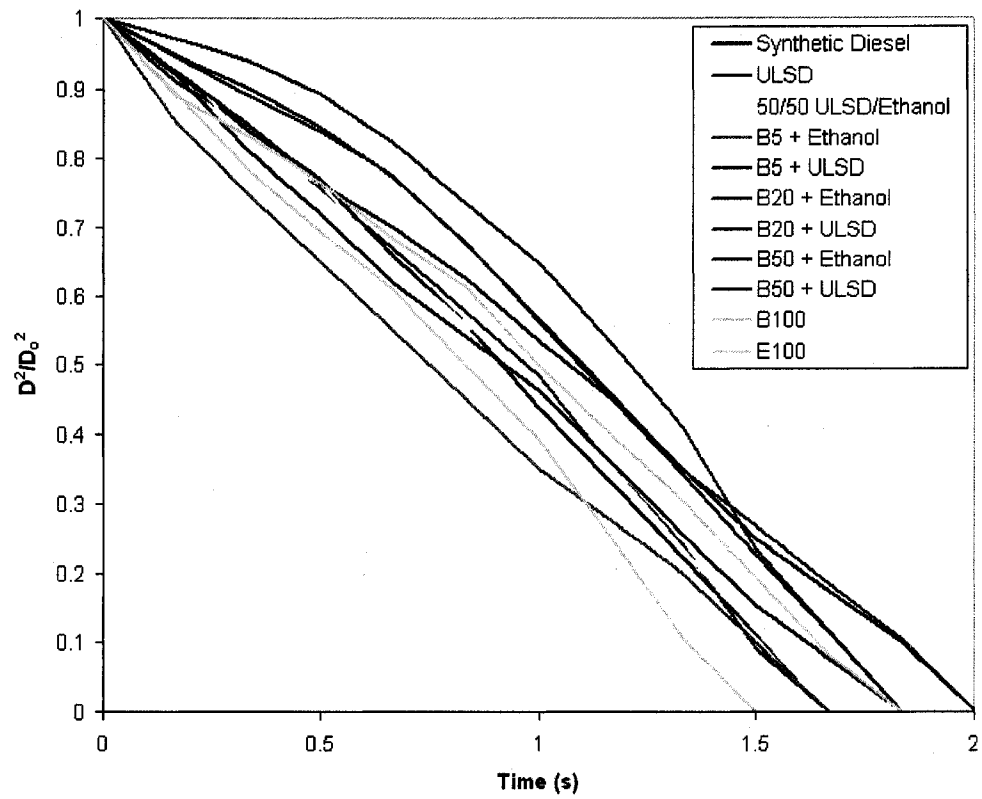
Figure 6.18 - Normalized temporal variations of the square of the diameter - all fuels
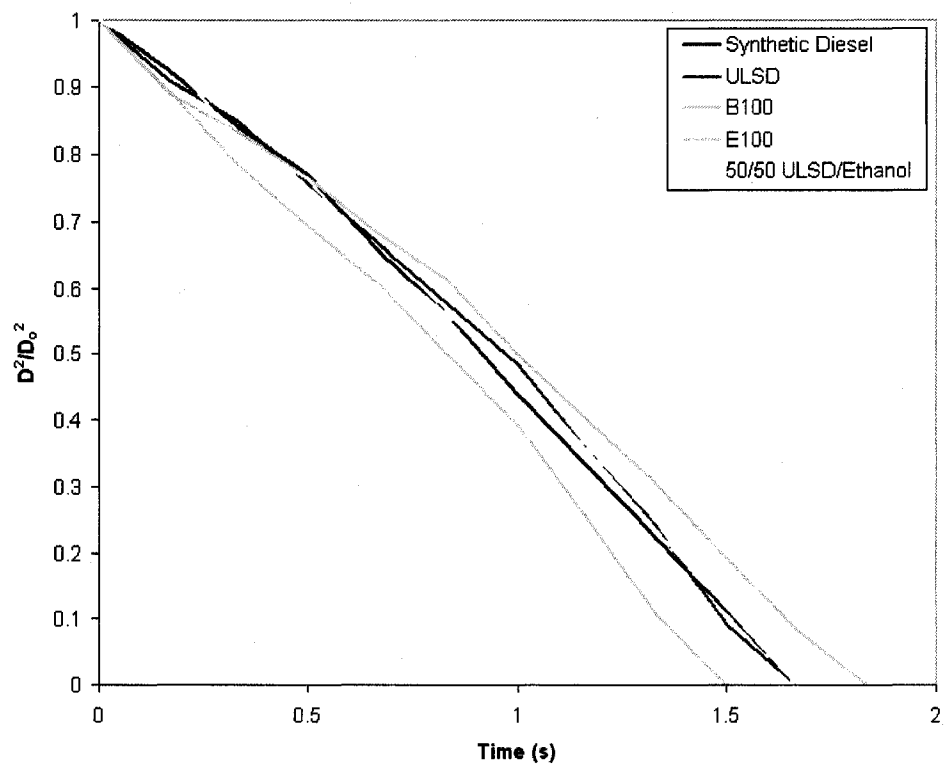
Figure 6.19 - Normalized temporal variations of the square of the diameter - no blends

51
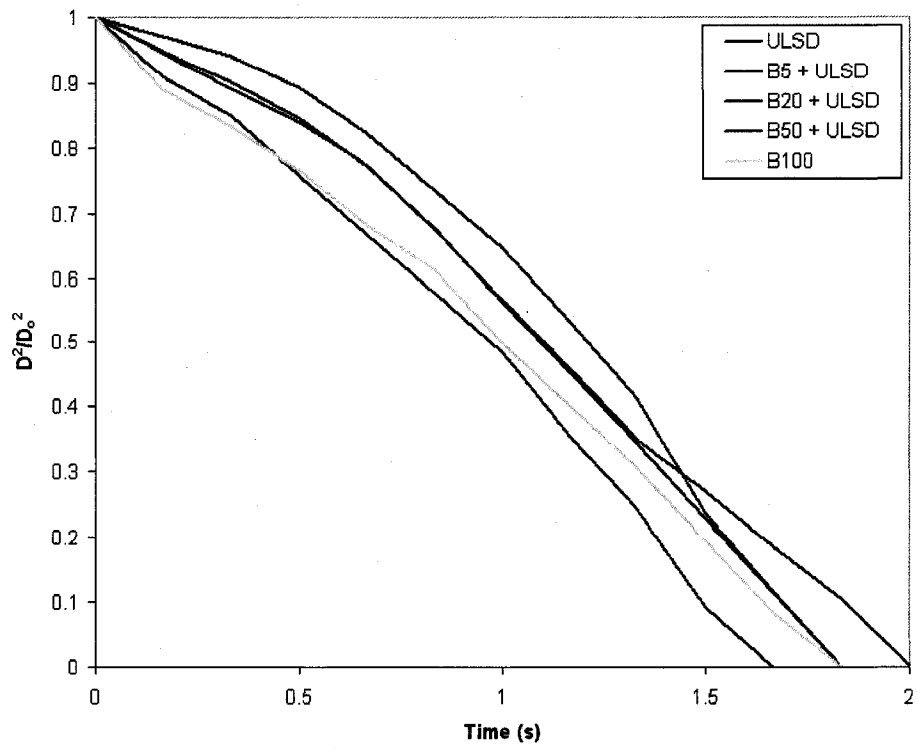
Figure 6.20 - Normalized temporal variations of the square of the diameter - biodiesel/diesel combinations

Figure 6.21 - Normalized temporal variations of the square of the diameter - biodiesel/ethanol combinations

52
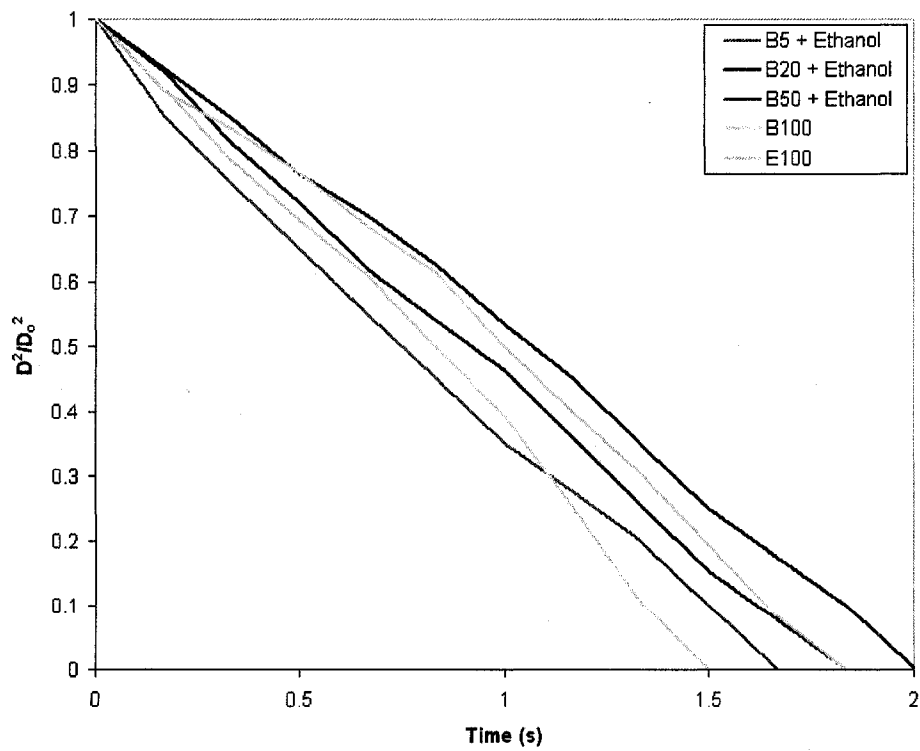
6.3 Flame Diameter Measurements

Figure 6.22 to Figure 6.25 depicts the temporal variations of the flame diameter and the flame / droplet diameter ratio. The axis on the left represents the droplet flame diameter D_f and the axis on the right represents the droplet flame diameter / droplet diameter ratio D_f/D. The droplet flame diameter is defined as the maximum edge length of the flame perpendicular to the falling direction as illustrated in Figure 5.5. From Figure 6.22 to Figure 6.25, it can be seen that the droplet flame diameter first increases then displays a gradual descent until flame extinction occurs. This observation is readily apparent in droplet combustion for conventional hydrocarbons as mentioned by Makino [30]. Law [27] stated that the droplet flame diameter / droplet diameter ratio exhibits a progressive exponential increase until the droplet fully combusts which conforms well to the results obtained in this thesis. This progressive exponential increase in D_f/D is a common occurrence for combustion in an air environment where the oxygen concentration is *21 %*. What is of particular interest is when combustion occurs under high oxygen concentration where the oxygen mass fraction is *0.33*. In this scenario, D_f/D will display a similar trend to D_f (a concave downwards function). A low oxygen atmosphere occurs when the oxygen mass fraction is *0.11*. In this environment, D_f/D will also display a similar trend to D_f (a concave downwards function) however D_f/D will steadily converge towards D_f [30].

Regardless of oxygen concentrations, the D^2 law will always apply. Also, it was observed by Law [27] that there is a direct correlation between oxygen concentration, flame luminosity, and flame location. Increasing the oxygen concentration will increase flame luminosity and will increase the flame location from the droplet surface (the flame will be farther away from the droplet surface).

In Figure 6.22, it can be observed that at *t = 0 s*, the flame diameters for all the fuels were different. This was due to the fuels chemical composition and nature of the specific fuel. The flame diameters were in the range of *2.5 mm* to *3.3 mm*.

53
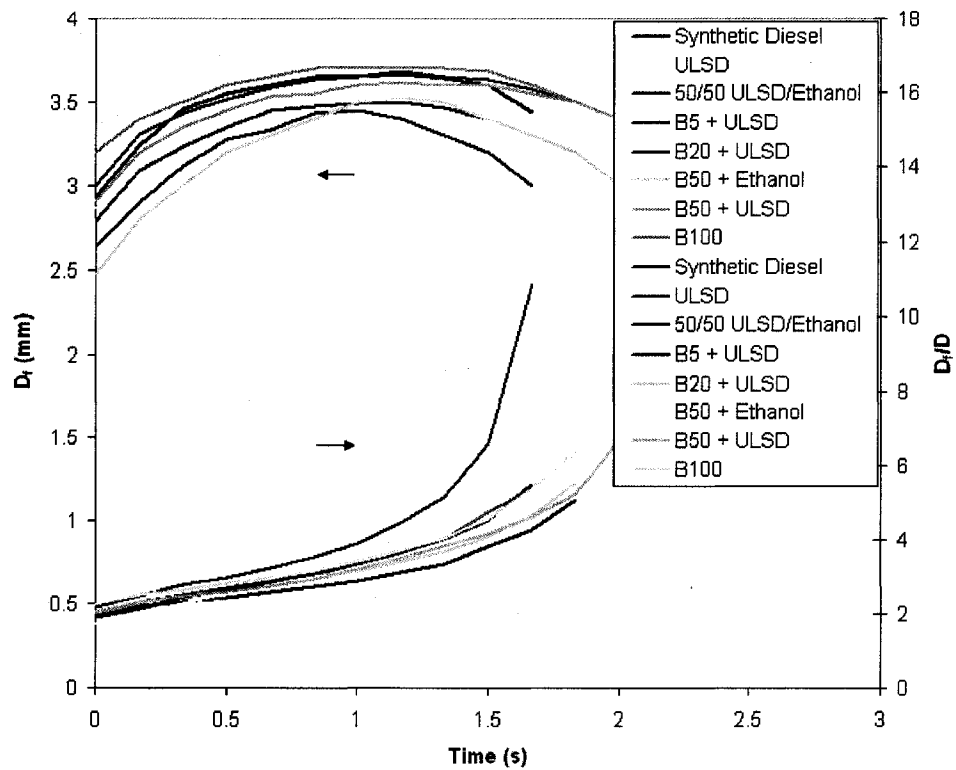
Figure 6.22 - Temporal variations of flame diameter and flame/droplet diameter ratio - all fuels

Figure 6.23 shows the variation of the flame diameter and flame / droplet diameter ratio over time of the non-blended fuels tested. Biodiesel had the largest flame diameter followed by synthetic diesel, ultra low sulfur diesel, and lastly a 50 % mixture of ultra low sulfur diesel and ethanol. Ethanol had a very weak and faint flame (the flame was not as pronounced as the other fuels) which made data processing very difficult because of the optical issues with the camera lens. It should be noted that a 50 % blend of ultra low sulfur diesel and ethanol was included in this group for comparative purposes.

54
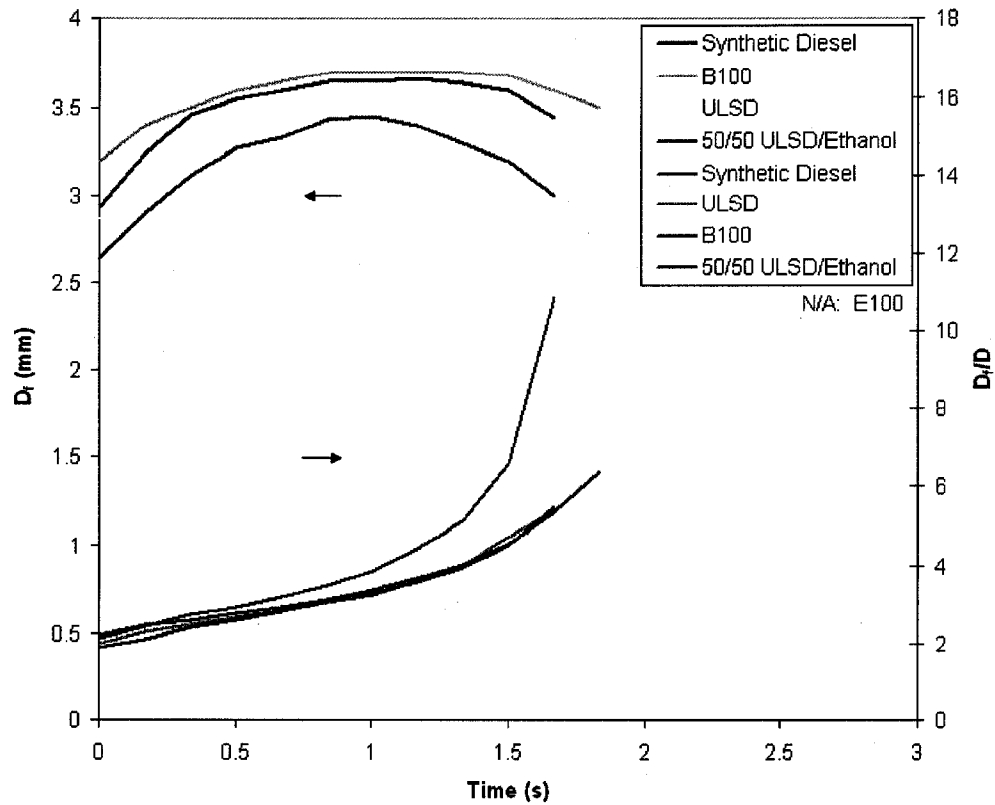
Figure 6.23 - Temporal variations of flame diameter and flame/droplet diameter ratio - no blends

Figure 6.24 illustrates the variation of the flame diameter and flame / droplet diameter ratio over time of the biodiesel and diesel fuel combinations. Biodiesel had the largest flame diameter followed by B20 (20 % biodiesel with 80 % diesel), B50, ultra low sulfur diesel, and lastly B5. Biodiesel and ultra low sulfur diesel had the highest flame/droplet diameter ratios. As biodiesel concentration decreased while ultra low sulfur diesel concentration increased, their respective ratios decreased. In other words, ratios decreased with the addition of ultra low sulfur diesel fuel.

55
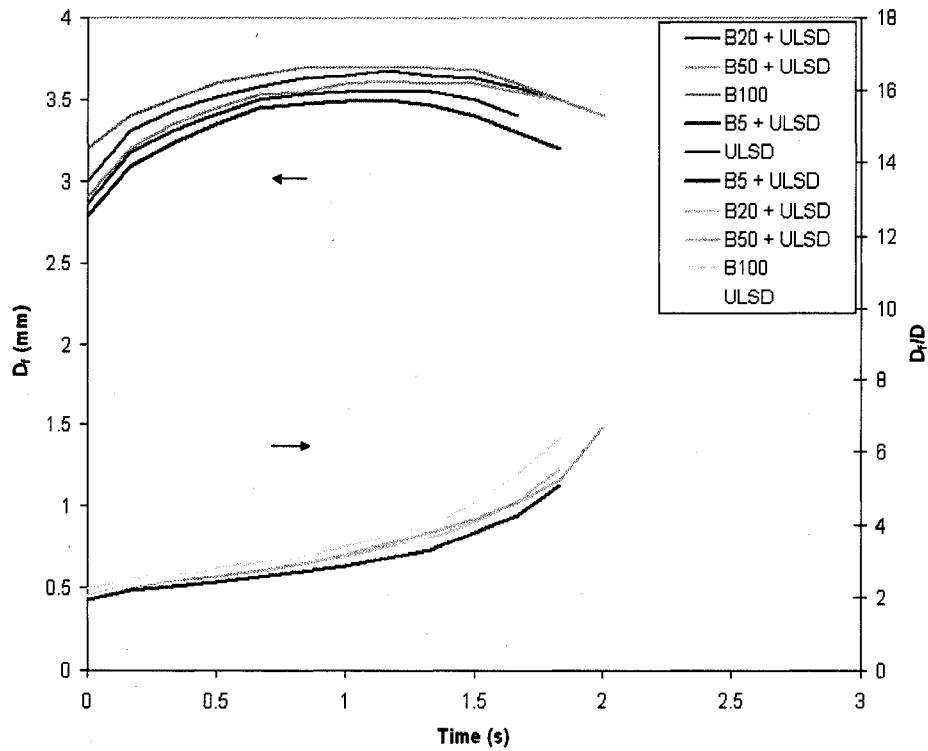
Figure 6.24 - Temporal variations of flame diameter and flame/droplet diameter ratio - biodiesel/diesel combinations

Figure 6.25 depicts the variation of the flame diameter and flame / droplet diameter ratio over time of the biodiesel / ethanol fuel combinations. Ethanol had a very weak and faint flame (the flame was not as pronounced as the other fuels) which made data processing difficult because of the optical issues with the camera lens. Only biodiesel and a 50 % mixture of biodiesel and ethanol were able to be analyzed. Biodiesel had a larger flame diameter and flame / droplet diameter ratio than the 50 % mixture of biodiesel and ethanol. From Figure 6.25, one can delineate that with lower concentrations of biodiesel (while increasing ethanol concentrations), both the flame diameter and flame / droplet diameter ratio will decrease.

56
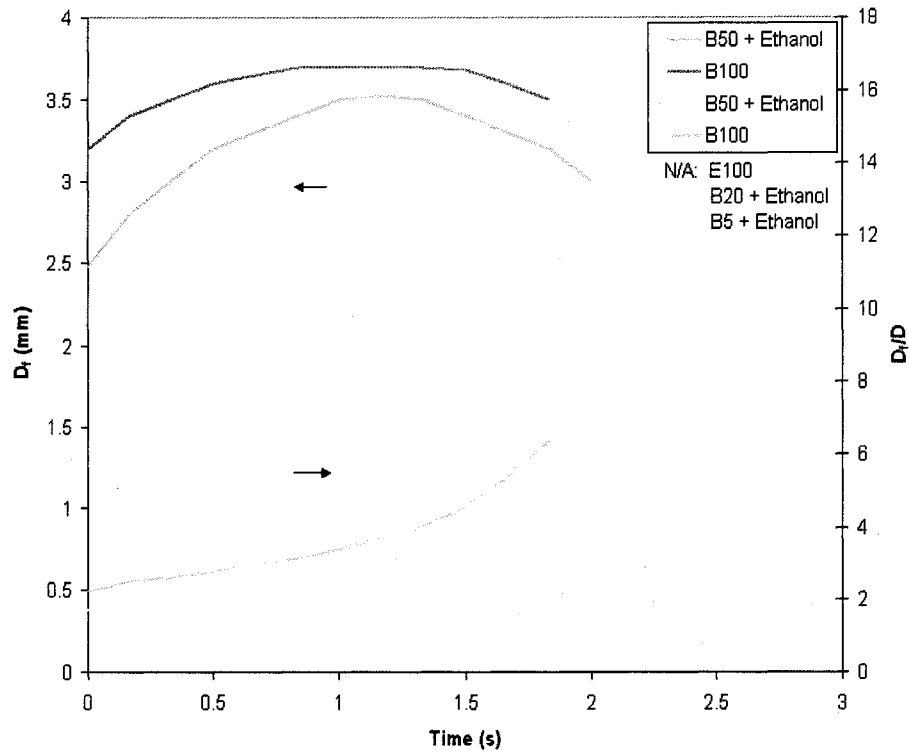
Figure 6.25 - Temporal variations of flame diameter and flame/droplet diameter ratio - biodiesel/ethanol combinations

6.4 Flame Temperature Measurements

Maximum flame temperatures were recorded on the vertical axis of the flames at increasing heights. Each point on the flame temperature profiles represents an average of ten maximum temperatures recorded in ten consecutive trials at a given location.

In Figure 6.26, the flame temperatures coincided with typical flame temperatures mentioned in Strehlow [50] and Glassman [15]. It was observed that flame temperatures increased and peaked at a certain spatial point, then gradually decreased with increasing height. This makes sense since the flame tip has the highest temperature. As one moves further away from the vicinity of the flame tip, temperature will gradually decrease until thermal radiation from the flame will be negligible. The highest flame temperatures appeared between *4 mm* and *6 mm* above the centre of the drop.

57

Figure 6.27 shows the flame temperature at increasing spatial points for the fuels with no blends. It can be seen that synthetic diesel and ultra low sulfur diesel had similar flame temperature profiles. This was expected since synthetic diesel was designed to mimic the characteristics of petroleum diesel.

In Figure 6.28 (biodiesel and diesel combinations) and Figure 6.29 (biodiesel and ethanol combinations), higher flame temperatures are clearly evident as the concentration of biodiesel is increased. The arrow represents increasing biodiesel content. Senatore [42] stated that the presence of oxygen in biodiesel contributes to a very fast combustion, but produces high temperatures. Biodiesel and ethanol had an oxygen content of 11 % and 35 % respectively. Increasing biodiesel in ultra low sulfur diesel will cause oxygen content to increase which will result in higher temperature. Oxygen content is only one factor that causes high temperatures. On the contrary, increasing biodiesel in ethanol will actually lower oxygen content - but, temperature increases. This is due to the complex chemical interactions that are a result of mixing of biodiesel and ethanol together. It can be generalized that increasing the concentration of biodiesel to ultra low sulfur diesel or ethanol will cause an increase in the droplet flame temperature.
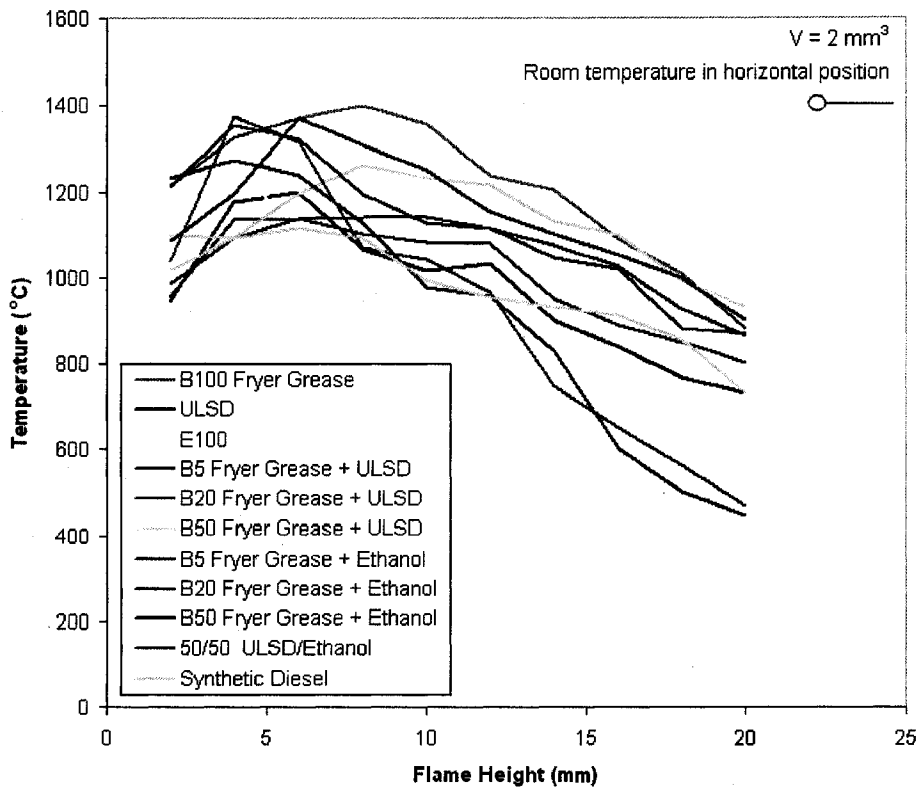
Figure 6.26 - Flame temperature at increasing spatial points - all fuels
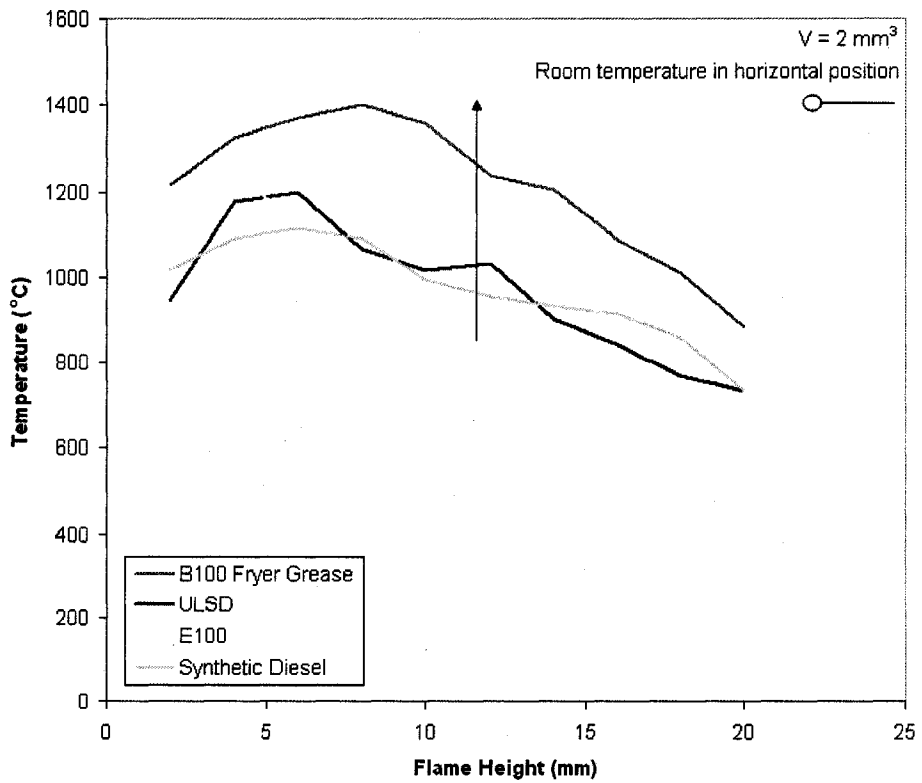
Figure 6.27 - Flame temperature at increasing spatial points - no blends

59
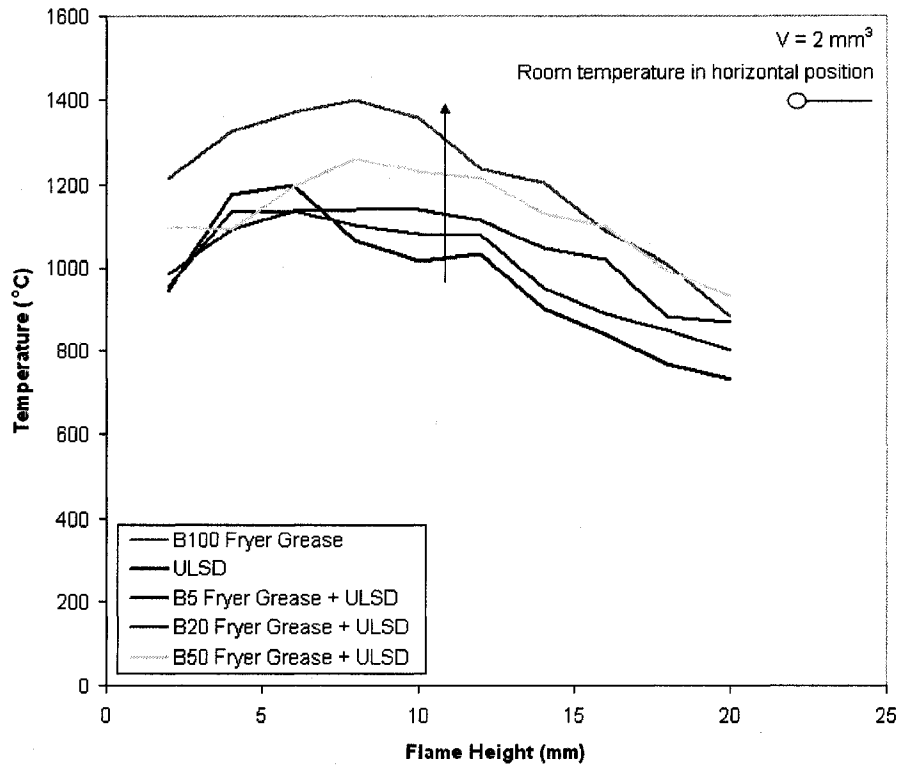
Figure 6.28 - Flame temperature at increasing spatial points - biodiesel/diesel combinations
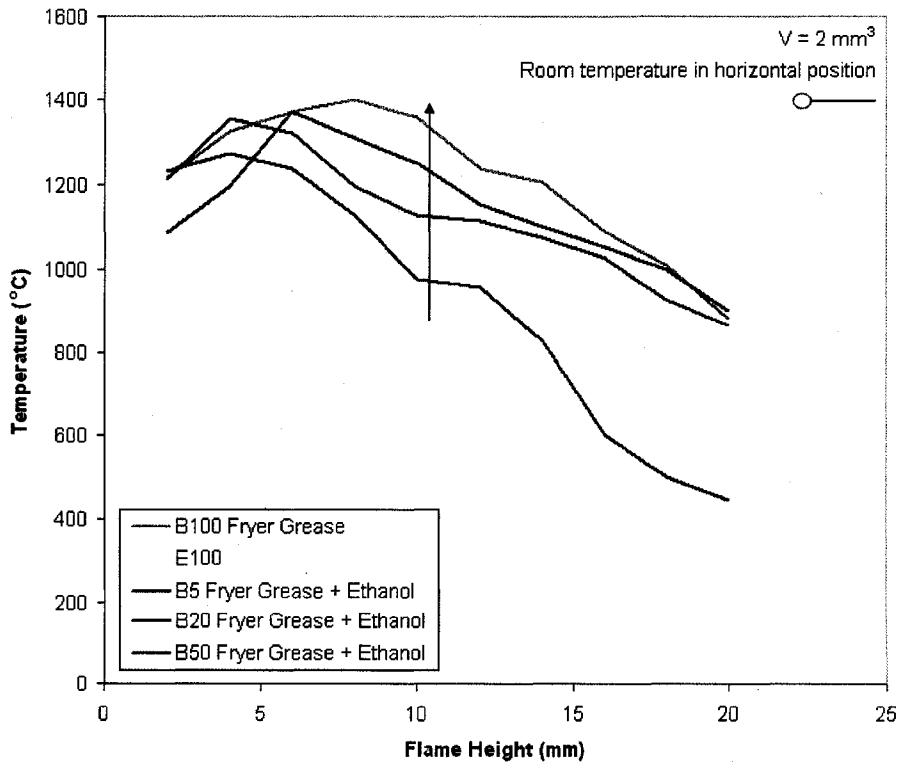
Figure 6.29 - Flame temperature at increasing spatial points - biodiesel/ethanol combinations

60

Figure 6.30 illustrates the droplet flame temperature at the bottom of the droplet. Recall, Figure 5.10 shows the positioning of the S-type thermocouple. In Figure 6.30, the droplet flame temperatures below the droplet were similar to the trends found in the peak temperatures from the droplet liquid temperatures. Biodiesel had the highest flame temperature, followed by ultra low sulfur diesel, synthetic diesel, and lastly ethanol. The synthetic diesel had a similar droplet flame temperature to ultra low sulfur diesel. It can be noted that flame temperatures increased as higher levels of biodiesel were blended into ultra low sulfur diesel and ethanol.
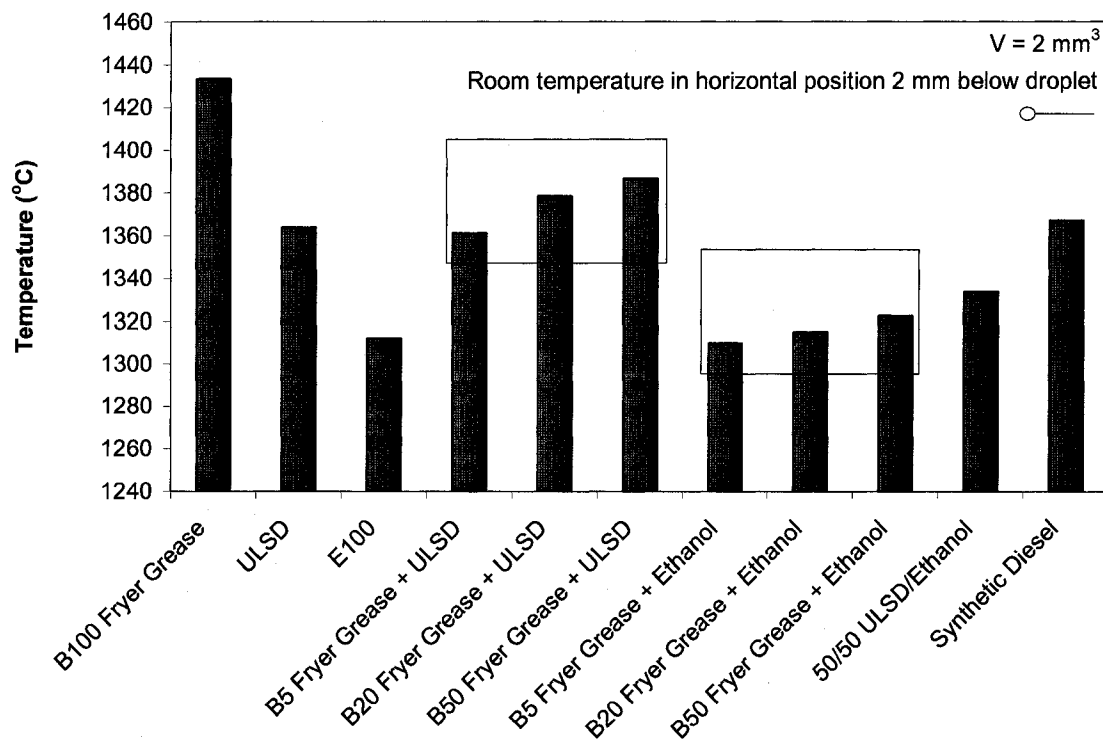
Figure 6.30 - Flame temperature at lower region - all fuels

6.5   Flame Transmisivity Measurements

As stated earlier in the Methodology and Procedures chapter, flame transmisivity measurements are representative of sooting characteristics and are a precursor to quantifying soot volume fraction measurements.

61

A fuel's structure has a significant effect on its sooting characteristics. Fuels with the tendency to soot more are aromatics, followed by alkynes, alkenes, and lastly alkanes. Examples of these highly sooty fuels are benzene, acetylene, ethylene, and methane respectively. Soot is usually found in hydrocarbon fuels, giving the flame its typical orange or yellow color due to the spectral sensitivity of the human eye. The formation of soot is dependent on the diffusion of hydrogen atoms. Soot is formed on the fuel side of the reaction zone and is consumed when it flows into an oxidizing region, such as the flame tip. Soot also contributes to radiant heat losses from flames, with peak emission at wavelengths in the infrared region of the spectrum. However, a flame may have some visible luminosity from soot where the contribution of soot radiation to the radiant heat loss may be insignificant.

Figure 6.31 illustrates the spatial variations of flame transmisivity of the droplets for all the fuels and their blends starting at *2 mm* and incrementing at *2 mm* intervals to a maximum height of *20 mm*. The droplet volume was *2 mm³* and the room temperature was at *19°C*. Testing was done on the horizontal quartz filaments. It can be seen that biodiesel had twice as much transmisivity relative to ultra low sulfur diesel at *10 mm* above the filament. All the fuels exhibited a similar trend: as the laser beam height above the droplet gradually increased, flame transmisivity levels increased and reached a peak at *10 mm*. Then, transmisivity levels slowly declined as height was increased. Ultra low sulfur diesel had the lowest transmisivity (highest amount of soot) relative to the fuels tested. Harris [16] stated that more soot (less flame transmisivity) is the result of a higher nucleation rate of the flame. The results are valid for other fuels since the post flame gases are similar. As biodiesel concentration was increased in ultra low sulfur diesel, flame transmisivity increased. Ethanol had no soot (highest transmisivity), which was expected since alcohols do not exhibit sooting characteristics. As biodiesel was added to ethanol, transmisivity only showed a decrease at *50 %* biodiesel with *50 %* ethanol. Biodiesel blends lower than *50 %* with ethanol showed had higher flame transmisivity. Synthetic diesel had lower amounts of soot (more transmisivity) compared to ultra low sulfur diesel. Both increasing biodiesel with ethanol, and increasing biodiesel with ultra low sulfur diesel showed a convergence towards the unblended

biodiesel. Increasing biodiesel with ethanol resulted in higher soot (less transmisivity) and increasing biodiesel with ultra low sulfur diesel resulted in lower soot (higher transmisivity). A *50 %* mixture of ultra low sulfur diesel and ethanol was analyzed for interest sake.

Figure 6.32 delineates the effects of fuel pre-heating on the soot transmisivity of droplets. The droplet volume was *2 mm³* and the room temperature was at *19°C*. Testing was done on the horizontal quartz filaments. Biodiesel, ultra low sulfur diesel, and a B50 blend were tested at various temperatures, from room temperature, *19°C* to *100°C*. A full transmisivity sweep, from *2 mm* to *20 mm*, was conducted for temperatures at the lower bound (room temperature) and upper bound (*100°C*). Again, similar to Figure 6., the maximum level of transmisivity was at *10 mm*. Therefore, only single point measurements were taken at intermediate temperatures (*30°C, 40 °C, 50 °C, 60 °C*). Gradually pre-heating biodiesel resulted in the progressive decline of soot (increase in transmisivity). On the contrary, pre-heating the B50 blend and ultra low sulfur diesel resulted in higher soot content (decrease in transmisivity) which was in agreement with Nakanishi [34]'s findings. This is due to the mass of soot that exhausts from the flame which is determined by the balance of the soot formation and soot oxidation in the flame. As the air temperature increases, the flame temperature increases and thermal cracking of the fuel is promoted, so nucleation and growth of the soot particle increases. That is, the rate of soot formation increases. But at the same time, the rate of soot oxidation increases with the air temperature. The net soot release is derived from the difference of the net soot formation and the net soot oxidation in the flame. At extremely high temperature, the oxidation of soot formed in the flame becomes predominant.

In Figure 6.33, biodiesel was observed to have a sudden decrease in soot (increase in transmisivity) between *30°C* to *40°C* and at temperatures above *40°C*, transmisivity continued to slowly increase. At increasing temperatures, ultra low sulfur diesel and B50 had higher soot (lower transmisivity). The droplet volume was *2 mm³* and the room temperature was at *19°C*. Testing was done on the horizontal quartz filaments.

63

When testing the filaments in different orientations as it can be shown in Figure 6.34, less soot (more transmisivity) was registered with filaments arranged in a vertical position as opposed to a horizontal arrangement. This was due to the fact that after each trial, it was observed that soot solidified and conglomerated along the vertical shaft of the filament and at the bend. This phenomenon resulted in less soot being identified by the laser power measurement detector via laser light scattering. The droplet volume was *2 mm³* and the room temperature was at *19°C*.

Figure 6.31 clearly shows biodiesel has lower amounts of soot compared to ultra low sulfur diesel. Recall Figure 6.26 shows biodiesel has the highest flame temperature. This was an intriguing result. Normally, there is a direct correlation with flame temperature and soot levels, where higher flame temperatures will yield higher levels of soot. However, this was not the case. Glassman [14] stated that with higher flame temperature, there is less tendency to soot which was in agreement with the results obtained. This was due to the fact that there is competition between the rate of pyrolysis to form the precursors of soot and the rate of oxidative attack. Therefore, if the oxidation rate increases faster with temperature than the pyrolysis rate, there is a tendency for lower soot.

Trends found in this study were comparable to those found in Turns [51] and Glassman [15]. In particular, these trends are shown in Figure 6.31.
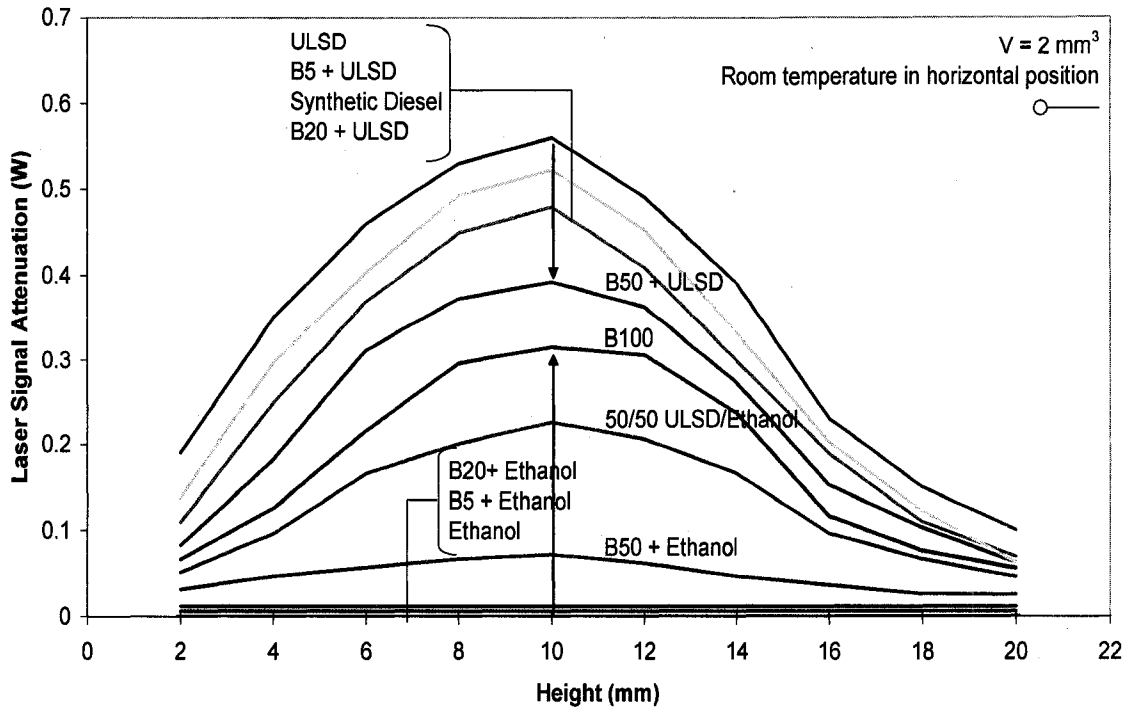
Figure 6.31 - Spatial variations of flame transmisivity
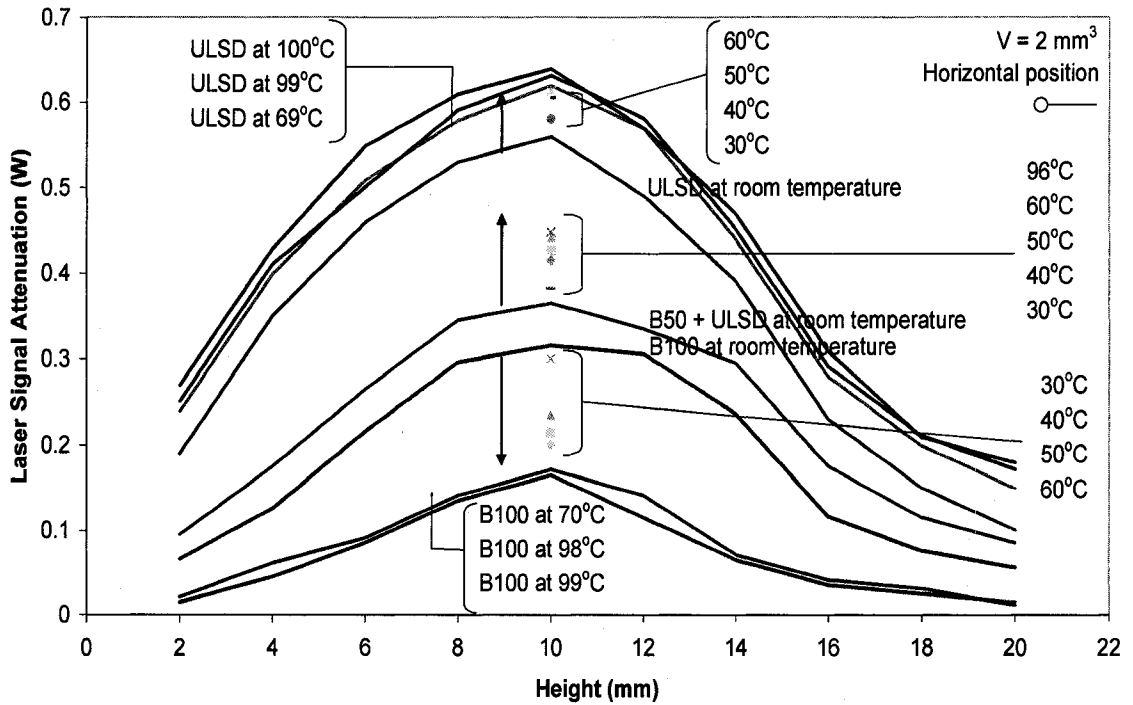
Figure 6.32 - Effects of heating on flame transmisivity

65
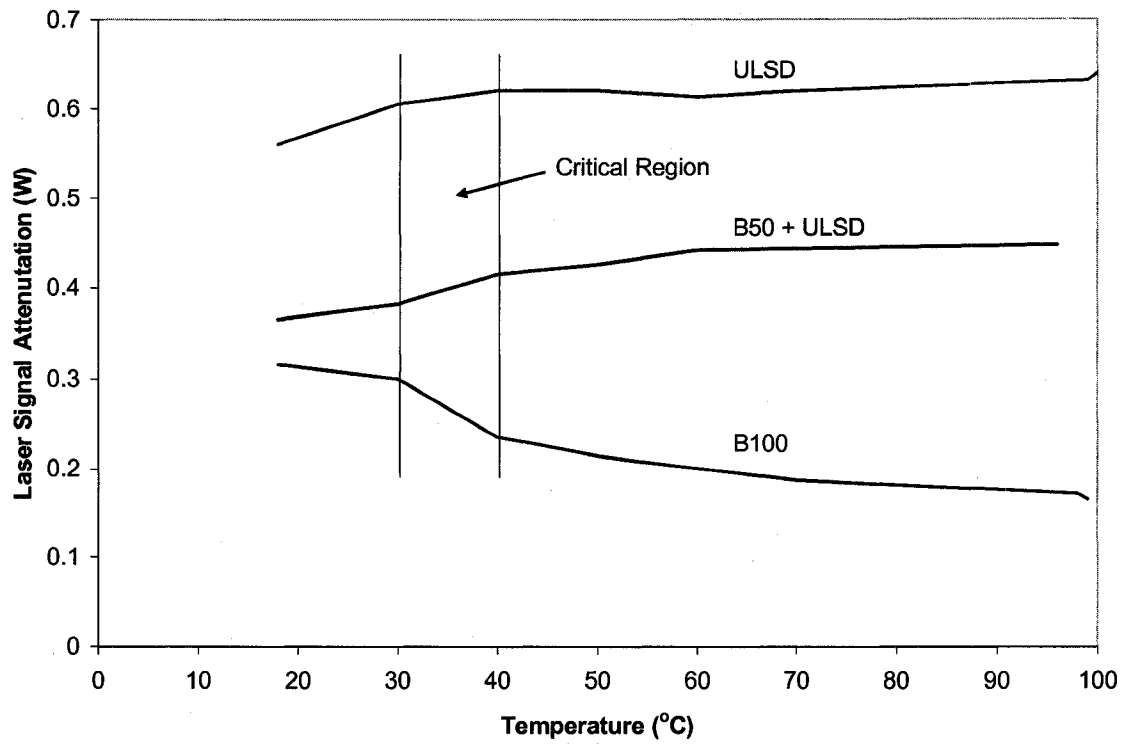
Figure 6.33 - Temperature impact of fuel pre-heat
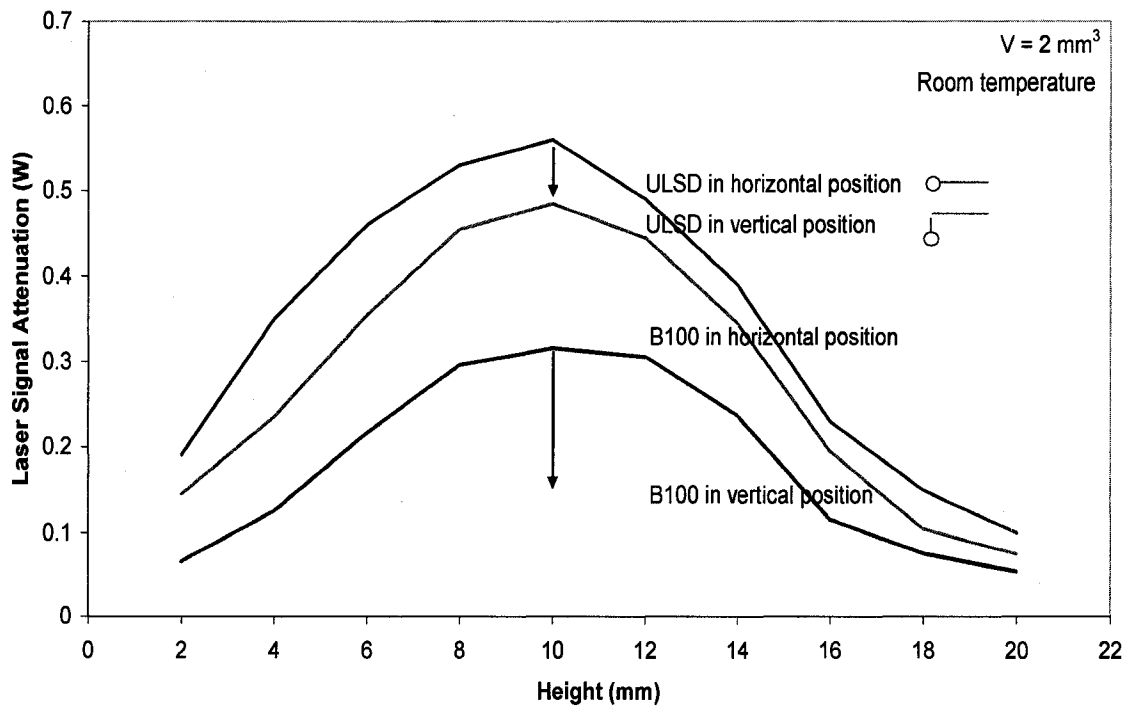
Figure 6.34 - Filament orientation and its effects on flame transmisivity

66

Chapter 7

Relevance to Engine Performance

7.1 Droplet Size Correlation

A 6.4 L V8 engine equipped with a dual-stage variable geometry turbocharger found in the 2008 Ford F-450 Super Duty pickup truck was used to correlate the maximum droplet diameter permissible under all possible engine speeds. In the dual-stage turbocharger, the smaller high pressure turbocharger had a turbine by-pass which opens as the inlet manifold boost pressure rises. At low mass flow rates, the by-pass is closed which allows the optimum use of the available expansion in the small turbine. As the gas flow rate increases with load and speed, progressively more expansion work is extracted from the larger turbine that drives the low pressure compressor. Stone [49] mentioned the benefits of two-stage turbocharging which leads to an improvement in low speed torque, an increase in maximum power output, a reduction in brake specific fuel consumption, and better transient response. A variable geometry turbocharger consists of variable angle vanes that are electronically adjusted by the engine control unit to optimize charge air. For example, under heavy acceleration or at wide open throttle, the vanes contract in order to restrict exhaust flow area and increase turbine speed thereby providing additional charge air. Variable geometry turbochargers are able to achieve more exhaust gas recirculation by controlling the pressure between the intake manifold and exhaust manifold. Exhaust gas recirculation lowers nitrogen oxide emissions. This is achieved by positioning the vanes to reduce the area for exhaust flow, effectively increasing exhaust manifold pressure while not necessarily increasing intake manifold pressure. The common-rail fuel injection system utilized advanced Piezo-actuated fuel injectors. These injectors allow multiple precision fuel injection bursts. Common-rail injection allows for independent control of the injection pressure over a wider operating speed range and load

67

range. The advantage of implementing a common-rail system is the ability to electronically control injection timing and injection rate which can assist in lowering engine noise and reducing nitrogen oxide emissions. Calculations to determine the maximum droplet diameter permissible under all operating speeds are as follows:

The time for one cycle is twice the time for one revolution.

$$t_{cycle} = 2 \times t_{revolution} \tag{7.1}$$

At *1000 RPM*, using Equation (6.1):

$$t_{cycle} = 2 \times t_{revolution} = 2\left(\frac{60\,s}{1000\frac{rev}{min}}\right) = 120\,ms$$

Stone [49] stated that in a spark ignition engine, the ignition delay (the time between start of ignition and start of combustion) is *30° CA* at *2500 RPM*. For a compression ignition engine, one can assume constant number of crank angles. Assuming the time to burn the fuel is *10° CA*, the time of combustion is the sum of the ignition delay and the time to burn the fuel. Therefore, the equivalent number of crank angles is *40°* which can be associated with *2500 RPM*. Interpolating *40° CA ≈ 2500 RPM* yields *100° CA ≈ 1000 RPM*. For ease of calculations, assume the time of combustion is *90° CA* at high load [63].

$$1\,cycle = 2\,revolutions$$
$$= 2 \times 360°\,CA$$
$$= 720°\,CA$$

$$\frac{90}{720} = \frac{1}{8}$$

Therefore, the time of combustion can be approximated as 1/8 the time of one cycle.

68

$$t_{combustion} = \frac{1}{8}t_{cycle} \qquad (7.2)$$

From Equation (6.2):

$$t_{combustion} = \frac{1}{8}t_{cycle} = \frac{120\,ms}{8} = 15\,ms$$

The droplet burning lifetime / rate constant for ultra low sulfur diesel was $1\ mm^2/s$. The maximum droplet diameter that will burn during the time of combustion can be calculated as follows:

$$\frac{dD^2}{dt} = k$$

$$\frac{dD^2}{dt} = 1\frac{mm^2}{s}$$

$$\frac{D^2}{t} = 1\frac{mm^2}{s}$$

$$D^2 = 1\frac{mm^2}{s}(15\,ms)$$

$$D^2 = 1\frac{mm^2}{s}(0.015s)$$

$$D^2 = 0.015\,mm^2$$

$$D = 0.1225\,mm \rightarrow 122.5\,\mu m$$

The above calculations were calculated starting at idle (*700 RPM*) and repeated at *100 RPM* increments up to the maximum allowable speed limit.

Figure 7.1 displays the experimentally obtained power and torque curves as well as droplet size as a function of engine speed. The maximum droplet diameter permissible is based on the ability to burn in this time. As engine speed increases, the maximum

69

permissible droplet diameter exhibits an exponential decaying function. Droplet diameter sizes start from *0.15 mm* at idle and gradually decay to *0.07 mm* at *3500 RPM*. Peak torque occurred at *2400 RPM* while maximum power was registered at *3000 RPM*. Torque stabilization occurred in the range of *2000 RPM* to *2800 RPM*.
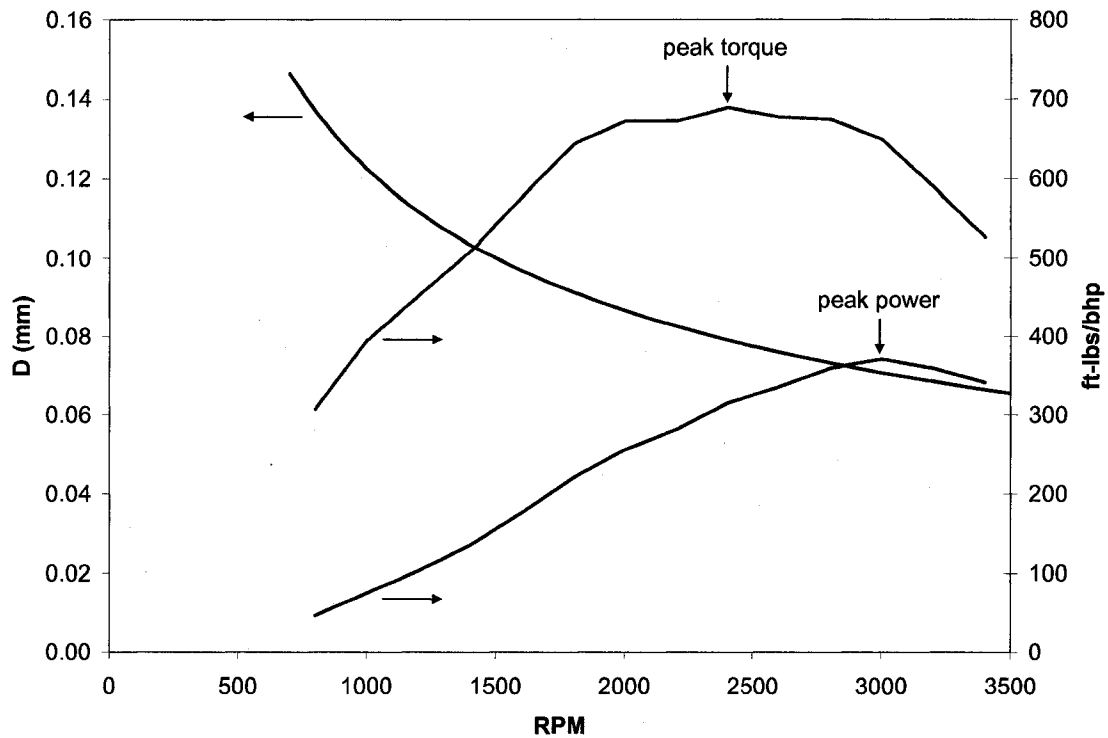
Figure 7.1 - Maximum droplet diameter permissible

7.2   Engine Analysis

There have been numerous interesting and informative studies documenting the effects of fueling an engine with biodiesel. These were quickly introduced in the Literature Review chapter. Some other good examples include those completed by Sharp [44], Knothe [23], Sluder [46], Kawano [22], Patterson [36], and Senatore [42]. One particular study that will be briefly discussed is from Fraer [12] where the authors conducted an investigation comparing the use biodiesel and petroleum diesel with a goal of obtaining quantitative information on the impact of biodiesel on engine component wear, in addition to maintenance and operating costs. The engines and fuel systems were removed from the

70

eight trucks and analyzed. Four 1996 Mack tractors and four 1993 Ford cargo vans were used. Two of each type were fueled with B20 and two with petroleum diesel. In other words, for the four Fords; two were fueled with biodiesel and two were fueled with petroleum diesel. This was the same case for the Mack engines. The engines were fueled with #2 diesel and B20 (20 % biodiesel, 80 % petroleum diesel) since it is the most common blend used in the United States. The engines and fuel systems were disassembled, analyzed, and evaluated for wear characteristics after four years of operation with over 600,000 miles accumulated on B20. Results indicated that there was very little difference in operational and maintenance costs attributed to the two different fuels. No abnormal wear was discovered. All engines exhibited normal wear for their mileage, independent of fuel. However, the Mack engines exhibited higher frequency of fuel filter and injector nozzle replacement. Biological contaminants may have caused the filter plugging. Sludge buildup was also noted around the rocker assemblies due to the accumulation of soaps in the engine oil from the biodiesel. The Ford engines did not have the filter plugging, injector replacement, or sludge accumulation issues noted with the Mack engines. This was due to the fact that the Ford engines used a smaller inline fuel injection pump system since the Fords had a smaller engine displacement (7.8 L) compared to the Macks (12.0 L). It was suggested that the greater fuel circulation volume was suspected to contribute to the fuel filter plugging evident with Mack engines. The fuel system, specifically the filter sizing and plumbing, may have also been a contributing factor.

71

Chapter 8

Statistical and Uncertainty Analysis

This chapter provides a brief overview of the possible errors that were encountered while performing the experiments mentioned in this thesis.

8.1   Statistical Analysis

A rudimentary statistical analysis was performed on the measurements taken.

Each measurement was conducted 10 times and based on those measurements, the sample mean was calculated. Assume n observations in a sample are represented by x_1, x_2, ..., x_n, then the sample mean is

$$\bar{x} = \frac{x_1 + x_2 + ... + x_n}{n} = \frac{\sum_{i=1}^{n} x_i}{n} \qquad (8.1.1)$$

The sample mean does not reveal all of the information about a sample data. The variability or scatter in the data may be characterized by the sample variance or the sample standard deviation.

Assume n observations in a sample are represented by x_1, x_2, ..., x_n, then the sample variance is

$$s^2 = \frac{\sum_{i=1}^{n}(x_i - \bar{x})^2}{n-1} \qquad (8.1.2)$$

72

Assume n observations in a sample are represented by x_1, x_2, ..., x_n, then the sample standard deviation is

$$s = \sqrt{\frac{\sum_{i-1}^{n}(x_i - \bar{x})^2}{n-1}}$$

(8.1.3)

The sample standard deviation has the desirable property of measuring variability of the variable of interest.

8.2 Uncertainty Analysis

Measurement can be defined as the process of assigning a value to a physical variable. Error in the measurement is the difference between the true value of the variable and the value registered by the measurement device. Uncertainty is the estimate of probable error in the measurement. Uncertainty analysis is the process of classifying and calculating errors. All uncertainty estimates will be made at the 95 % confidence level. This implies that 95 % of the time, the actual error will be less than the estimated uncertainty. The data plotted may include both bias and precision errors. Bias errors will tend to shift the entire data set away from the true line or may change its slope. Precision errors will cause the data to scatter about the true line.

8.2.1 Temperature

Fine-gauge exposed-junction thermocouples were selected because they offer better response times than grounded junction or ungrounded junction thermocouples as stated in the Omega Temperature Handbook [62].

For liquid temperature measurements, K-type Omega thermocouples were used. They had a 1.1 °C or 0.4 % limit of error.

For flame temperature measurements, S-type Omega thermocouples were used. They had a 0.6 °C or 0.1 % limit of error.

73

The following table illustrates the uncertainty in the peak temperatures for all the fuels tested.

Table 8.1 - Uncertainty in the peak temperatures (± °C)

B100	ULSD	E100	Synthetic Diesel	50/50 ULSD/Ethanol
2.08	2.53	1.49	1.34	2.39

B5	B20	B50
2.65	2.74	2.60

B5 + Ethanol	B20 + Ethanol	B50 + Ethanol
2.10	2.58	1.95

Assuming no random uncertainty exists, the following calculations were repeated for all fuels and their blends.

The random uncertainty of each measurement at the 95 % confidence level for all the fuels and their blends is as follows:

The sample mean $\bar{x}$ and sample standard s deviation were calculated each respective fuel.

Using the student's t-distribution at the confidence level of 95 % and 9 degrees of freedom, t = 2.262. Note: 10 trials of each measurement were taken, therefore the degrees of freedom, v = n - 1 is one less of the sample size.

The random uncertainty is calculated using:

$$P_i = t \times s \qquad (8.2.1.1)$$

The random uncertainty of the sample mean of the measurements at 95 % confidence level is as follows:

74

$$P_{\bar{x}} = \frac{t \times s}{n^{\frac{1}{2}}}$$

(8.2.1.2)

The random uncertainty of the mean of the measurements, assuming sample standard deviation was calculated on the basis of a large sample size (n > 30) is as follows assuming a large sample data set, but with the same sample standard deviation, t = 2:

$$P_{\bar{x}} = \frac{2 \times s}{n^{\frac{1}{2}}}$$

(8.2.1.3)

Assuming that the parent population is normally distributed, the 95 % confidence interval for the population mean can be found by calculating the two-sided confidence limits.

$$\pm \frac{t_{0.025,9} \times s}{n^{\frac{1}{2}}}$$

(8.2.1.4)

The results from the above calculations are summarized below:

Table 8.2 - Statistical summary of the peak temperatures (°C)

	B100	ULSD	E100	Synthetic Diesel	50/50 ULSD/Ethanol
Sample mean	584	481	293	449	432
Same standard deviation	2.80	3.40	2.01	1.81	3.22
Sample variance	7.83	11.57	4.06	3.29	10.4
Sample random uncertainty of measurements	6.24	7.58	4.48	4.03	7.17
Sample random uncertainty of mean	2.08	2.53	1.49	1.34	2.39
Sample random uncertainty based on a large sample	1.87	2.27	1.34	1.21	2.15
Two-sided confidence limits	2.08	2.53	1.49	1.34	2.39

75

Table 8.2 continued from previous page.

	B5	B20	B50
Sample mean	465	476	537
Same standard deviation	3.57	3.69	3.50
Sample variance	12.71	13.60	12.22
Sample random uncertainty of measurements	7.95	8.22	7.80
Sample random uncertainty of mean	2.65	2.74	2.60
Sample random uncertainty based on a large sample	2.38	2.46	2.33
Two-sided confidence limits	2.65	2.74	2.60

	B5 + Ethanol	B20 + Ethanol	B50 + Ethanol
Sample mean	291	443	502
Same standard deviation	2.83	3.48	2.63
Sample variance	8.01	12.10	6.93
Sample random uncertainty of measurements	6.31	7.75	5.86
Sample random uncertainty of mean	2.10	2.58	1.95
Sample random uncertainty based on a large sample	1.89	2.32	1.75
Two-sided confidence limits	2.10	2.58	1.95

76

The following table illustrates the uncertainty in the flame temperatures for all the fuels tested.

Table 8.3 - Uncertainty in the flame temperatures (± °C)

B100	ULSD	E100	Synthetic Diesel	50/50 ULSD/Ethanol
4.65	4.20	4.56	3.97	4.46

B5	B20	B50
3.83	3.66	3.54

B5 + Ethanol	B20 + Ethanol	B50 + Ethanol
4.01	4.02	3.83

Assuming no random uncertainty exists, the following calculations were repeated for all fuels and their blends.

The random uncertainty of each measurement at the 95 % confidence level for all the fuels and their blends is as follows:

The sample mean $\bar{x}$ and sample standard s deviation were calculated each respective fuel.

Using the student's t-distribution at the confidence level of 95 % and 9 degrees of freedom, t = 2.262. Note: 10 trials of each measurement were taken, therefore the degrees of freedom, $v = n - 1$ is one less of the sample size.

The random uncertainty is calculated using:

$$P_i = t \times s \qquad\qquad (8.2.1.5)$$

The random uncertainty of the sample mean of the measurements at 95 % confidence level is as follows:

$$P_{\bar{x}} = \frac{t \times s}{n^{\frac{1}{2}}} \qquad\qquad (8.2.1.6)$$

77

The random uncertainty of the mean of the measurements, assuming sample standard deviation was calculated on the basis of a large sample size (n > 30) is as follows assuming a large sample data set, but with the same sample standard deviation, t = 2:

$$P_{\bar{x}} = \frac{2 \times s}{n^{\frac{1}{2}}} \qquad (8.2.1.7)$$

Assuming that the parent population is normally distributed, the 95 % confidence interval for the population mean can be found by calculating the two-sided confidence limits.

$$\pm \frac{t_{0.025,9} \times s}{n^{\frac{1}{2}}} \qquad (8.2.1.8)$$

The results from the above calculations are summarized below:

Table 8.4 - Statistical summary of the flame temperatures (^{0}C)

	B100	ULSD	E100	Synthetic Diesel	50/50 ULSD/Ethanol
Sample mean	1434	1364	1312	1367	1334
Same standard deviation	7.18	5.57	6.05	5.26	5.91
Sample variance	38.10	31.07	36.62	27.66	34.93
Sample random uncertainty of measurements	13.96	12.61	13.69	11.90	13.37
Sample random uncertainty of mean	4.65	4.20	4.56	3.97	4.46
Sample random uncertainty based on a large sample	4.12	3.72	4.03	3.51	3.94
Two-sided confidence limits	4.65	4.20	4.56	3.97	4.46

78

Table 8.4 continued from previous page.

	B5	B20	B50
Sample mean	1361	1379	1387
Same standard deviation	5.08	4.85	4.70
Sample variance	25.79	23.56	22.10
Sample random uncertainty of measurements	11.49	10.98	10.63
Sample random uncertainty of mean	3.83	3.66	3.54
Sample random uncertainty based on a large sample	3.39	3.24	3.13
Two-sided confidence limits	3.83	3.66	3.54

	B5 + Ethanol	B20 + Ethanol	B50 + Ethanol
Sample mean	1310	1315	1323
Same standard deviation	5.31	5.33	5.08
Sample variance	28.23	28.44	25.79
Sample random uncertainty of measurements	12.02	12.06	11.49
Sample random uncertainty of mean	4.01	4.02	3.83
Sample random uncertainty based on a large sample	3.54	3.56	3.39
Two-sided confidence limits	4.01	4.02	3.83

8.2.2   Volume

For the delivery of the droplet, a 5 μL Hamilton high-precision micro-syringe fitted with a specialized Chaney adapter was used. The Hamilton Chaney adapter is a device that assures repetitive and identical syringe plunger location resulting in consistent droplet volume deliveries. It eliminates subjective errors when setting a syringe plunger at a specific volume. The syringe is accurate within ± 1 % of nominal volume and its precision is 1 % measured at 80 % of total scale volume.

8.2.3   Flame Transmisivity

A Coherent Innova 70 water-cooled argon ion laser generated a continuous laser beam with a light regulation of ± 0.5 % and a current regulation of ± 3.0 %. This was the maximum peak variation over any 30 minute operating duration following a two hour stabilization period. In order to quantify the flame transmisivity, an Ophir Orion laser power meter was used. It is capable of measuring voltage as precise as 0.001 W with an analog output accuracy of ± 0.2 %. The beam diameter was 1.5 mm and the beam divergence was 0.5 mRad. Optical noise was 0.5 % RMS measured with an RMS volt meter with a 10 Hz to 2 MHz bandwidth.

8.2.4   Droplet Burning Rate Constant

To quantify the uncertainty in the droplet burning rate constant k, recall the simplified mathematical expression for k:

$$k = \frac{D^2}{t} \tag{8.2.4.1}$$

The burning rate constant is defined as the square of the diameter of the droplet over the time it takes the droplet to completely vaporize.

80

The *k* value can be found by taking a least squares fit (linear regression) through the data, using the diameter-squared as the *y* variable. Line fits can average out precision errors.

The uncertainty for *k* is determined using the preceding equation.

$$\Delta k = \left[\left(\frac{\partial k}{\partial D}\Delta D\right)^2 + \left(\frac{\partial k}{\partial t}\Delta t\right)^2\right]^{\frac{1}{2}} \qquad (8.2.4.2)$$

where D represents the initial droplet diameter, t represents the droplet lifetime, ΔD represents the standard deviation of the droplet diameter, and Δt represents the time increment of the camera capturing rate (0.001 s).

The following table illustrates the uncertainty in the burning rate constants for all the fuels tested.

Table 8.5 - Uncertainty in the burning rate constants ($\pm$ mm^2/s)

	B100	ULSD	E100	Synthetic Diesel	50/50 ULSD/Ethanol
Δk	0.04	0.07	0.02	0.03	0.05

	B5	B20	B50
Δk	0.06	0.03	0.01

	B5 + Ethanol	B20 + Ethanol	B50 + Ethanol
Δk	0.03	0.04	0.06

Assuming no random uncertainty exists, the following calculations were repeated for all fuels and their blends.

The random uncertainty of each measurement at the 95 % confidence level for all the fuels and their blends is as follows:

The sample mean $\bar{x}$ and sample standard s deviation were calculated each respective fuel.

81

Using the student's t-distribution at the confidence level of 95 % and 9 degrees of freedom, t = 2.262. Note: 10 trials of each measurement were taken, therefore the degrees of freedom, $v = n - 1$ is one less of the sample size.

The random uncertainty is calculated using:

$$P_i = t \times s \qquad (8.2.4.3)$$

The random uncertainty of the sample mean of the measurements at 95 % confidence level is as follows:

$$P_{\bar{x}} = \frac{t \times s}{n^{\frac{1}{2}}} \qquad (8.2.4.4)$$

The random uncertainty of the mean of the measurements, assuming sample standard deviation was calculated on the basis of a large sample size (n > 30) is as follows assuming a large sample data set, but with the same sample standard deviation, t = 2:

$$P_{\bar{x}} = \frac{2 \times s}{n^{\frac{1}{2}}} \qquad (8.2.4.5)$$

Assuming that the parent population is normally distributed, the 95 % confidence interval for the population mean can be found by calculating the two-sided confidence limits.

$$\pm \frac{t_{0.025,9} \times s}{n^{\frac{1}{2}}} \qquad (8.2.4.6)$$

The results from the above calculations are summarized below:

82

Table 8.6 – Statistical summary of the burning rate constants (mm²/s)

	B100	ULSD	E100	Synthetic Diesel	50/50 ULSD/Ethanol
Sample mean	0.97	1.00	0.92	1.09	1.02
Same standard deviation	0.05	0.09	0.03	0.04	0.07
Sample variance	0.00	0.01	0.00	0.00	0.01
Sample random uncertainty of measurements	0.11	0.20	0.07	0.09	0.16
Sample random uncertainty of mean	0.04	0.07	0.02	0.03	0.05
Sample random uncertainty based on a large sample	0.03	0.06	0.02	0.03	0.04
Two-sided confidence limits	0.04	0.07	0.02	0.03	0.05

Table 8.6 continues on the next page.

Table 8.6 continued from previous page.

	B5	B20	B50
Sample mean	0.97	0.98	0.96
Same standard deviation	0.08	0.04	0.02
Sample variance	0.01	0.00	0.00
Sample random uncertainty of measurements	0.18	0.09	0.04
Sample random uncertainty of mean	0.06	0.03	0.01
Sample random uncertainty based on a large sample	0.05	0.03	0.01
Two-sided confidence limits	0.06	0.03	0.01

	B5 + Ethanol	B20 + Ethanol	B50 + Ethanol
Sample mean	1.16	1.07	1.00
Same standard deviation	0.04	0.06	0.08
Sample variance	0.00	0.00	0.01
Sample random uncertainty of measurements	0.09	0.13	0.18
Sample random uncertainty of mean	0.03	0.04	0.06
Sample random uncertainty based on a large sample	0.03	0.04	0.05
Two-sided confidence limits	0.03	0.04	0.06

84

Chapter 9

Summary, Conclusions and Recommendations

9.1   Summary

A study was undertaken to provide fundamental information regarding biodiesel as a transportation fuel. This was accomplished through droplet combustion analysis and examining flame transmisivity characteristics.

Four experimental setups were designed and assembled to allow for the evaluation of three fuels and their blends. Synthetic diesel was also tested, but not blended.

Biodiesel, ultra low sulfur diesel, ethanol, and a combination of their blends were selected to undergo the following experimental procedures:

- Temporal varying droplet dimension measurements (diameter and flame diameter)

- Temporal varying droplet liquid temperature measurements

- Spatial varying droplet flame temperature measurements along the flame axis

- Spatial varying soot transmisivity measurements along the flame axis

9.2   Conclusions

The most important finding was that biodiesel had lower amounts of soot (higher transmisivity). Ultra low sulfur diesel had the highest amount of soot (lowest

85

transmisivity). Synthetic diesel had lower amounts of soot (more transmisivity) compared to ultra low sulfur diesel. Both increasing biodiesel with ethanol, and increasing biodiesel with ultra low sulfur diesel showed a convergence towards the unblended biodiesel. Increasing biodiesel with ethanol resulted in higher soot (less transmisivity) and increasing biodiesel with ultra low sulfur diesel resulted in lower soot (higher transmisivity).

Gradually pre-heating biodiesel resulted in the progressive decline of soot (increase in transmisivity). On the contrary, pre-heating the B50 blend and ultra low sulfur diesel resulted in higher soot content (decrease in transmisivity).

When testing the filaments in different orientations, less soot (more transmisivity) was registered with filaments arranged in a vertical position as opposed to a horizontal arrangement.

As the laser beam height above the droplet gradually increased, flame transmisivity levels increased and reached a peak at *10 mm*. Then, transmisivity levels slowly declined as height was increased. Biodiesel had higher flame temperatures with lower amounts of soot (higher transmisivity).

The temporal variations of the square of the diameter indicated the presence of transient stages. The burning rate constants were calculated for the entire droplet lifetime and for the three transient stages. Adherence to the D^2 law during the three transient stages was observed. Single-component fuels such as ethanol had only one transient stage k_2. Not all of the fuels had a final transient stage.

It was determined that liquid heating had no effect on the burning rate constant.

The observed boiling temperatures for biodiesel, ultra low sulfur diesel, and ethanol tend to situate on the upper bounds of the referenced boiling temperature ranges.

86

It was observed that maximum flame temperatures increased and peaked at a certain spatial point, then gradually decreased with increasing height. The highest flame temperatures appeared between *4 mm* and *6 mm* from the centre of the droplet. Higher concentrations of biodiesel added to ultra low sulfur diesel and ethanol resulted in higher droplet and liquid temperatures.

9.3   *Future Work*

To further continue the work presented here, one can focus on the following:

- Analyzing droplet interaction such as those that would be present in fuel sprays. This would have a direct impact on high precision fuel delivery devices such as fuel injectors. Faeth [10] provides a good starting point for such a study.

- The droplet experiments mentioned could be conducted using the falling droplet technique or the porous sphere method. These were briefly described in the Literature Review chapter.

- The sooting characteristics of a fuel greatly depend on the flame structure and temperature of a system. Conducting soot experiments under high pressure would be advisable since changing the pressure experienced by a flame often results in changes to temperature, flow velocity, flame structure, and thermal diffusivity.

References

[1] Ackerman, M., and Williams, F.A., "Simplified model for droplet combustion in a slow convective flow", *Combustion and Flame*, 143:599-612 (2005).

[2] Agarwal, A.K., Bijwe J., and Das, L.M., "Wear Assessment in a Biodiesel Fueled Compression Ignition Engine", *Transactions of the ASME*, 125:820-826 (2003).

[3] Ahmed, M.A., Ejim, C.E., Fleck, B.A., and Amirfazli, A., "Effect of Biodiesel Fuel Properties and Its Blends on Atomization", *SAE Technical Paper*, 2006-01-0893.

[4] Anderson, V.L., and McLean R.A., *Design of Experiments: A Realistic Approach*, Marcel Dekker, New York, 1974.

[5] Austerlitz, H., *Data Acquisition Techniques Using Personal Computers*, Academic Press, San Diego, 1991.

[6] Beckwith, TG., Marangoni, R.D., and Lienhard, J.H., *Mechanical Measurements* (5th Ed.), Addison-Wesley, Massachusetts, 1993.

[7] Box, G.E.P., Hunter, W.G., and Hunter, J.S., *Statistics for Experimenters: An Introduction to Design, Data Analysis, and Model Building*, John Wiley and Sons, New York, 1978.

[8] Chomiak, J., *Combustion: A Study in Theory, Fact and Application*, Gordon and Breach, Switzerland, 1990.

[9] D'Alessio, J., Lazzaro, M., Massoli, P., and Moccia, V., "Thermo-Optical Investigation of Burning Biomass Pyrolysis Oil Droplets", *Twenty-Seventh (International) Symposium on Combustion*, The Combustion Institute, Boulder, 1998, p. 1915.

[10] Faeth, G.M., "Evaporation and Combustion of Sprays", *Progress in Energy and Combustion Science*, 9:1-75 (1983).

[11] Figliola, R.S., and Beasley, D.E., *Theory and Design for Mechanical Measurements* (2nd Ed.), John Wiley and Sons, New York, 1995.

[12] Fraer, R., Dinh, H., Proc, K., McCormick, R.L., Chandler, K., Buchholz, B., "Operating Experience and Teardown Analysis for Engines Operated on Biodiesel Blends (B20)", *SAE Technical Paper*, 2005-01-3641.

[13] Frenklach, M., Clary, D.W., Gardiner, W.C. Jr. and Stein, S.E., "Shock-Tube Pyrolysis of Acetylene: Sensitivity Analysis of The Reaction Mechanism For Soot Formation", *Twentieth (International) Symposium on Combustion*, The Combustion Institute, 1985, p. 889.

[14] Glassman, I., "Soot Formation in Combustion Processes", *Twenty-Second (International) Symposium on Combustion*, The Combustion Institute, Pittsburgh, 1988, p. 295.

[15] Glassman, I., *Combustion* (3rd Ed.), Academic Press, California, 1996.

[16] Harris, S.J., and Weiner, A.M., "Surface growth of soot particles in premixed ethylene flames", *Preprints of Papers - American Chemical Society*, 28:282 (1983).

[17] Heywood, J.B., *Internal Combustion Engine Fundamentals*, McGraw-Hill, New York, 1988.

[18] Hodgman, C.D., *Handbook of Chemistry and Physics* (43rd Ed.), The Chemical Rubber Publishing Co., Ohio, 1962.

[19] Hubbard, G.L., Denny, V.E., and Mills, A.F., "Droplet Evaporation: Effect of Transients and Variable Properties", *International Journal of Mass Transfer* 18: 1003-1008 (1974).

[20] Hui-ya, Z., Yu-sheng, Z, Bo, X., and Chun-lan, M, "Extension of O'Rourke Droplet Collision Model: Application to Diesel Spray of Single-hole Injector", *SAE Technical Paper*, 2006-01-3335.

[21] Kadota, T., and Hiroyasu, H., "Soot Concentration Measurement in a Fuel Droplet Flame via Laser Light Scattering", *Combustion and Flame* 55:195-201 (1984).

[22] Kawano, D., Ishii, H., Goto, Y., and Noda, A., "Application of Biodiesel Fuel to Modern Diesel Engine", *SAE Technical Paper*, 2006-01-0233.

[23] Knothe, G., "The Lubricity of Biodiesel", *SAE Technical Paper*, 2005-01-3672.

[24] Knothe, G., and Steidley, K.R., "Lubricity of Components of Biodiesel and Petrodiesel. The Origin of Biodiesel Lubricity", *Energy & Fuels* 19:1192-1200 (2005).

[25] Kuo, K.K., *Principles of Combustion* (2nd Ed.), John Wiley and Sons, New Jersey, 2005.

[26] Law, C.K., "Recent advances in droplet vaporization and combustion", *Progress in Energy and Combustion Science* 8:171-201 (1982).

[27] Law, C.K., *Combustion Physics*, Cambridge University Press, New York, 2006.

[28] Ma, F., and Hanna, M.A., "Biodiesel production: a review", *Bioresource Technology* 70:1-15 (1999).

[29] Magnussen, B.F., and Hjertager, B.H., in *Sixteenth (International) Symposium on Combustion*, The Combustion Institute, Italy, 1979, p. 719.

[30] Makino, A., and Fukada, H., "Combustion Behavior of a Falling Sodium Droplet: Burning Rate-Constant and Drag Coefficient", *Heat Transfer* 34:481-495 (2005).

[31] Maly, R.R., and Degen, W., "Impact of Future Fuels", *SAE Technical Paper*, 2002-21-0073.

[32] Mitsuya, M., Hanai, H., Sakurai, S., Ogami, Y., and Kobayashi, H., "Droplet combustion experiments in varying forced convection using microgravity environment", *International Journal of Heat and Fluid Flow* 26:914-921 (2005).

[33] Moon, S., Choi, J., Abo-Serie, E., and Bae, C., "The Effects of Injector Temperature on Spray and Combustion Characteristics in a Single Cylinder DISI Engine", *SAE Technical Paper*, 2005-01-0101.

[34] Nakanishi, K., Kadota, T., Hiroyasu, H., "Effect of air velocity and temperature on the soot formation by combustion of a fuel droplet", *Combustion and Flame* 40:247-262 (1981).

[35] Nuruzzaman, A.S.M., Hedley, A.B., and Beer, J.M., "Combustion rates in self-supporting flames on monosized droplet streams", *Journal of the Institute of Fuel* 301-310 (1970).

[36] Patterson, J., Hassan, M.G., Clarke, A., Shama, G., Hellgardt, K., and Chen, R., "Experimental Study of DI Diesel Engine Performance Using Three Different Biodiesel Fuels", *SAE Technical Paper*, 2006-01-0234.

[37] Pereira, M.G., and Mudge, S.M., "Cleaning oiled shores: laboratory experiments testing the potential use of vegetable oil biodiesels", *Chemosphere* 54:297-304 (2004).

[38] Peskin, R.L., and Wise, H., "A Theory for Ignition and Deflagration of Fuel Drops", *AIAA Journal*, 4:1646-1650 (1966).

[39] Quigley, R., and Barbour, R.H., "Biodiesel Quality Improvement with Additive Treatment", *SAE Technical Paper*, 2004-01-1869.

[40] Scholl, K.W., and Sorenson, S.C., "Combustion of Soybean Oil Methyl Ester in a Direct Injection Diesel Engine", *SAE Technical Paper*, 930934.

[41] Schlichting, H., *Boundary-Layer Theory* (6th Ed.), McGraw-Hill, New York, 1968.

[42] Senatore, A., Cardonne, M., and Buono, D., "Performances and Emissions Optimization of a CR Diesel Engine Fuelled with Biodiesel", *SAE Technical Paper*, 2006-01-0235.

[43] Shaddix, C.R., and Tennison, P.J., in *Twenty-Seventh (International) Symposium on Combustion*, The Combustion Institute, Boulder, 1998, p. 1907.

[44] Sharp, C.A., and Ryan, T.W., "Heavy-Duty Diesel Engine Emissions Tests Using Special Biodiesel Fuels", *SAE Technical Paper*, 2005-01-3671.

[45] Sivathanu, Y.R., and Faeth, G.M., "Temperature / Soot Volume Fraction Correlations in the Fuel-Rich Region of Buoyant Turbulent Diffusion Flames, *Combustion and Flame*, 81:150-165 (1990).

[46] Sluder, C.S, Wagner, R.M., Lewis, S.A., and Storey J.M.E., "Fuel Property Effects on Emissions from High Efficiency Clean Combustion in a Diesel Engine", *SAE Technical Paper*, 2006-01-0080.

[47] Sobiesiak, A., The mechanism of the flame propagation in the model fuel droplet system under zero-gravity conditions, Ph.D. Thesis, Warsaw University of Technology, 1981.

[48] Spalding, D.B., *Combustion and Mass Transfer*, Pergamon, New York, 1979.

[49] Stone, R., *Introduction to Internal Combustion Engines*, SAE, Pennsylvania, 1999.

[50] Strehlow, R.A., *Combustion Fundamentals*, McGraw-Hill, New York, 1984.

[51] Turns, S.R., *An Introduction to Combustion: Concepts and Applications* (2nd Ed.), McGraw-Hill, New York, 2000.

[52] Tyson, K.S, *Biodiesel Handling and Use Guidelines*, National Renewable Laboratory, Colorado, 2001.

[53] Vander Wal, R.L., and Dietrich, D.L., "Laser-induced incandescence applied to droplet combustion", *Applied Optics* 34:1103-1007 (1995).

91

[54] Vaughn, T., Hammill, M., Harris, and M., Marchese, A.J., "Ignition Delay of Bio-Ester Fuel Droplets", *SAE Technical Paper*, 2006-21-3302.

[55] Wainner, R.T., and Seitzman, J.M., "Soot Diagnostics using Laser-Induced Incandescence in Flames and Exhaust Flows", *AIAA*, 99-0640 (1999).

[56] Wardle, D.A., "Global sale of green air travel supported using biodiesel", *Renewable & Sustainable Energy Reviews* 7:1-64 (2003).

[57] Warnatz, J., Maas, U., and Dibble, R.W., *Combustion: Physical and Chemical Fundamentals, Modeling and Simulation, Experiments, Pollutant Formation* (3rd Ed.), Springer, Germany, 2001.

[58] Wheeler, A.J., and Ganji, A.R., *Introduction to Engineering Experimentation* (2nd Ed.), Prentice Hall, New Jersey, 2003.

[59] Williams, F.A., and Ackerman, M., "Simplified model for droplet combustion in a slow convective flow", *Combustion and Flame* 143:599-612 (2005).

[60] Wilson, J.R., "Clean Diesel Fuel and Diesel Fuel Substitutes", TMG, 2004

[61] Xu, G., Masiki, I., Honma, S., Sasaki, M., Ikeda, K., Nagaishi, H., and Takeshita, Y., "Combustion characteristics of droplets composed of light cycle oil and diesel light oil in a hot-air chamber", *Fuel* 82:319-330 (2003).

[62] Omega Engineering, Inc., *The Temperature Handbook – Canadian Edition, Volume 2*, Laval, Quebec (2006).

[63] Sobiesiak, A., *Internal Combustion Engines* lecture notes, University of Windsor, 2006.

Appendices

A   *Diameter and Flame Diameter Measurements*
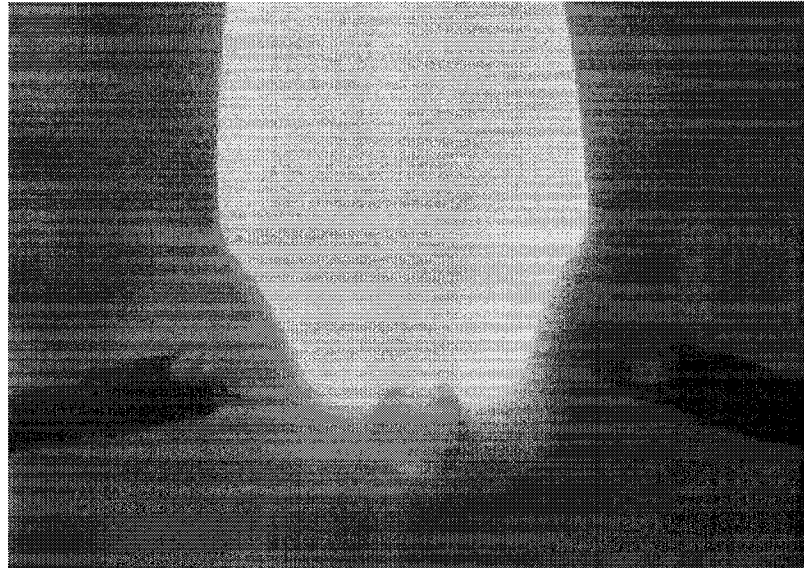

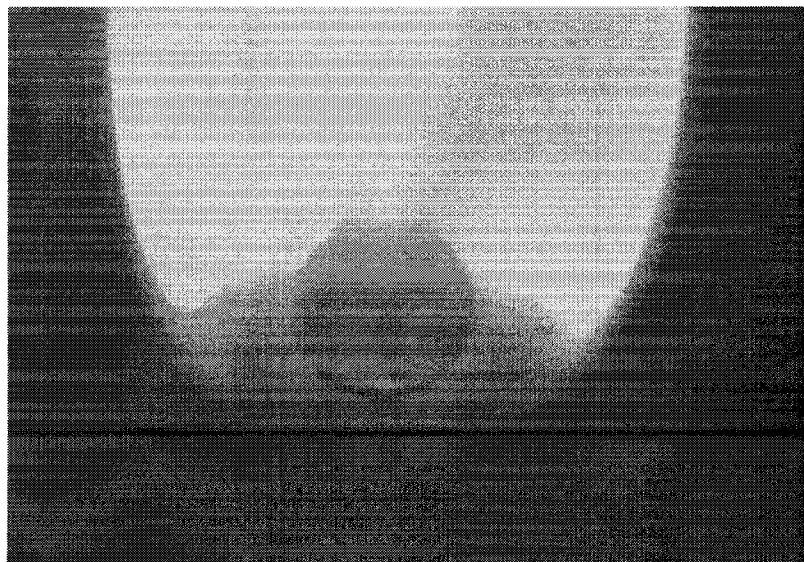**Figure A.1 - Previous ignition system using free hanging electrodes**

Figure A.2 - Current ignition system using fully adjustable tungsten electrodes

93

Table A.1 - Burning rate constants using free hanging electrodes

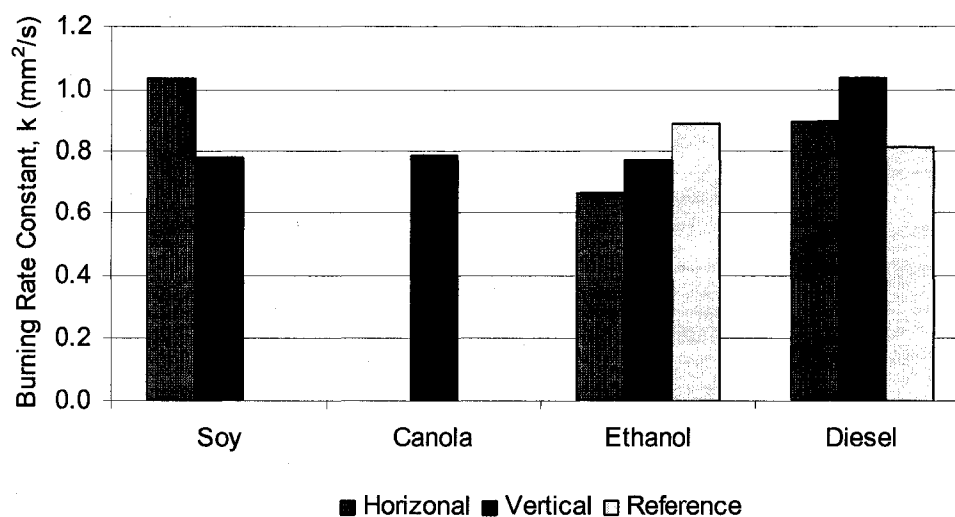| Fuel	Burning Rate Constant, k (mm^2/s)		
	Horizontal	Vertical	Reference
Soy-based Biodiesel	1.04	0.78	-
Canola-based Biodiesel	-	0.79	-
Ethanol	0.67	0.77	0.89 [8]
Diesel	0.90	1.03	0.82 (cetane) [8]

Figure A.3 - Comparative plot of burning constants using free hanging electrodes

B   Liquid and Flame Temperature Measurements

Table B.1 - Thermocouple maximum service temperature

Thermocouple Type	0.13 mm (0.005")	0.38 mm (0.015")	0.51 mm (0.020")	0.81 mm 0.032
J**	315°C (600°F)	371°C (700°F)	371°C (700°F)	482°C (900°F)
K	593°C (1100°F)	871°C (1600°F)	871°C (1600°F)	982°C (1800°F)
N	593°C (1100°F)	871°C (1600°F)	871°C (1600°F)	982°C (1800°F)
T	149°C (300°F)	204°C (400°F)	204°C (400°F)	260°C (500°F)
E	315°C (600°F)	426°C (800°F)	426°C (800°F)	593°C (1100°F)
R,S	-	-	1450°C (2642°F)	1450°C (2642°F)
B	-	-	1700°C (3092°F)	1700°C (3092°F)

94

Table B.2 - Thermocouple response time

Wire Size mm (Inches)	Still Air 427°C/38°C 800°F/100°F	60 ft./sec Air 427°C/38°C 800°F/100°F	Still H2O 93°C/38°C 200°F/100°F
0.025 (0.001)	0.05 sec	0.004 sec	0.002 sec
0.125 (0.005)	1.0 sec	0.08 sec	0.04 sec
0.381 (0.015)	10.0 sec	0.80 sec	0.40 sec
0.75 (0.032)	40.0 sec	3.2 sec	1.6 sec

Table B.3 - Base metal calibrations: 300 mm (12") length standard

Calibration	Wire Dia. mm (in)	Model Number
K CHROMEGA® ALOMEGA®	† 0.013 (0.0005)	CHAL-0005
	0.025 (0.001)	CHAL-001
	0.050 (0.002)	CHAL-002
	0.075 (0.003)	CHAL-003
	0.125 (0.005)	CHAL-005
	0.25 (0.010)	CHAL-010
	0.38 (0.015)	CHAL-015
	0.50 (0.020)	CHAL-020
	0.81 (0.032)	CHAL-032

Table B.4 - Pt/Rh calibrations: 150 mm (6") length standard

Calibration	Wire Dia. mm (in)	Model Number
S Pt/10%Rh- Pt	0.025 (0.001)	P10R-001
	0.050 (0.002)	P10R-002
	0.075 (0.003)	P10R-003
	0.125 (0.005)	P10R-005
	0.20 (0.008)	P10R-008
	0.25 (0.010)	P10R-010
	0.38 (0.015)	P10R-015
	0.50 (0.020)	P10R-020
	0.81 (0.032)	P10R-032

95

C   Flame Transmisivity Measurements

From the following thermopile response curve, the time constant of the laser power meter was determined to be approximately 0.7 s.

THERMOPILE HEAD RESPONSE CURVE:
23-JUN-2004 Head Type: 10A-V1 Ver 1 S/N: 160187
Overshoot= 0.6% at 1.6 seconds;   Undershoot= 0.5% at 3.9 seconds
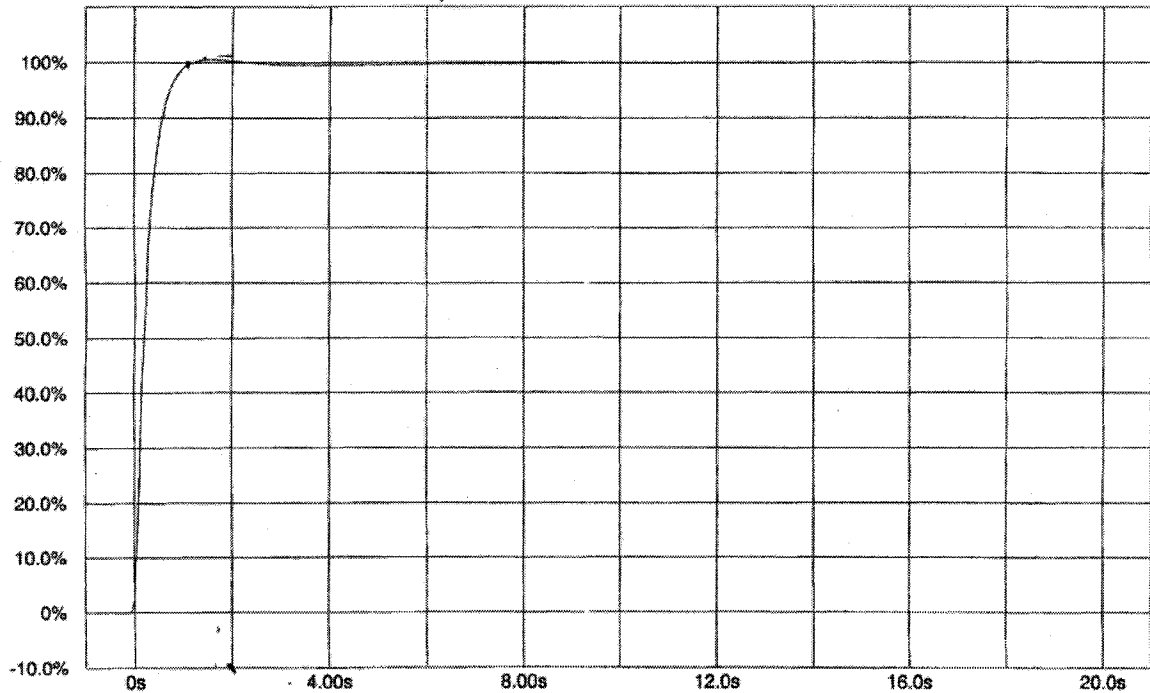Time to settle to 95% was 0.7 seconds;   Factor= 1.075

Figure C.1 - Thermopile head response curve

96

Vita Auctoris

S.C. Anthony Lam graduated from Queen's University in 2004 with a Bachelor of Science degree in Mechanical Engineering. He is currently a candidate for a Master of Applied Science degree in Mechanical Engineering at the University of Windsor.